Distribution Agreement

In presenting this thesis or dissertation as a partial fulfillment of the requirements for an advanced degree from Emory University, I hereby grant to Emory University and its agents the non-exclusive license to archive, make accessible and display my thesis or dissertation in whole or in part in all forms of media, now or hereafter known, including display on the world wide web. I understand that I may select some access restrictions as part of the online submission of this thesis or dissertation. I retain all ownership rights to the copyright of the thesis or dissertation. I also retain the right to use in future works (such as articles or books) all or part of this thesis or dissertation.

Signature: _____ _____

Terrence Michael Wright, Jr. Date

CONTRIBUTION OF MOTOR NEURON INTRINSIC PROPERTIES TO MOTOR PATTERN GENERATION

By
Terrence Michael Wright, Jr.

Doctor of Philosophy

Graduate Division of Biological and Biomedical Sciences
Graduate Program in Neuroscience
James T. Laney Graduate School

_____

Ronald L. Calabrese
Advisor

_____

Robert J. Butera
Committee Member

_____

Shawn Hochman
Committee Member

_____

Astrid A. Prinz
Committee Member

_____

Peter Wenner
Committee Member

_____

Lisa A. Tedesco, Ph.D.
Dean of the James T. Laney School of Graduate Studies

_____

Date

CONTRIBUTION OF MOTOR NEURON INTRINSIC PROPERTIES TO MOTOR PATTERN GENERATION

By

Terrence Michael Wright, Jr.

B.S., California State University, San Marcos, 2002

M.S., California State University, San Marcos, 2004

Advisor: Ronald L. Calabrese

An abstract of

A dissertation submitted to the Faculty of the

James T. Laney School of Graduate Studies of Emory University

in partial fulfillment of the requirements for the degree of

Doctor of Philosophy

Graduate Division of Biological and Biomedical Sciences

Graduate Program in Neuroscience

2011

ABSTRACT

CONTRIBUTION OF MOTOR NEURON INTRINSIC PROPERTIES TO MOTOR PATTERN GENERATION

By Terrence Michael Wright, Jr.

Rhythmic motor patterns, such as walking, are generated, in part, by rhythmically active neural networks called central pattern generators (CPG's; Marder and Calabrese, 1996). Typically, CPG's provide rhythmically patterned synaptic drive onto motor neurons in order to coordinate them, with appropriate phase differences, into a motor pattern appropriate for the behavior. These premotor patterns of drive contain both timing information and patterns of synaptic strengths. Invertebrate preparations, with their simple and accessible nervous systems, have been used to generate principles that underlie how premotor patterns of synaptic input interact with motor neurons to produce stereotyped motor outputs (Marder and Bucher, 2007). Here, I use the leech heartbeat CPG, a system in which patterns of synaptic drive onto motor neurons can be easily measured, to address how a CPG circuit coordinates its motor neurons to produce stereotyped motor patterns.

In the first of two studies, I show that, although the segmental input pattern is the primary determinant of motor neuron output, the intrinsic properties of the heart motor neurons play an important role in determining how they are coordinated by their segmental synaptic input pattern, particularly when receiving one of the two input patterns these motor neurons receive.

In the second study, I show, in both modeling and in follow-up experiments in the living system, that the generation of one motor pattern is a consequence of the nearly synchronous premotor timing information produced by the leech heartbeat CPG. For the other motor pattern, I show that premotor timing information determines the range over which motor neurons can fire while synaptic strength profiles define the actual motor progression.

These experiments provide a direct assessment of how motor neuron intrinsic properties interact with their premotor pattern of synaptic drive to produce rhythmic motor output. Furthermore, the data presented here may inform studies on motor pattern generation in other systems, including studies on recovery of locomotor control in patients with spinal cord injury.

CONTRIBUTION OF MOTOR NEURON INTRINSIC PROPERTIES TO MOTOR PATTERN GENERATION

By

Terrence Michael Wright, Jr.

B.S. California State University, San Marcos

M.S. California State University, San Marcos

Advisor: Ronald L. Calabrese

A dissertation submitted to the Faculty of the
James T. Laney School of Graduate Studies of Emory University
in partial fulfillment of the requirements for the degree of
Doctor of Philosophy

Graduate Division of Biological and Biomedical Sciences
Graduate Program in Neuroscience
2011

ACKNOWLEDGEMENTS

None of what follows would have been possible without the love, care and kindness that has been shown to me since I matriculated to Emory. I consider myself the rare graduate student who was able to pursue the kind of training I envisioned when I started this adventure. Along the way, I have been beyond blessed to have formed relationships and bonds with my peers that extend beyond the realms of the scientific endeavor here at Emory, at Georgia Tech and through my years as a student and TA at the Neural Systems and Behavior Course at Woods Hole, Mass. I value all of these people for challenging me in the way I think not only about science, but also about life, and I can truly say I am better for it. While I could in no way acknowledge all of these people, I have endeavored to acknowledge those who have been most instrumental in my graduate training. The order of acknowledgement in no way signifies the importance of their contribution.

I wish to acknowledge my PhD mentor and friend, Ronald L. Calabrese. I believe the noun “mentor” to be more a more appropriate description than “adviser” does when describing who Ron has been to me. An advisor, as described by Webster’s as “a person who gives advice”, certainly describes Ron, but I do not believe this captures the essence of who Ron is. Mentor, on the other hand, is defined as “a trusted counselor or guide”. That, I believe, captures the essence of who Ron is, for while Ron is certainly able to give advice, when it comes to his approach in training graduate students, Ron has been a guide to me throughout

my time in the lab. I thank you, Ron, for guiding me in the development of my scientific abilities.

I also thank each member of my committee (Astrid Prinz, Pete Wenner, Robert Butera and Shawn Hochman) for challenging me in my scientific abilities and thinking. It is because of you all that this thesis has achieved what it has. My committee has truly been what a committee should be: they continually, and, perhaps, with some pleasure on their part, challenged me in every aspect of this project.

I also thank the members of the Calabrese Lab, both past and present (Rebecca Roffman, Angela Wenning, Paul Garcia, Adam Weaver, Anca Doloc-Mihu, Ian Cunningham, Andrei Ivanov, Andrey Olypher, Damon Lamb and Anne-Elise Tobin). I am honored to have formed friendships with each of you on both a scientific and personal level, and I thank all of you for challenging me through scientific discussion to think about the science I was doing.

I also thank Sonia Hayden for her friendship and help to all the students in the Neuroscience Program. While I wish her all the best in her new position in Psychology, I know her heart will always be with us in the Neuroscience Program.

I also thank the entire Biology Department for their very generous support of me. In particular, I thank the support staff (Tonya, Barbara, Regina, Betsy, Jan, Gail, Malia, Lynn and Martha) for helping me with anything I needed. I was their Charlie, and they were my Angels.

Finally, I thank my family, whose love and admiration I truly cherish. To my smallest fan, Jada: Poppa loves the way you love science and how you think scientifically. I know you will be a great scientist one day. To Dallas: you are already smarter than I was at your age; continue to work hard and all the hopes, goals and dreams you set for yourself will be within your grasp.

To my beloved Carmen: words cannot express the joy you bring to my life. God has truly blessed us, and I will be forever grateful for the support and encouragement you have given me. I have not always gotten things right, but you have never ceased to love me. I thank you for your heart for the girls and me; I thank you for your heart for our home, and I thank you for always pulling for me. It is to you, Jada and Dallas that this Thesis is dedicated.

TABLE OF CONTENTS PAGE

LIST OF FIGURES PAGE

LIST OF FIGURES PAGE

LIST OF TABLES

CHAPTER 1

GENERAL INTRODUCTION

Rhythmic motor behaviors, such as walking (Kiehn 2006), swimming (Grillner 2003) and breathing (Feldman et al. 1991; Suzue 1984), are generated by neural networks called central pattern generators (CPG's). A defining characteristic of these networks is their ability to produce a fictive pattern in *in vitro* preparations lacking sensory input that is similar to the motor pattern observed *in vivo* (Marder and Bucher 2007; Marder and Calabrese 1996). Analyses of CPG's in many preparations have been instrumental in understanding how rhythmic motor activity is generated and/or modulated. Studies of CPG's in animals may ultimately result in novel therapeutic strategies for addressing spinal cord injury (SCI), where the primary effect is a loss of locomotor behavior.

1.1 Central Pattern Generators

CPG's have been shown to underlie many rhythmic patterns, including swimming in both lamprey (Grillner 2003) and tadpole (Li et al. 2001) and locomotion in rodents (Kiehn 2006). The CPG that is best characterized is the stomatogastric nervous system (STN) of decapod crustaceans (Marder and

Bucher 2007). This small network of ~30 neurons contains two central pattern-generating circuits, the pyloric and gastric mill CPGs. The pyloric CPG controls the muscles that move the pylorus, while the gastric mill CPG controls the muscles that move the teeth in the gastric mill. During the past 40 years, work in the stomatogastric system has provided tremendous insight into how rhythmic motor patterns can be generated. Unlike the stomatogastric system, however, the CPG's governing swimming and walking are distributed over multiple spinal segments. Therefore, motor patterns in these systems are the result of synaptic interactions both within and across adjacent segments, producing a traveling wave of activity that results in an appropriate wave of muscle activity along the body axis for swimming or coordinated muscle activity that spans limbs in rodents. Mathematical and experimental studies in the lamprey have suggested that segmentally distributed CPG's can be represented as a chain of oscillators with nearest-neighbor coupling (Skinner et al. 1997; Wadden et al. 1993).

Part of understanding how a CPG produces an appropriate motor pattern requires knowledge of how the CPG premotor interneurons are connected to the motor neurons they control. Only in simpler vertebrate preparations have CPG interneurons been identified so that such an analysis is possible (Grillner 2003; Soffe et al. 2009). Invertebrates, with their simple and accessible nervous systems, have been instrumental in providing mechanisms and principles that govern how rhythmic motor patterns are generated (Nusbaum and Beenhakker 2002) and selected (DeLong et al. 2009).

The leech heartbeat CPG allows for a complete analysis of how CPG's generate appropriate motor patterns at the cellular level because of our mechanistic understanding of how the CPG itself is organized (Norris et al. 2006) and because of our ability to perform simultaneous recordings from both the premotor interneurons of the CPG and the motor neurons responsible for its output (Norris et al. 2007a; b). We have been able to generate conductance-based models of the interaction of the heartbeat CPG with the motor neurons that have driven experiments in the leech nervous system. An important goal of this thesis is to understand how output from the heartbeat CPG is translated into an appropriate heartbeat motor pattern.

1.2 Motor Neuron Intrinsic Properties

Because motor neurons innervate the muscles that underlie rhythmic motor behaviors, they represent the final output pathway of a rhythmically active network. Therefore, in order to generate an appropriate motor pattern, CPG's must coordinate motor neurons into rhythmic firing with appropriate phase relationships. Much work in the field has focused on how synaptic connections within CPG circuits produce the rhythmic activation of the motor neurons that underlie these systems. Although the lateral pyloric (LP) motor neuron which receives input from pacemaker neurons of the pyloric CPG in the stomatogastric network has served as a model for how motor neuron intrinsic properties

influence the integration of their synaptic input (Marder and Bucher 2007), less is known about what role motor neuron intrinsic properties in other animals play in integrating their premotor patterns of synaptic drive. Owing to this lack, the functional contribution of motor neuron intrinsic properties to rhythmic motor output is poorly understood.

A few studies have shown that motor neurons contain intrinsic properties that may shape the input they receive from the CPG. Motor neurons in cats, for example, can express plateau potentials in response to a synaptic input that lasts beyond the time that the input is active (Lee and Heckman, 1998, Edom and Kiehn, 1998). This bistability could confer upon that motor neuron the ability to sustain activity in the absence of ongoing synaptic input, and thus contribute to motor output in the cat. Motor neurons in the rodent express an active conductance, termed I_h, that acts to depolarize a motor neuron during the phase in the cycle of their activity where they receive inhibitory input (Kiehn et al. 2000) from the spinal locomotor CPG. This current may serve to promote a phase advance of the motor neurons activity during locomotor activity. Taken together, these two examples indicate that intrinsic properties in these motor neurons could affect the motor output in these preparations.

The functional consequence of these intrinsic properties has not been determined, however, owing to lack of knowledge about the premotor CPG networks that drive these motor patterns. This problem is illustrated by a recent study in the turtle fictive scratch preparation (Alaburda et al. 2005). In this

paper, Alaburda et. al showed, in spinal slices, turtle motor neurons could express plateau potentials that were abolished in the presence of muscimol, a $GABA_A$ agonist that mimicked inhibitory synaptic input from the scratch CPG. Furthermore, in intact preparations, they showed that motor neurons exhibited large voltage responses to injected current in the absence of input from the scratch CPG. Once the CPG was activated, however, the same current input elicited a reduced response from the same motor neuron. Taken together, these results indicate that, although turtle motor neurons contain intrinsic properties that may affect how they integrate their premotor synaptic drive and thus allow them to contribute to the motor output observed *in vitro*, the synaptic conductance arising from the premotor CPG network onto these motor neurons obscures the expression of these properties. Therefore, these results suggest that a quantification of the premotor pattern of synaptic drive onto these motor neurons will be required in order to determine the functional contribution these motor neurons are making to the output observed in the living system. An important goal of this thesis will be to understand, in the context of a physiologically realistic synaptic input pattern, the functional contribution of motor neuron intrinsic properties to their output activity.

1.3 Animal-to-Animal Variability and Stereotyped Motor Output

Recent theoretical studies of parameter variation in conductance-based models have shown that a large number of parameter sets (i.e., combinations of intrinsic membrane and synaptic conductances) can produce similar CPG output (Prinz et al. 2004). Indeed, in the pyloric network of the stomatogastric CPG, many studies have shown that there can be up to five-fold variability in intrinsic and synaptic conductances across animals, yet functional pyloric rhythms are always produced (Goaillard et al. 2009).

One potential explanation for the range of parameter sets that support functional activity is that changes in one parameter can be compensated by changes in another parameter. Indeed, in follow up experimental work on the pyloric CPG of the STN Schulz et al (2007) showed that, in pyloric dilator (PD) motor neurons of the STN, there are positive correlations between the mRNA encoding the I_h channel and the mRNA encoding the I_A channel. The I_h channel would promote increased excitability of the PD cell, whereas I_A would decrease the excitability of the PD cell. Therefore, when combined, increases in one will compensate increases in the other, resulting in similar output for that motor neuron. Furthermore, (Goaillard et al. 2009; Norris et al. 2011) surveyed animal-to-animal variability in network and synaptic parameters and found significant correlations between the synaptic conductance of one of the components of the pyloric pacemaker kernel (the pyloric dilator (PD) neuron) to the onset phase of the follower lateral pyloric (LP) motor neuron. They also showed that a

modulator-activated inward conductance (I_{MI}) known to increase excitability in the LP neuron also correlated with the same PD synaptic conductance, suggesting that these parameters may be compensatory with respect to each other. Taken together, these results present a nice synergy between theoretical results and the physiology observed in the STN.

In order to compare the results observed in the STN to other preparations, it is important to consider the differences in the organization of its CPG's compared to other circuits. For example, the majority of the neurons within the pyloric CPG and gastric mill CPG networks of the STN are motor neurons, and these CPGs are not distributed circuits like the circuit that governs rodent hindlimb locomotion or the circuit that governs swimming in lampreys or tadpoles. Furthermore, because the core pacemaker of the pyloric CPG consists of a tightly coupled pair of neurons, there is a reduction in phase diversity across animals.

The leech heartbeat CPG is a well-characterized network in which we can easily measure premotor timing information and patterns of synaptic strength across animals (Norris et al. 2011). The heartbeat CPG is a segmentally distributed network with multiple premotor inputs onto motor neurons that vary in the synaptic conductances and display flexibility in their premotor phasing. In a previous study (Norris et al. 2011), we showed that there is considerable animal-to-animal variability in synaptic parameters, timing information as well as motor output. Unlike the STG, however, no simple correlations were found

between any single premotor input conductance and output phase of motor neurons in this system, yet in every preparation, stereotyped patterns of motor activity were observed. We concluded that each animal arrives at its own pattern of synaptic drive onto motor neurons that result in the appropriate motor output. One of the important goals of this thesis is to ascertain how timing information and patterns of synaptic strength interact to produce stereotyped patterns of output.

1.4 Leech Nervous System

The leech has long been a preparation in which overt behaviors could be analyzed at the cellular level. The reason this preparation has been favorable for studying the cellular control of behavior is its simple and accessible CNS. The leech CNS is composed of a headbrain, hindbrain and 21 segmental ganglia connected via a bundle of axons into a ventral nerve cord (Fig 1.1). The segmental ganglia contain approximately 200 pairs of neurons (Macagno 1980), and exert relatively autonomous control over their home segment by providing and receiving innervation through a pair of lateral roots that innervate the segmental muscles and structures. Each ganglion is stereotyped such that individual neurons are iterated across most segments and can be identified by soma size, location within a ganglion and finally by their characteristic electrical activity. Neurons within a segmental ganglion communicate by axons that run in the

FIG 1.1 Leech nervous and circulatory systems. *A:* The leech CNS consists of a head ganglion, 21 midbody segmental ganglia and a tail ganglion that communicate via bundles of axons called connectives. Each ganglion is indexed according to segment number. *B:* The primary vessels moving blood through the closed circulatory system of the leech are the passive dorsal sinuses, located dorsally and ventrally, and the bilateral heart tubes. The heart tubes express bilaterally asymmetric constriction patterns owing to segment-specific innervation from heart motor neurons found in the segmental ganglia. The ventral cord lies within the ventral sinus (adapted from Kuffler et. al. 1984).

Figure 1.1

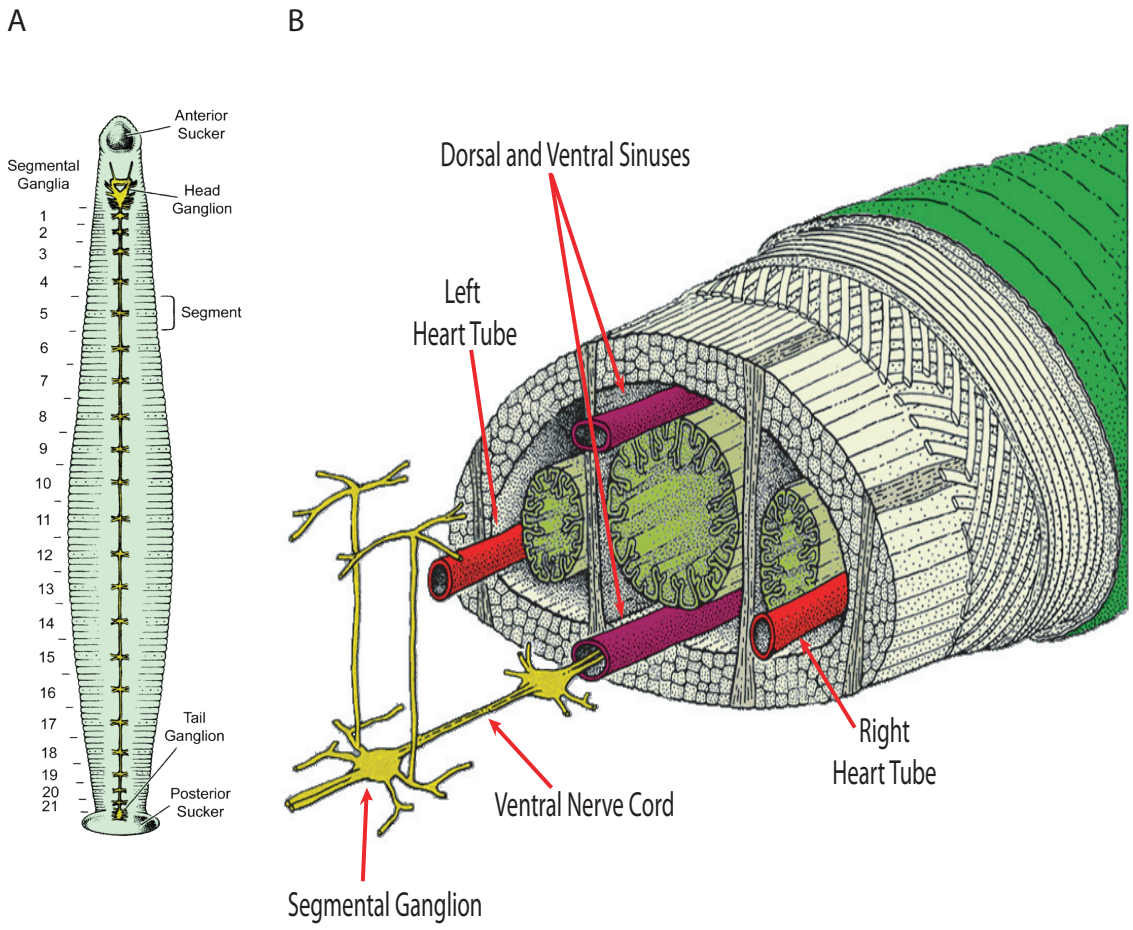
A
B
Anterior Sucker
Segmental Ganglia
Head Ganglion
1
2
3
4
5
6
7
8
9
10
11
12
13
14
15
16
17
18
19
20
21
Segment
Tail Ganglion
Posterior Sucker
Dorsal and Ventral Sinuses
Left Heart Tube
Right Heart Tube
Ventral Nerve Cord
Segmental Ganglion

connective bundles with adjacent ganglia and can receive descending/ascending information from the head/hindbrain neurons (Puhl and Mesce 2010) via their axons in the connectives. When referring to a neuron in a given segment, I will reference the segment number in parentheses (e.g. the HE(8) motor neuron refers to the heart motor neuron in segment 8).

1.5 The Leech Heartbeat CPG

The circulatory system of the leech is a closed system in which the primary vessels are the passive sinuses (dorsal and ventral) and the lateral heart tubes (Fig 1.1). The movement of blood through the leech is accomplished by the rhythmic constriction of the pair of lateral heart tubes (Thompson and Stent 1976a). The heart tube constriction patterns are bilaterally asymmetric, with one heart tube constricting with a rear-to-front progression (i.e., peristaltically) while the other constricts nearly synchronously along its length. The peristaltic heart tube generates a high systolic pressure (Hildebrandt 1988; Wenning et al. 2004a; Wenning et al. 2004b) compared to the synchronous heart, which generates a low systolic pressure. The heart tube constriction patterns are not permanent; there are regular switches in the constriction patterns every 20-40 cycles (Norris et al. 2006).

Although the hearts can generate a myogenic rhythm (Maranto and Calabrese 1984a; Thompson and Stent 1976a; b), the heart tubes generate patterned rhythmic activity as the result of ipsilateral segmental innervation arising from one of a pair of electrically coupled bilateral heart excitor (HE) motor neurons. The heart motor neurons are found in segments 3-18 and innervate the heart tubes in their segment only, forming cholinergic neuromuscular junctions (Maranto and Calabrese 1984a; b). The heart motor neurons are rhythmically active; the activity pattern of the heart motor neurons (i.e., the fictive motor pattern) is also bilaterally asymmetric, with heart motor neurons on one side producing a rear-to-front pattern activity while the other heart motor neurons fire with a near synchronous pattern of activity. Therefore, the bilateral activity of the heart motor neurons underlies the bilateral constriction patterns of the heart tubes.

The rhythmic activity of the heart motor neurons is the result of segment-specific ipsilateral innervation arising from premotor heart (HN) interneurons (Norris et al. 2007a; Thompson and Stent 1976b) that are components of the heartbeat CPG. The heart interneurons occur as bilateral pairs in segments 1-7 (Norris et al. 2006). Subsets of the HN interneurons are premotor in that they make inhibitory synaptic connections onto the heart motor neurons. A summary of the synaptic connections of the premotor interneurons onto a subset of the heart motor neurons that will be the focus of this thesis, the heart motor neurons in midbody segments 8, 10, 12 and 14, are shown in Figure 1.2. The firing pattern of the premotor interneurons is also bilaterally asymmetric, with HN

FIG 1.2 A bilateral circuit diagram showing a subset of the identified premotor heart (HN) interneurons [HN(3), HN(4), HN(6) and HN(7)] and their pattern of synaptic connections onto a subset of the HE motor neurons that are the focus of this thesis [(HE(8)-HE(14)]. Large circles represent cell bodies, whereas small colored circles represent inhibitory chemical synapses. Colored lines represent cell processes, and resistors represent electrical synapses between HE motor neurons within a given segment. Our standard color scheme for the premotor HN interneurons will be preserved throughout the thesis: dark blue for the HN(3), green for the HN(4), magenta for the HN(6) and cyan for the HN(7). The peristaltic mode will be coded in pink and the synchronous pattern will be coded in light blue.

Figure 1.2

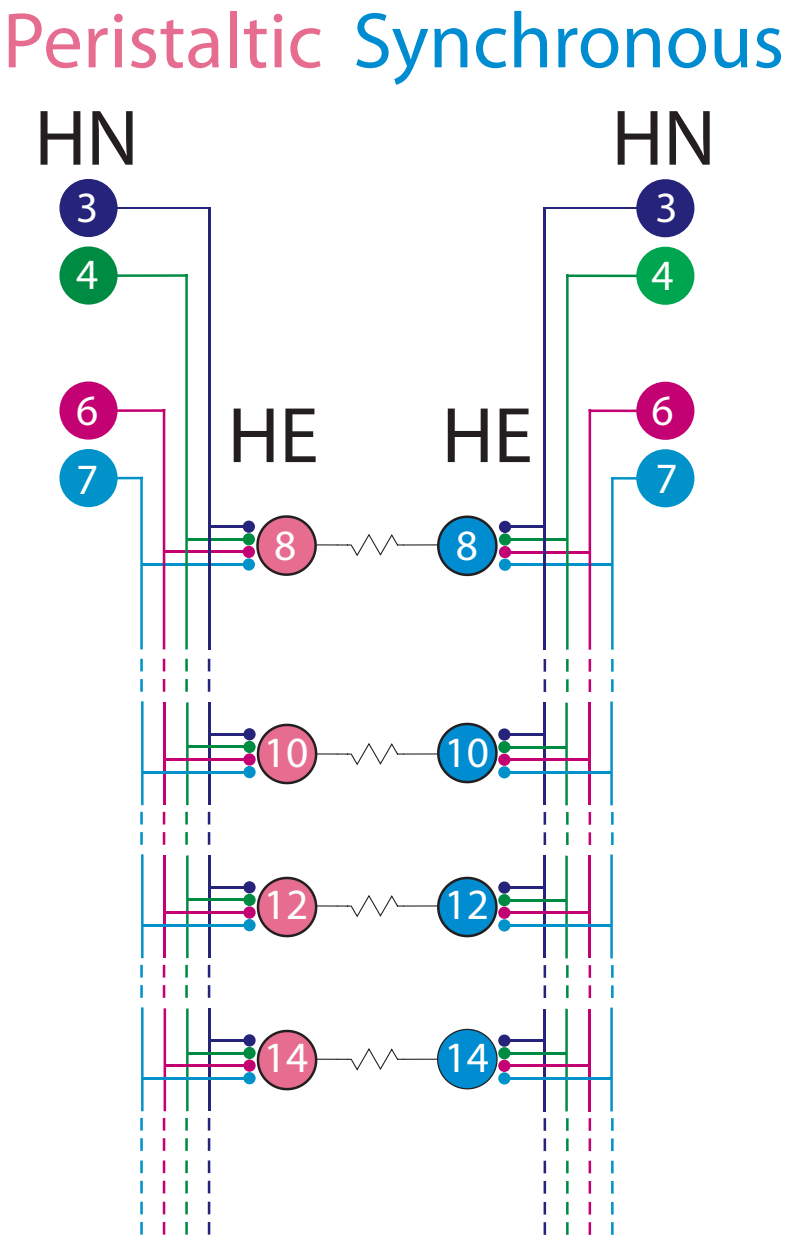
Peristaltic
Synchronous
HN
HN
3
4
6
7
HE
HE
3
4
6
7
8
8
10
10
12
12
14
14

interneurons on one side firing with a rear-to-front progression while the HN interneurons on the other side fire nearly synchronously.

Because of the accessibility of the leech nervous system, we have been able to describe quantitatively all aspects of the heart beat system from input to output (Norris et al. 2006; Norris et al. 2007a; b). For example, we have been able to quantify the timing of the heart motor neurons with respect to the heart interneurons as well as the patterns of synaptic strength that the premotor interneurons provide onto a heart motor neuron (Norris et al. 2011). Figure 1.3A shows simultaneous ipsilateral extracellular recordings from the HN(3), HN(4), HN(6) and HN(7) premotor interneurons along with the ipsilateral HE(8) and HE(12) motor neurons. In the beginning of the record, both the heart interneurons and the heart motor neurons were in the peristaltic mode; after a switch, the firing pattern of both the heart interneurons and the heart motor neurons switched into the synchronous mode. Recordings such as these allow us to quantify the firing pattern of both the heart interneurons and the heart motor neurons and represent them graphically in a phase diagram. Figure 1.3B shows a phase diagram measured by Norris et al. (2011) for the peristaltic and synchronous coordination modes for both the premotor heart interneurons as well as the HE(8) and HE(12) motor neurons. The phase diagrams also illustrate the intersegmental coordination between the HE(8) and the HE(12) motor neurons in the peristaltic and synchronous modes.

FIG 1.3 Determining the input and output temporal patterns of the HE(8) and HE(12) motor neurons. *A:* Simultaneous extracellular recordings were made of ipsilateral HN(3), HN(4), HN(6) and HN(7) premotor interneurons (inputs; color scheme as in Fig 1.2) and the HE(8) and HE(12) motor neurons (output; black) in both the Peristaltic (top traces) and Synchronous (bottom traces) coordination modes. *B:* Summary phase diagram of the premotor interneurons and the HE(8) and HE(12) motor neurons in the peristaltic (pink-outlined boxes) and synchronous (light blue-outlined boxes) coordination modes. For both motor neurons and interneurons, the average duty cycle is represented by the length of the box: the left edge indicates the average phase of the first spike of the burst, the right edge indicates the average phase of the last spike of the burst. Average phase is indicated by a vertical line within the box. Error bars are SDs. The phase diagram is constructed from measurements of activity relative to the middle spike of the ipsilateral HN(4) interneuron for both synchronous and peristaltic coordination modes. To align the ipsilateral phase diagrams, the synchronous HN(4) interneuron was assigned a phase of 0.51 as measured with respect to the peristaltic HN(4) interneuron in bilateral recordings (Norris et al., 2006). All other synchronous neurons were then offset by the same amount as the phase of the synchronous HN(4) interneuron. Figure modified from Norris et al., 2011.

Figure 1.3

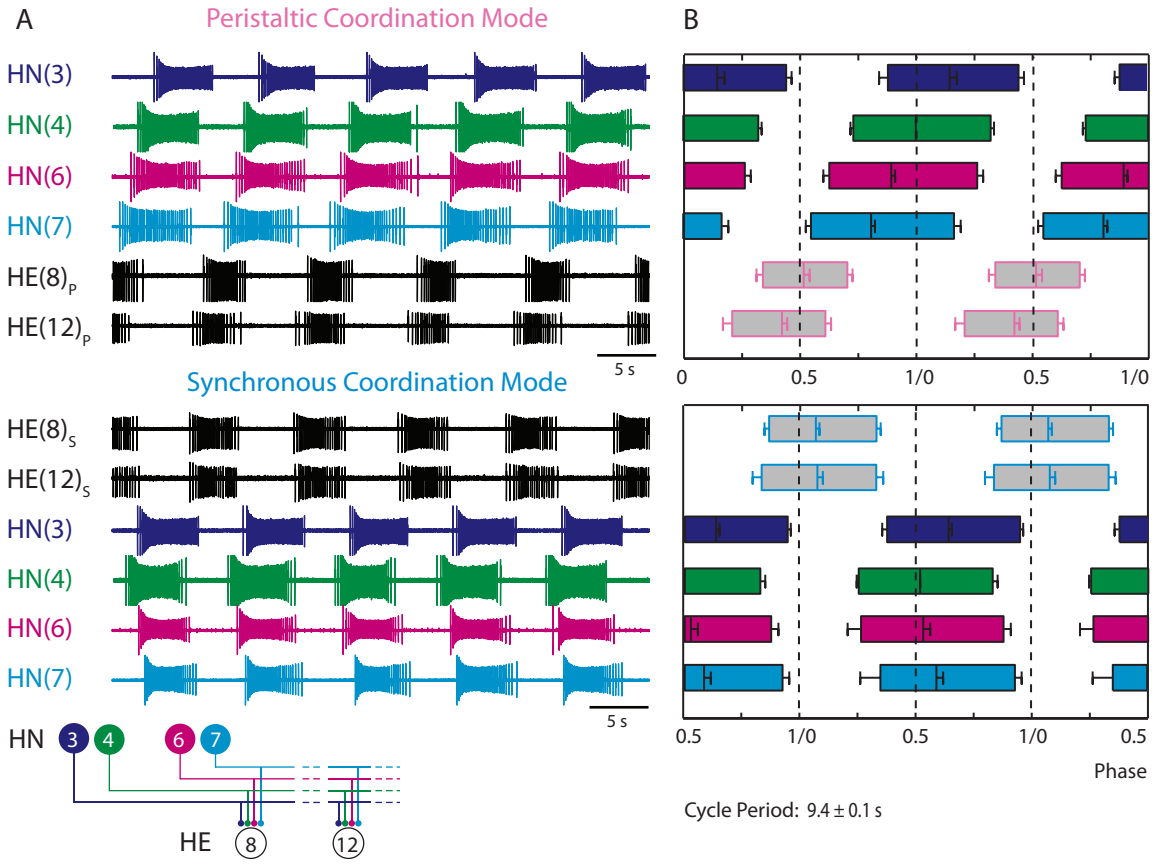
A
Peristaltic Coordination Mode
HN(3)
HN(4)
HN(6)
HN(7)
HE(8)P
HE(12)P
5 s
Synchronous Coordination Mode
HE(8)S
HE(12)S
HN(3)
HN(4)
HN(6)
HN(7)
5 s
HN 3 4 6 7
HE 8 12
B
0 0.5 1/0 0.5 1/0
0.5 1/0 0.5 1/0 0.5
Phase
Cycle Period: 9.4 ± 0.1 s

Figure 1.4 shows how patterns of synaptic strength from the premotor interneurons onto the heart motor neurons can be measured. Typically, Norris et al. (2011) recorded simultaneously from each of the premotor HN interneurons while voltage clamping a post-synaptic heart motor neuron. Their measure of synaptic strength was the average peak postsynaptic current timed to each premotor input. As can be seen, trends in the patterns of synaptic strengths can be observed across segments. Experiments such as these allow us to quantify both timing information of the premotor inputs (termed the temporal pattern of inputs) and the patterns of synaptic strengths of the premotor interneurons (termed the synaptic strength profile). One of the goals of this thesis will be to address the relative contributions of the temporal patterns and synaptic strength profiles to the production of functional peristaltic and synchronous motor output.

1.6 Heart Motor Neurons

The heart excitor (HE) motor neurons occur as bilateral pairs in midbody segments 3-18. They are stereotyped in their morphology across segments (Shafer and Calabrese 1981). The heart motor neurons are monopolar; a single large neurite exits the posterior pole of the soma and proceeds laterally towards the ganglionic midline. Before reaching the midline, the neurite bends, forming a semicircle, before exiting the ganglion through the ipsilateral anterior nerve. From this primary neurite, several secondary processes branch off, forming fine

FIG 1.4 Determining the absolute and relative synaptic strength of each input to a heart motor neuron. *A:* An HE(12) motor neuron was recorded in voltage clamp (holding potential: -45 mV) simultaneously with extracellular recording from the ipsilateral HN(3), HN(4), HN(6) and HN(7) premotor heart interneurons (standard color scheme). *B*: Spikes from 11 HN bursts (including the ones illustrated here) were used to generate the spike-triggered averages of IPSCs in the HE(12) motor neuron and, subsequently, in the HE(8) motor neuron in the same preparation. Upward arrows indicate the time of the triggering HN spike, and the downward arrows indicate the peak of the averaged IPSC used to measure amplitude. Iconic unilateral circuit diagram at bottom right identified the recorded neurons. Figure modified from Norris et. al., 2011.

Figure 1.4

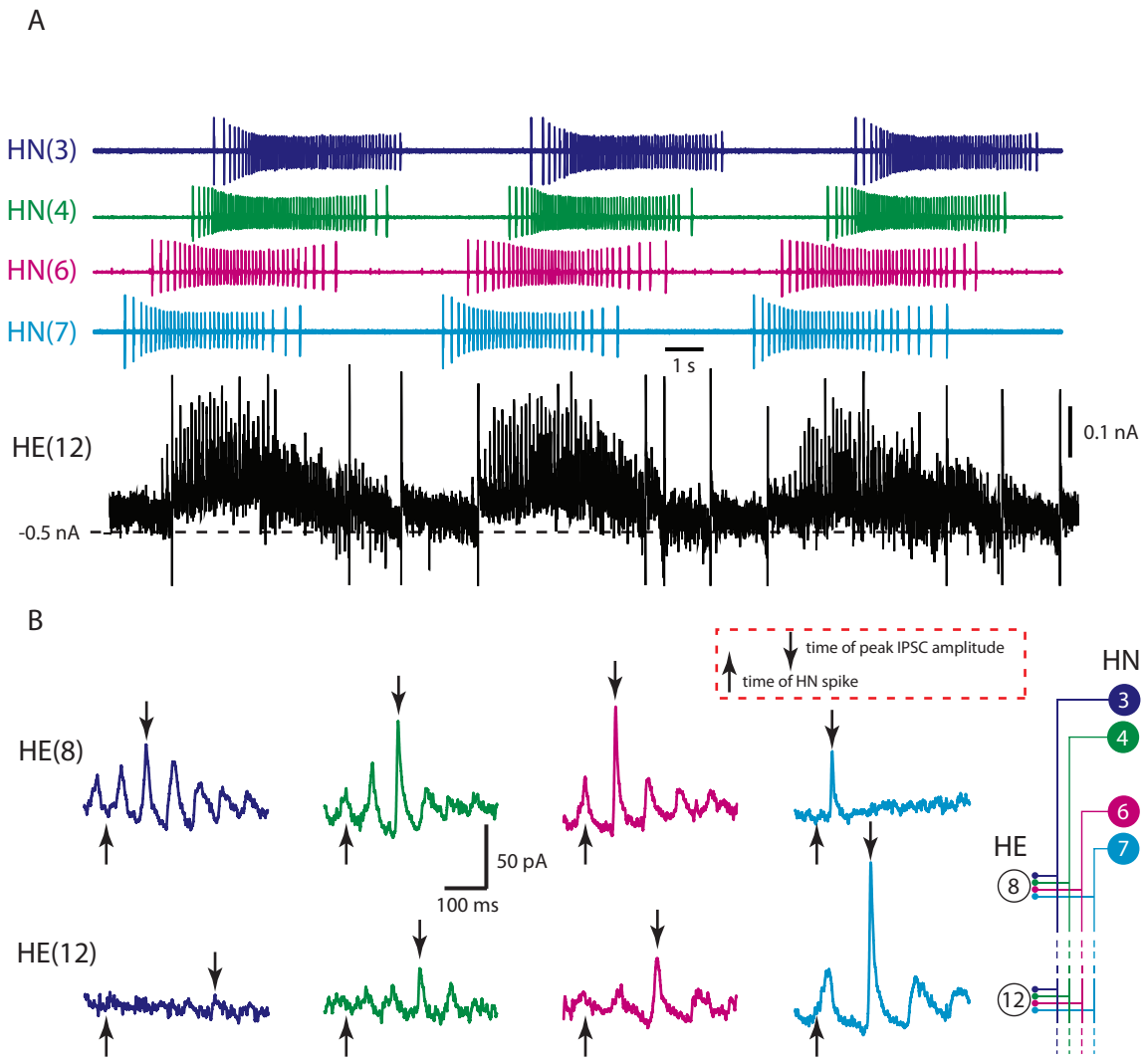
A
HN(3)
HN(4)
HN(6)
HN(7)
1 s
HE(12)
0.1 nA
-0.5 nA
B
time of peak IPSC amplitude
time of HN spike
HN
3
4
6
7
HE
8
12
HE(8)
50 pA
100 ms
HE(12)

branches that approach, and in some cases cross, the ganglionic midline. These fine branches form a uniplanar sheet near the dorsal surface. The morphology of the heart motor neurons is consistent from animal to animal.

The fine branches of the heart motor neurons provide opportunities for synaptic contacts and electrical contacts between heart motor neurons and from heart interneurons onto heart motor neurons (Tolbert and Calabrese 1985). Double fills of the pair of heart motor neurons with horseradish peroxidase showed extensive overlap of the fine arbors of heart motor neurons separated by a gap of 6 nm, suggesting a putative site for the electrical contacts between the heart motor neurons. Double fills of heart motor neurons and heart interneurons has shown that several of the heart motor neuron fine processes surround processes from the heart interneurons, suggesting that these are the putative synaptic sites for the heart interneurons onto the heart motor neurons.

The activity of the heart motor neurons entrains the myogenic constrictions of the bilateral heart tubes (Maranto and Calabrese 1984a; b). The heart motor neurons form typical neuromuscular junctions, in which the heart motor neuron releases Acetylcholine onto the heart. Each spike in a heart motor neuron elicits a unitary excitatory potential in a muscle cell, with the potentials summing to produce a plateau-like regenerative potential in the heart tubes. In the absence of input from the heart motor neurons, the heart tubes produce an irregular myogenic rhythm. Therefore, the heartbeat CPG, which drives the activity of the heart motor neurons to impose the CPGs activity onto the heart

tubes, is ultimately responsible for establishing the heart tube constriction patterns observed.

1.7 Canonical Heart Motor Neuron Ensemble Model

Experiments such as those described in Figure 1.4 were used to provide a quantitative description of the temporal pattern and synaptic strength profiles for all 16 pairs of heart motor neurons (Norris et al. 2006; Norris et al. 2007a; b). To determine the extent to which a temporal pattern and synaptic strength profiles could account for the intersegmental coordination of heart motor neurons during the fictive motor pattern, we developed a first-generation model of the ensemble of the heart motor neurons (García et al. 2008). The model motor neurons were single-compartment, conductance-based models that contained a simple set of voltage-gated conductances compatible with spontaneous firing in the absence of synaptic inhibition and silence during bouts of interneuron-mediated inhibitory synaptic potentials (Appendix A). Electrical coupling between model motor neurons was also included. By keeping the intrinsic properties of the model motor neurons to a minimum, it was possible to determine the extent to which synaptic input and electrical coupling acting together could account for the peristaltic and synchronous coordination modes observed in the living system in the absence of a substantive contribution from the motor neurons themselves. The model reproduced the general trends of intersegmental coordination, but the match with the living system was not quantitatively accurate, as seen in Figure 1.5. Thus realistic (that is, experimentally derived) inputs do not produce

FIG 1.5 Bilateral middle-spike phase diagram comparing the absolute phase relations of a canonical model of the ensemble of the HE motor neurons (dashed line) with that of the living system (solid line) with the peristaltic premotor HN(4) interneuron as the phase reference for segments seven through fifteen. Shown are two synchronous (blue) and one peristaltic phase curve for both the model and the living system. The phase of the peristaltic premotor HN(4) interneuron is shown as a slanted green line; the synchronous premotor HN(4) interneuron is shown as a dashed green line for clarity. The slope of the line represents the intersegmental conduction delays from segment to segment. The use of a common phase reference illustrates the difference in phase between the model and the living system. A major goal of this thesis will be to understand how motor neuron intrinsic properties present in the living motor neurons and not accounted for in the model contribute to the living system phases observed. Figure modified from García et al., 2008.

Figure 1.5

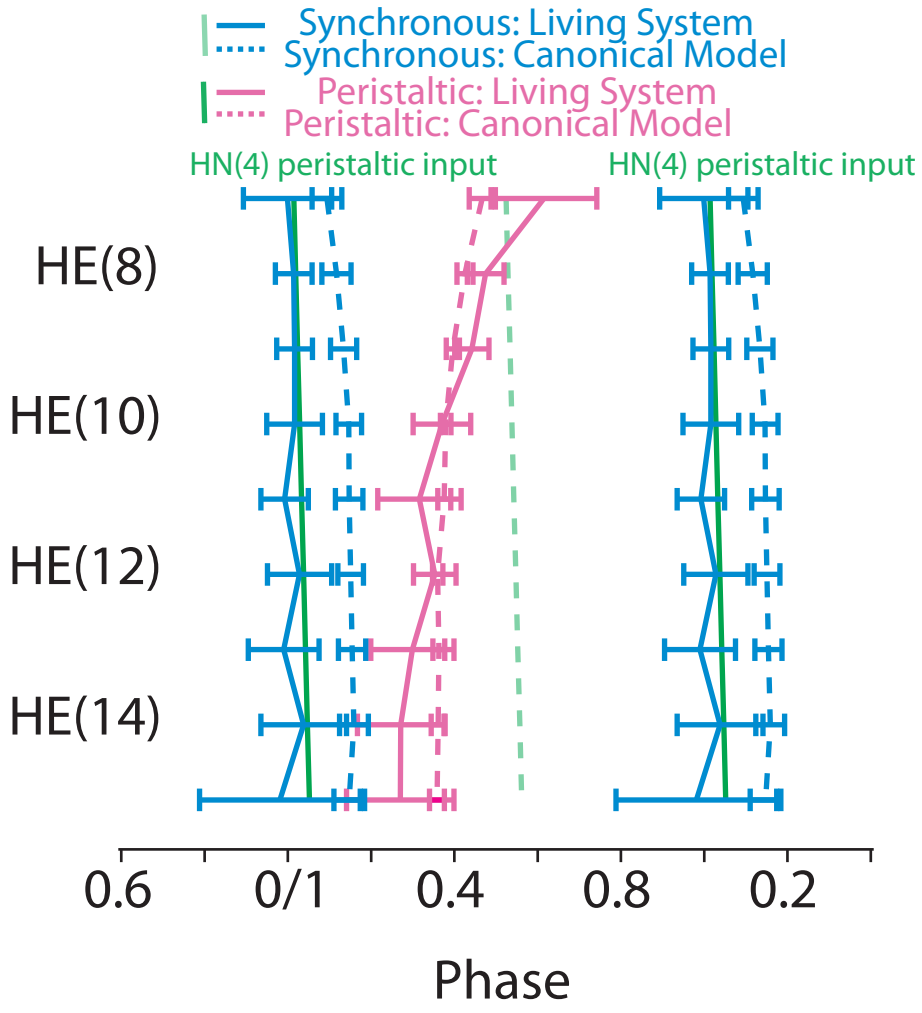
Synchronous: Living System
Synchronous: Canonical Model
Peristaltic: Living System
Peristaltic: Canonical Model
HN(4) peristaltic input
HN(4) peristaltic input
HE(8)
HE(10)
HE(12)
HE(14)
0.6
0/1
0.4
0.8
0.2
Phase

similarly realistic output in the model motor neurons, suggesting that motor neuron intrinsic properties may contribute to their output phase in response to a segmental input pattern. An important goal of this thesis was to ascertain what this contribution might be.

1.8 Thesis Overview

Chapter 2 describes how the heart motor neuron intrinsic properties and within-segment electrical coupling contribute to the output phasing observed in the living system. This chapter has been accepted to *The Journal of Neurophysiology*. Chapter 3 describes how timing information and patterns of synaptic strength from the premotor heart interneurons coordinate the heart motor neurons into their intersegmental motor patterns. This chapter is being prepared for submission to *The Journal of Neuroscience*. Chapter 4 presents a general discussion of this work that attempts to put my work into a larger context.

The primary goals of this thesis were: to determine the functional role, if any, that motor neuron intrinsic properties have in the generation of rhythmic motor output and to determine the relative contribution of timing information and the profile of synaptic strength is producing appropriate motor neuron phasing. I pursued these goals both modeling, and a hybrid-systems analysis in

which a virtual model of the heart interneuron to heart motor neuron synapses was introduced to heart motor neurons in the living system using the dynamic clamp technique. I present evidence that heart motor neuron intrinsic properties do play a functional role in assuming their output phase with respect to a segmental input pattern. I also show how timing information and patterns of synaptic strengths from the premotor heart interneurons combine to produce the stereotyped peristaltic and synchronous intersegmental motor patterns observed in the living system.

CHAPTER 2

CONTRIBUTION OF MOTOR NEURON INTRINSIC PROPERTIES TO FICTIVE MOTOR PATTERN GENERATION

ABSTRACT

Previously, we reported a canonical ensemble model of the heart motor neurons that underlie heartbeat in the medicinal leech. The model motor neurons contained a minimal set of electrical intrinsic properties and received a synaptic input pattern based on measurements performed in the living system. Although the model captured the synchronous and peristaltic motor patterns observed in the living system, it did not match quantitatively the motor output observed. Because the model motor neurons had minimal intrinsic electrical properties, the mismatch between model and living system suggests a role for additional intrinsic properties in generating the motor pattern. We used the dynamic clamp to test this hypothesis. We introduced the same segmental input pattern used in the model to motor neurons isolated pharmacologically from their endogenous input in the living system. We show that, although the segmental input pattern determines the segmental phasing differences observed in motor neurons, the intrinsic properties of the motor neurons play an important role in determining their phasing, particularly when receiving the synchronous input pattern. We then used trapezoidal input waveforms to show that the intrinsic properties present in the living system promote phase advances when compared to our

model motor neurons. Electrical coupling between heart motor neurons also plays a role in shaping motor neuron output by synchronizing the activity of the motor neurons within a segment. These experiments provide a direct assessment of how motor neuron intrinsic properties interact with their premotor pattern of synaptic drive to produce rhythmic output.

INTRODUCTION

Rhythmic motor behaviors, such as swimming and walking, are generated by networks of rhythmically active neurons called central pattern generators (CPGs, (Marder and Calabrese 1996)). A defining characteristic of these networks is their ability to generate a rhythmic pattern in *in vitro* preparations in which sensory feedback has been removed (i.e., the fictive pattern). The majority of CPG's provide a pattern of rhythmic synaptic activation to the motor neurons that underlie the behavior. While much work has focused on identifying and analyzing elements of these rhythmically active networks, less is known about how motor neurons themselves contribute to the generation of the motor pattern.

Some studies have shown that motor neurons possess intrinsic properties that may affect motor pattern generation. For example, motor neurons in cats (Lee and Heckman 1998) and turtles (Hounsgaard and Kiehn 1989) exhibit bi-stable membrane properties (i.e., a stable membrane potential at rest and at

depolarized levels) which may confer upon them the ability to sustain motor output in the absence of synaptic input. Kiehn et al. (2000) characterized a hyperpolarization-activated current, I_h, present in motor neurons in the neonatal rodent spinal cord. They showed that this current advanced the transition of a motor neuron from its inhibited phase to its firing phase, suggesting that this current could confer upon a motor neuron an ability to "escape" from ongoing inhibitory synaptic input and thus influence motor output.

Electrical coupling between motor neurons can also affect motor pattern generation. For example, studies have shown that there is electrical coupling between hypoglossal motor neurons associated with breathing (Rekling et al. 2000) and tongue movements (Sharifullina et al. 2005) as well as among motor neurons in *Xenopus* embryos (Perrins and Roberts 1995). Furthermore, when gap junctions were blocked in *Xenopus* embryos, (Zhang et al. 2009) noted that the burst durations of motor neurons increased, resulting in alteration of rostro-caudal delays during fictive swimming. These results indicate that electrical coupling in these preparations may contribute to the motor output observed *in vitro*.

Elucidating the functional significance of neuronal intrinsic properties has remained elusive, however, owing in part to a lack of detailed information about the activity patterns and synaptic connections of premotor interneuronal networks that provide the synaptic information to the motor neurons in these systems. For example, in the absence of synaptic input, the motor neurons

involved in fictive scratch in turtles exhibit large-amplitude voltage fluctuations in response to current injections indicating they possess complex intrinsic properties (Alaburda et al. 2005). When the premotor network driving fictive scratch is activated, however, the voltage fluctuations observed are diminished due to the synaptic conductance impinging upon the motor neurons. This result implies that the intrinsic properties responsible for the voltage oscillations make a minor contribution to the motor pattern observed *in vitro*. These results suggest that a detailed description of the premotor pattern of synaptic drive onto these motor neurons is required in order to determine the role of motor neuron intrinsic properties in the generation of the fictive scratch.

Invertebrates, with their simple and accessible nervous systems, have long been useful for elucidating synaptic connectivity within central pattern generating networks (Nusbaum and Beenhakker 2002) and how motor patterns are modulated and selected (DeLong et al. 2009). Here we use the leech heartbeat CPG to assess how motor neuron intrinsic properties and electrical coupling contribute to rhythmic motor output.

The leech heartbeat system has been described in detail (Kristan et al. 2005; Thompson and Stent 1976a; b; c), so we provide a brief summary here. Blood flow in the leech circulatory system is accomplished by the rhythmic constriction of a pair of longitudinal vessels, the lateral heart tubes (referred to as 'hearts'). The hearts are coordinated such that one heart constricts with a rear-to-front progression (i.e., peristaltically), while the other heart constricts nearly

synchronously along its length. The asymmetry in the constriction patterns is not permanent; rather, there are regular switches in the constriction patterns roughly every 20-40 cycles. The constriction patterns of the hearts are the result of excitatory drive arising ipsilaterally from segmental heart (HE) motor neurons (Thompson and Stent 1976a). Heart motor neurons occur as electrically coupled bilateral pairs in mid-body segmental ganglia 3 through 18 of the 21 midbody ganglia in the ventral nerve cord. The heart motor neurons receive rhythmic inhibitory input from ipsilateral premotor heart (HN) interneurons that are components of the heartbeat CPG. The firing pattern of the heart motor neurons (i.e., the fictive motor pattern) is also bilaterally asymmetric: motor neurons on one side fire with a rear-to-front progression of activity while the heart motor neurons on the other side fire nearly synchronously with the appropriate side-to-side coordination (Wenning et al. 2004a; Wenning et al. 2004b). The firing pattern of the premotor heart (HN) interneurons (i.e, the temporal pattern) is bilaterally asymmetric, with heart interneurons on one side firing with a rear-to-front progression, while the interneurons on the other side fire nearly synchronously.

Previously, Norris and colleagues (2006; 2007a; b) quantified the individual components of presynaptic input to the heart motor neurons as well as their output. In the first of a series of studies, they quantified the temporal patterns (peristaltic and synchronous) of the heart interneurons. They then characterized the pattern of synaptic strengths arising from each of the premotor interneurons onto their appropriate heart motor neuron targets (i.e., a heart

motor neurons synaptic strength profile). Finally, they quantified the phasing of the heart motor neurons with respect to the premotor interneurons. These studies led to the development of a first-generation model of the ensemble of heart motor neurons (García et al. 2008). The model motor neurons were single-compartment, conductance-based models and were given a minimal set of voltage-gated conductances. The synaptic input pattern introduced to the model motor neurons was based on the Norris et al. experiments (2006; 2007a; b) just described. Although this first-generation model exhibited the general trends in activity (i.e., a peristaltic and synchronous pattern of activity) as those observed in the living system, a quantitative comparison revealed substantive differences in phase between the model and the living system (Fig. 1). For example, in the peristaltic mode (pink lines), the model motor neurons do not capture the amount of peristaltic phase progression observed in the living system; in anterior segments (e.g., 8), the phase of the model motor neurons leads the average of that in the living system, whereas in more posterior segments (e.g., 14), the phase of the model motor neuron lags the average of that in the living system. In the synchronous mode (blue lines), model motor neuron activity occurs nearly synchronously, but the phase of the model motor neurons lags the average of that in the living system in all segments illustrated in Figure 1. These results raise the possibility that the intrinsic properties of the heart motor neurons in the living system, which were not accounted for in our model motor neurons, may be critical for their appropriate phasing.

FIG 2.1. Leech heartbeat fictive motor pattern: comparison of intersegmental coordination between the living system and a canonical ensemble model of the heart motor neurons. A bilateral phase diagram for segments 7 through 15 compares the absolute phase relations (see Methods) of our canonical model of the heart motor neurons (dashed lines) with that of the living system (solid lines), using the peristaltic premotor HN(4) interneuron as the phase reference. In this abbreviated representation of a phase diagram, only average middle spike phase (± sd) is shown. Two synchronous (blue) and one peristaltic (phase) phase curves for the living system are shown and corresponding curves (black dashed) for the model is superimposed. The phase reference, the peristaltic HN(4) interneuron, is shown as a slanted green line; the synchronous HN(4) interneuron is shown as a dashed green line. The slope of the line gives the intersegmental conduction delays from segment to segment. The use of a common phase reference makes apparent the difference in phase between the model and the living system. In the peristaltic coordination mode, model motor neurons do not capture the large intersegmental phase progression observed in the living system, while in the synchronous coordination mode, model motor neurons capture the synchronous intersegmental coordination, but their middle spike phase is significantly delayed with respect to the living system. The mismatches in phase observed suggest that factors in addition to synaptic input patterns influence motor neuron phase. Panel modified from García et al. (2008).

Figure 2.1

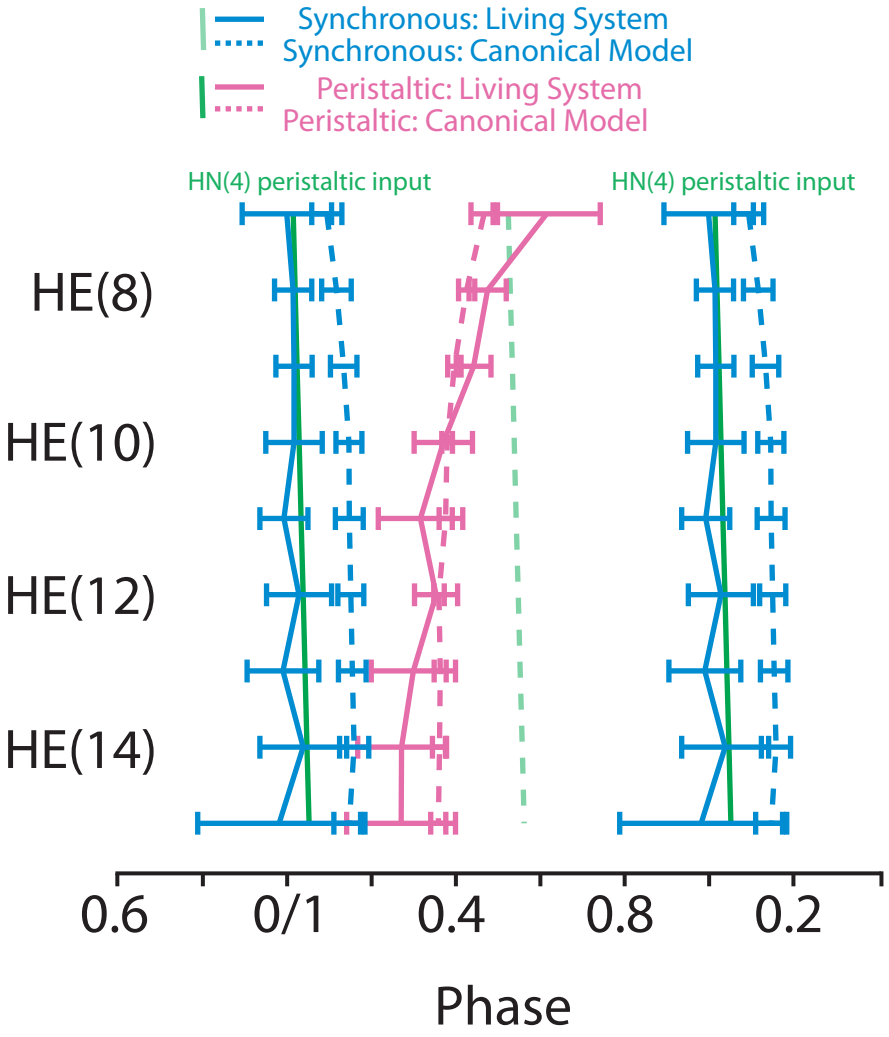
Synchronous: Living System
Synchronous: Canonical Model
Peristaltic: Living System
Peristaltic: Canonical Model
HN(4) peristaltic input
HN(4) peristaltic input
HE(8)
HE(10)
HE(12)
HE(14)
0.6
0/1
0.4
0.8
0.2
Phase

To test this hypothesis, we used the dynamic clamp technique (Prinz et al. 2004; Sharp et al. 1993) to construct hybrid networks in which heart motor neurons in the living system received the same synaptic conductance waveform introduced into our model motor neurons (Fig. 2). We show that, although the segmental input pattern determines the phasing differences observed in motor neurons in segments 8 through 14, the intrinsic properties of the motor neurons also influence their phasing in the hybrid system. Indeed, appropriate phasing can be achieved when motor neurons receive the synchronous segmental input patterns. We also explore how the heart motor neurons in the living system integrate their inputs differently from our canonical model motor neurons. Finally, we show that electrical coupling between heart motor neurons can influence their phasing. Taken together, these results show that motor neurons can be active participants in motor pattern generation.

METHODS

Terminology

Heart (HE) motor neurons and heart (HN) interneurons are indexed according to midbody ganglion number [e.g., HE(8), HN(4)]. In all experiments, we used bilateral pairs of heart motor neurons. We introduced the peristaltic input pattern to one heart motor neuron and the synchronous input pattern to

the other heart motor neuron. Therefore, we omit body-side indexing and labeled heart motor neurons as receiving the peristaltic or synchronous input pattern.

Animals and Solutions

Leeches (*Hirudo sp.*) were purchased from a commercial supplier (Leeches USA, Westbury, NY) and maintained in artificial pond water at 15° C. Animals were anesthetized in ice, then dissected in chilled saline. Individual ganglia from segments 8, 10, 12 and 14 were dissected and pinned out, ventral surface up, in 35 mm Petri dishes lined with Sylgard™ (184, Dow Corning, Midland MI). The ventral sheath of the ganglion was removed in all experiments. We superfused the preparation with leech saline containing (in mM: 115 NaCl, 4 KCl, 1.8 glucose, 10 HEPES buffer and 1.8 $CaCl_2$ adjusted to a pH of 7.4 using NaOH) at 1-2 ml/min in a bath volume of 0.5-1 ml. All experiments were performed at room temperature (20-25° C). In most of the experiments included in this study, 10^{-4} M bicuculline methiodide (Sigma-Aldrich, Allentown, PA) was added to the leech saline to block inhibitory synaptic input to heart motor neurons (Cymbalyuk et al. 2002). In other experiments, $CaCl_2$ was replaced with an equimolar amount of $MnCl_2$ (Sigma-Aldrich) to block the premotor inputs.

Intracellular Recording Techniques and Data Acquisition

Heart motor neurons were identified based on soma location within the ganglion, soma size and finally by their characteristic activity of bouts of firing interrupted by barrages of IPSPs. Intracellular voltage recordings from heart motor neurons were made using sharp intracellular microelectrodes (~25-40 MΩ filled with 2 M KAc, 20 mM KCl) made from borosilicate glass (1.0 mm outer diameter; 0.75 mm inner diameter; AM Systems, Sequim, WA). Intracellular recordings and current injections were performed using an Axoclamp-2A amplifier (Molecular Devices, Sunnyvale, CA) in Discontinuous Current Clamp (DCC) mode using a sampling rate of 2.5-3.0 kHz. To ensure electrode settling, the electrode potential was monitored with an oscilloscope. Output bandwidth of the amplifier was 0.3 kHz. Data were digitized (10 kHz sampling rate) using a digitizing board (Digi-data 1200 Series Interface, Molecular Devices, Sunnyvale, CA) and acquired using pCLAMP software (Molecular Devices) on a personal computer (Dell, Round Rock, TX).

In all experiments, both heart motor neurons in a given ganglion were impaled and recorded simultaneously. After penetration, the input resistance of both cells was measured using -0.3 nA pulses. We did not proceed with experiments unless the input resistance of both motor neurons was > 30 MΩ, and the difference in input resistance between the two motor neurons was < 15 %. Upon termination of the experiment, the microelectrode was withdrawn from the cell and the electrode potential was recorded. Only experiments in which the

electrode potential was within $\pm$ 5 mV of 0 mV were accepted in this study. Therefore, membrane potential are accurate to $\pm$ 5 mV.

Standard heart motor neuron ensemble model

We compared data from our physiological experiments to a model of the entire ensemble of heart motor neurons previously developed by García et al. (2008). Briefly, the motor neurons in this model were single-compartment, conductance-based models whose membrane potential (V) is given by the following current-balance equation:

$$C\frac{dV}{dt} = -(I_{Na} + I_P + I_{KA} + I_{K1} + I_{K2} + I_{leak} + I_{coup} + I_{Syn} + I_{inject})$$

where t is time, C is the total membrane capacitance, I_{leak} is the leak current, I_{coup} is the current due to electrical coupling between the motor neurons, I_{Syn} is the sum of the inhibitory synaptic currents arising from each of the premotor inputs and I_{inject} is any injected current. The model motor neurons contained five voltage-dependent ionic currents: *1*) a fast Na^+ current (I_{Na}), *2*) a persistent Na^+ current (I_P), *3*) a fast transient K^+ current (I_{KA}), *4*) an inactivating delayed rectifier K^+ current (I_{K1}) and *5*) a noninactivating delayed rectifier K^+ current (I_{K2}). The Hodgkin-Huxley equations (Hodgkin and Huxley 1952) describing

these voltage-gated currents were the same as those used in a model of an oscillator heart interneuron model (Hill et al. 2001). Each motor neuron was modeled as an isopotential cylinder whose length and diameter were both 60 μm with a specific membrane resistance of 1.1 Ωm^2 and a specific membrane capacitance of 0.05 Fm^{-2}. With these parameters, the input resistance of a model motor neuron was 97 MΩ. The maximal conductances of the individual ionic currents as well electrical coupling were set empirically so that the activity of the model motor neurons mimicked those observed during intracellular recordings of heart motor neurons in the absence of synaptic input .(García et al. 2008)

The model motor neurons received an inhibitory synaptic input pattern that consisted of both timing information and a pattern of synaptic strengths; both components were determined from physiological experiments of the type performed by Norris and colleagues (2006; 2007a; b) as described below.

For the model motor neurons, the firing pattern of the premotor interneurons (referred to here as the temporal pattern) was taken from 60 s of simultaneous extracellular recordings of the ipsilateral HN(3), HN(4), HN(6) and HN(7) premotor interneurons in both the peristaltic and synchronous coordination modes, as in Norris et al. (2006). The peristaltic and synchronous input patterns were aligned to each other to create a bilateral input pattern – left synchronous-right peristaltic – by assigning a phase of 0.0 to the middle spike of the first peristaltic HN(4) premotor interneuron burst (therefore, the peristaltic HN(4) premotor interneuron is our absolute phase reference) and a phase of

0.506 to the middle spike of the first burst of the synchronous HN(4) premotor interneuron. These phase values match the average phase difference between the two HN(4) interneurons as measured in the living system (Norris et al. 2006). Each segmental pair of model motor neurons received the same temporal pattern (one peristaltic, one synchronous) offset by an intersegmental conduction delay of 20 ms per segment. Therefore, the model heart motor neurons in segment 12 receive the same temporal pattern as the model heart motor neurons in segment 8, offset by 80 ms. The period of the input pattern was 4.3 s (the range of periods measured in the living system is 4 to 8.5 s; average period = 5.3 s (Norris et al. 2006)). Because the timing information used in our temporal pattern came from a living preparation, the temporal pattern is not precisely regular and therefore the average phases presented for the ensemble model display a variance.

The distribution of synaptic conductances elicited by each of the premotor heart interneurons in a postsynaptic heart motor neuron (referred to here as a heart motor neurons synaptic strength profile) was also derived from experiments in the living system, described in Figure 1*B* of Norris and et al. (2007b).They recorded from each of the premotor heart interneurons, as described above, and then voltage clamped a series of ipsilateral heart motor neurons. They recorded spontaneous IPSCs in the heart motor neurons arising from activity in the premotor interneurons. From these recordings, they generated spike-triggered averages of the IPSCs for each presynaptic heart interneuron to each heart motor neuron. They selected the peak of the spike triggered average trace as their measure of an individual premotor heart

interneurons synaptic input. These peak IPSCs were then converted to conductances (E_{Syn}= -62.5 mV; (Angstadt and Calabrese 1991)). They then computed the average synaptic conductance across animals and expressed these averages as peak synaptic conductances ($g_{SynHN(i)}$). There is no difference in the synaptic strength profile between the synchronous and peristaltic coordination modes (Norris et al. 2007b). The set of 4 maximal conductances ($g_{SynHN(i)}$) is unique to each segmental motor neuron pair, thus each motor neuron pair has a unique synaptic strength profile. Each model motor neuron received their segment-specific synaptic strength profile, as in Figure 3 of García et al. (2008). Each presynaptic heart interneuron spike elicited a unitary conductance that followed a double exponential function scaled by the synaptic weight for that input in that motor neuron ($g_{SynHN(i)}$). The model computes $g_{Syn}(t)$ from the sum of the 4 individual inhibitory synaptic conductances ($g_{SynHN(i)}$) associated with a particular presynaptic input HN_i. The heart motor neuron ensemble model with standard parameters (García et al. 2008) is referred to as the canonical ensemble model.

The heart motor neuron ensemble model was implemented in GENESIS (GEneral NEural Simulator System), with each model motor neuron receiving its segment-appropriate temporal pattern and synaptic strength profile. We ran the model for 60 s of model time. The model used the Euler integration method with a time step of 0.0001 s. The 13 bouts of inhibitory synaptic input sculpted 12 bursts of activity of the model motor neurons. We used these 12 bursts to assess

the phase of the model fictive motor pattern (see below). We recorded and saved the computed synaptic conductance waveforms arising from each premotor HN interneuron as well as their sum ($g_{SynTotal}$; Fig. 2) in each motor neuron for subsequent use in the dynamic clamp (see below).

Hybrid System Design and Implementation

We used the dynamic clamp technique (Prinz et al. 2004) to produce a virtual version of the heart interneuron to heart motor neuron synapse. The dynamic clamp both computes and injects, in real time (time step: 0.0001 s), a model of the synaptic current (I_{Syn}) based on the recorded intracellular membrane potential (V_m), a conductance ($g_{Syn}(t)$) and a reversal potential (E_{Syn}) according to Ohms Law. Because we are linking a model of this synapse with heart motor neurons in the living system, we refer to these preparations as hybrid systems. The virtual synapse was implemented according to the following equation:

$$I_{Syn} = \sigma g_{Syn}(t)(V_m - E_{Syn})$$

where I_{Syn} is the synaptic current, $g_{Syn}(t)$ is the time varying synaptic conductance waveform representing the sum of all the individual synaptic inputs to a model motor neuron, σ is used to scale $g_{Syn}(t)$, V_m is the membrane potential

of the motor neuron, and E_{Syn} is the synaptic reversal potential (Angstadt and Calabrese 1991). To generate the synaptic conductance waveforms introduced in our hybrid system experiments, we extracted $g_{Syn}(t)$ from canonical ensemble model simulations (see above). For simplicity, we label $g_{Syn}(t)$ as g_{Syn} in figures and text. Figure 2*A* shows how g_{Syn} was assembled by summing the individual time-varying synaptic conductance waveforms from each input to an HE(10) motor neuron pair. Figure 2*A* also illustrates the difference in the total synaptic conductance trajectory (g_{Syn}, black trace) between the peristaltic (upper panel) and the synchronous (lower panel) modes. In the peristaltic mode, the synaptic conductance trajectory rises and falls slowly because the firing of the premotor interneurons are spread out, with the HN(7) interneuron leading the HN(3) interneuron, resulting in a gradual rise and decay of the synaptic conductance. In the synchronous mode, however, the synaptic conductance trajectory rises and falls more precipitously because the firing of the premotor interneurons occurs at nearly the same time, resulting in a much more rapid rise and decay of the synaptic conductance envelope. The synaptic conductance waveforms used in our hybrid system experiments were the same as in the ensemble model except they were scaled by σ. The scaling factor allowed us to increase the overall synaptic conductance while preserving the relative synaptic strength of the individual premotor synaptic conductances. Unless indicated otherwise, the canonical segmental input pattern was used in both the dynamic clamp and in the ensemble model.

FIG 2.2. Hybrid system design and implementation. *A*: Simultaneous computed synaptic conductances arising from each of the premotor heart interneurons ($g_{HN(i)}$; colored traces) as well as the sum of these synaptic conductances (g_{Syn}; black trace) for both the peristaltic and synchronous coordination modes. g_{Syn} is the time varying conductance ($g_{Syn}(t)$, see Methods) introduced into the HE(10) motor neuron. The two g_{Syn} traces illustrate the difference between the peristaltic and synchronous input patterns. In the peristaltic mode, g_{Syn} rises and declines gradually, as the firing of the premotor inputs are spread out over time, while in the synchronous mode, g_{Syn} rises and falls rapidly, as the firing of the premotor inputs occurs at nearly the same time. *B*: Hybrid system setup. We recorded simultaneously from a pair of heart motor neurons ($V_{HE(L,i)}$ and $V_{HE(R,i)}$) from a given segment, and pharmacologically isolated the motor neurons from their premotor heart interneuron inputs ("X"; see Methods). The dynamic clamp computes and injects in real time the artificial equivalent of the appropriate synaptic current (I_{dc}) into the heart motor neurons. In some experiments, the dynamic clamp was also used to compute I_{coup}. *C*: Exemplar dynamic clamp experiment and calculation of phase. Simultaneous intracellular recordings from a pair of HE(10) motor neurons are shown. At the beginning of the voltage recording, the heart motor neurons were firing tonically; g_{Syn} is 0 nS. Once the dynamic clamp synapse was activated (vertical line), the dynamic clamp injects a time-varying current proportional to the synaptic conductance. In some figures, the dynamic clamp current (I_{dc}) is omitted, and only the synaptic conductance is shown. The vertical green lines on the traces

show the middle spike of the peristaltic HN(4) interneuron (0/1 – our phase reference) and of the synchronous HN(4) interneuron (0.5). The interval between the two green lines of our phase reference is the cycle period. The average phase for an individual experiment here and in subsequent figures is indicated next to a filled diamond.

Figure 2.2

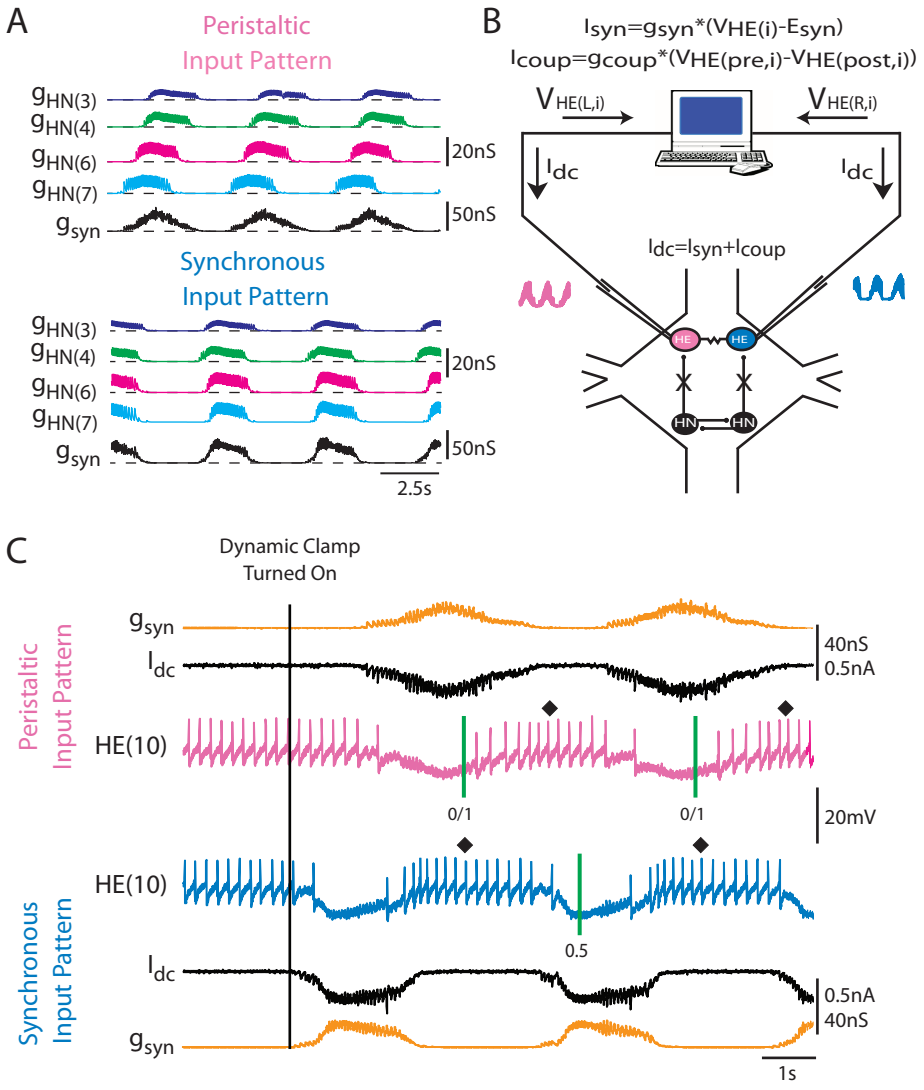
A
Peristaltic
Input Pattern
gHN(3)
gHN(4)
gHN(6)
gHN(7)
gsyn
20nS
50nS
Synchronous
Input Pattern
2.5s
B
Isyn=gsyn*(VHE(i)-Esyn)
Icoup=gcoup*(VHE(pre,i)-VHE(post,i))
VHE(L,i)
VHE(R,i)
Idc
Idc=Isyn+Icoup
HE
HN
C
Dynamic Clamp
Turned On
Peristaltic
Input Pattern
gsyn
Idc
40nS
0.5nA
HE(10)
0/1
0/1
20mV
Synchronous
Input Pattern
HE(10)
0.5
Idc
gsyn
0.5nA
40nS
1s

In some experiments, we used the dynamic clamp to add to the natural electrical coupling between heart motor neurons. Electrical coupling was implemented according to:

$$I_{coup} = g_{coup}(V_a - V_b)$$

where V_a and V_b each represent the membrane potentials of one member of the pair of coupled heart motor neurons, I_{coup} is the coupling current from cell b to cell a (and $-I_{coup}$ is the coupling current from cell a to b), and g_{coup} is the junctional conductance. Therefore, the total dynamic clamp current, I_{dc}, introduced to a pair of heart motor neurons (Fig. 2*B*) is defined as:

$$I_{dc} = I_{Syn} + I_{coup}$$

where, unless otherwise noted, I_{coup} = 0 nA (i.e., g_{coup} = 0 nS).

In another set of experiments, we varied the structure of the premotor synaptic conductance waveform in order to study how the coherence of the synaptic input pattern influences HE motor neuron phase. The temporal pattern of this synaptic input was based on the firing pattern of the HN(4) interneurons (both peristaltic and synchronous, each with their appropriate phasing) only; in this way, we could compute phase using the same phase reference as in our other experiments. The synaptic strength profile associated with this temporal pattern was the sum of the individual premotor heart interneuron synaptic conductances

(i.e, $g_{Syn} = \sum g_{SynHN(i)}$). The synaptic conductance waveform was trapezoidal in shape. The onset of the conductance envelope was triggered by the first spike of the HN(4) interneuron burst. The conductance envelope increased linearly from 0 nS to g_{Syn} during the first 500 ms of the HN(4) interneuron burst, remained constant at g_{Syn} before returning (termed "offset ramp conductance" in this study) to 0 nS either 1) abruptly at the last spike of the HN(4) interneuron burst, 2) during the last 250 ms of the HN(4) interneuron burst or 3) during the last 500 ms of the HN(4) interneuron burst. One heart motor neuron received this series of waveforms in order of increasing offset ramp conductance while its contralateral partner was receiving the same set of waveforms in order of decreasing offset ramp conductance.

In hybrid system experiments, we blocked the endogenous synaptic input with 10^{-4} M bicuculline methiodide unless otherwise noted. All dynamic clamp calculations were performed using a real-time dedicated processing board (DS1104, dSPACE, Detroit MI). We activated the dynamic clamp synapses and electrical coupling only when the motor neurons were spiking tonically and had no discernible inhibitory postsynaptic potentials in the voltage recording (Fig. 2*C*). In our hybrid system experiments, we either: 1) bilaterally varied the synaptic scaling factor (σ) introduced to a pair of heart motor neurons, 2) varied the origin of the segmental input pattern introduced into the same heart motor neuron pair, 3) varied the coupling conductance, g_{coup}, between heart motor neurons within a segment or 4) introduced modified synaptic conductance patterns to heart motor neurons (see above). In experiments 1-3, we introduced

thirteen cycles of inhibitory synaptic conductance into a heart motor neuron pair, yielding 12 bursts of activity over 60 s. In experiment 4, we introduced 10 cycles of inhibitory synaptic conductance over 45 s, yielding 9 bursts of heart motor neuron activity.

Data Analysis

Electrophysiological data were analyzed offline using a combination pCLAMP 9.2 (Molecular Devices) and custom scripts written in Matlab (The Mathworks, Natick, MA) and Spike2 (CED Systems, Cambridge, UK). First, the raw voltage recordings were high-pass filtered (cut-off frequency ~ 1 Hz). These data were then used for spike detection. Spike detection was carried out using methods reported previously (Norris et al., 2006).

After detection, spikes were grouped into bursts as follows: after an interburst interval of 500 ms or more, the next spike was deemed the first spike of that burst. Each subsequent spike was included in that burst until the interspike interval became greater than 500 ms (interburst interval). A minimum of four spikes were required in order to qualify as a burst. In some experiments, the dynamic clamp-mediated inhibitory synaptic current injected into a heart motor neuron did not inhibit it sufficiently, so that the heart motor neuron continued firing, but at a low frequency, during the inhibited phase of its

oscillations (i.e., during the peak dynamic clamp injected current). In those recordings, we removed this small number (usually < 4) of spikes during the trough of the inhibited phase to create a sufficient interburst interval for burst detection.

We define period as the interval between successive middle spikes of the peristaltic HN(4) interneuron ($T_{HN(4)}$). We then computed the phase of the heart motor neurons with respect to the synaptic input pattern that they received. We define phase as the difference in time for a spike of interest of a heart motor neuron and the time of the middle spike of the phase reference, the peristaltic HN(4) interneuron ($\Delta t_{HE(i)f,m,l-HN(4)}$). This difference is then normalized to the period of the phase reference Thus phase is given by:

$$\phi_{f,m,l} = (\Delta t_{HE(i)f,m,l-HN(4)}/T_{HN(4)})$$

We calculated the average first (f), middle (m) and last (l) spike phase, burst period (T) and duty cycle (D) for each heart motor neuron recorded. In the text and figures, the generic term phase and symbol ϕ are applied to the middle spike phase as defined above. In figures, we indicate the middle spike phase within each heart motor neuron burst by a filled diamond above that burst. All phase values are expressed modulo one. Duty cycle is defined as the difference between the average last spike phase and the average first spike phase:

$$D = \phi_{last} - \phi_{first}$$

Because the duty cycle is the difference between two averages, standard deviation is not reported.

Statistics

Data were compiled and analyzed using Microsoft Excel (2010, Microsoft, Redmond, WA), SigmaPlot 11 (Systat Software, San Jose, CA), Minitab (v14, Minitab, State college, PA) or Matlab (The Mathworks). We generated an average phase and duty cycle for each preparation, and the average ($\pm$ sd, n = either 6 or 7 preparations) across animals was used for all statistical analyses. In the experiments in which the synaptic conductance was scaled (by varying σ, see *Dynamic Clamp Implementation*), the coupling conductance (g_{coup}) was varied, or the synaptic conductance (g_{syn}) was modified, all phases and duty cycles were analyzed using a One-Way Repeated Measures ANOVA with follow up Bonferroni post-tests. For comparisons between the hybrid and living systems, we used a 2-sample *t*-test to compare the appropriate phases. For comparisons between either the living or hybrid system and the model, we used a 1-sample *t*-test. Finally, in experiments in which the segmental input pattern was varied, a 2-Way (Cell x Pattern) Repeated Measures ANOVA was used, with Bonferroni post-tests. Statistical significance was set at $p < 0.05$ for all statistical tests. All figures were generated using Adobe Illustrator 15.0 (Adobe Systems, San Jose, CA).

RESULTS

Scaling the synaptic input conductance by a constant factor affects hybrid system heart motor neuron duty cycles but not their phasing

In our previous modeling efforts (García et al. 2008), we hand-tuned the output of the model motor neurons by scaling the synaptic conductance waveform by a constant factor. This manipulation allowed us to match total synaptic conductance to the model neuron intrinsic properties while preserving the relative contribution of each of the premotor heart interneurons. Adjusting the scaling factor effectively tuned the duty cycle of the model motor neurons, without affecting their middle spike phasing. To determine the appropriate scaling factor for our experiments and to determine its effects on firing phase and duty cycle, we varied the scaling factor of the synaptic conductance in the hybrid system. We recorded simultaneously from the pair of heart motor neurons in segment 10 (n = 6) and played in the segmental input pattern for the HE(10) motor neurons from our canonical ensemble model. We then scaled this input by three different constant values: 3, 5 and 8 (σ, see Methods) (Fig 3*A-C*). We chose these values because values smaller than 3 resulted in bursts that were poorly defined at their beginning and ends, with duty cycles typically greater than 0.9, while values greater than 8 did not further decrease the duty cycle because at these scaling values the heart motor neurons were silenced for the duration of the

input waveform each cycle. We then compared the average first spike, middle spike and last spike phase, as well as the duty cycles observed among the three different scaling factors. Figure 3*D* shows summarized results for experiments performed in segments 8, 10, 12 and 14 as a bilateral phase diagram. There was a significant decrease in duty cycle with increasing scaling factor in all segments tested in the peristaltic mode and in segments 10, 12 and 14 in the synchronous mode (One-Way Repeated Measures ANOVA, $p < 0.05$). In those segments where there was a significant difference in duty cycle, there were also significant differences in the average first and last spike phase among the three scaling factors (One-Way Repeated Measures ANOVA, $p < 0.05$). As the scaling factor is increased, burst onsets (as measured by the average first spike phase) are delayed, while burst offsets (as measured by last spike phase) are advanced. The middle spike phase, therefore, is not affected because the scaling factor decreases the incidence of spikes nearly equally from both the beginning and the end of each heart motor neuron burst.

The middle spike phase, however, was significantly different across the three scaling factors in some of the segments tested, specifically, the HE(10) motor neuron receiving the peristaltic input pattern and the HE(10) and HE(12) motor neurons receiving the synchronous input pattern. To assess which of the scaling factors were different, we conducted Bonferroni post-tests. In each segment, the 8 scaling factor was significantly different from both the 3 and 5 scaling factors ($p < 0.05$); the 3 and 5 scaling factors were not significantly different from each other. Although there are significant differences in middle

FIG 2.3. Tuning the output of heart motor neurons using the synaptic scaling factor in the hybrid system. *A-C*: Simultaneous intracellular recordings from a pair of HE(10) motor neurons receiving the same HE(10) segmental input pattern as that used in our canonical ensemble model. Panels *A-C* are from the same experiment. The synaptic conductance was scaled by a constant value (σ; see Methods) of 3(*A*), 5(*B*) or 8(*C*). *D*: Bilateral phase diagram for HE motor neurons in segments 8, 10, 12 and 14 for each of the 3 scaling factors Filled symbols show the average (n = at least 6 preparations per segment) middle spike phase for segment 8 (circles), 10 (triangles), 12 (squares) and 14 (diamonds); vertical bars connected to the filled symbols show the average first (left vertical lines) and last (right vertical lines) spike phase. Lines and asterisks indicate significant differences in the appropriate phasing or duty cycle among the three scaling factors (1-Way Repeated Measures ANOVA, $p < 0.05$).

Figure 2.3

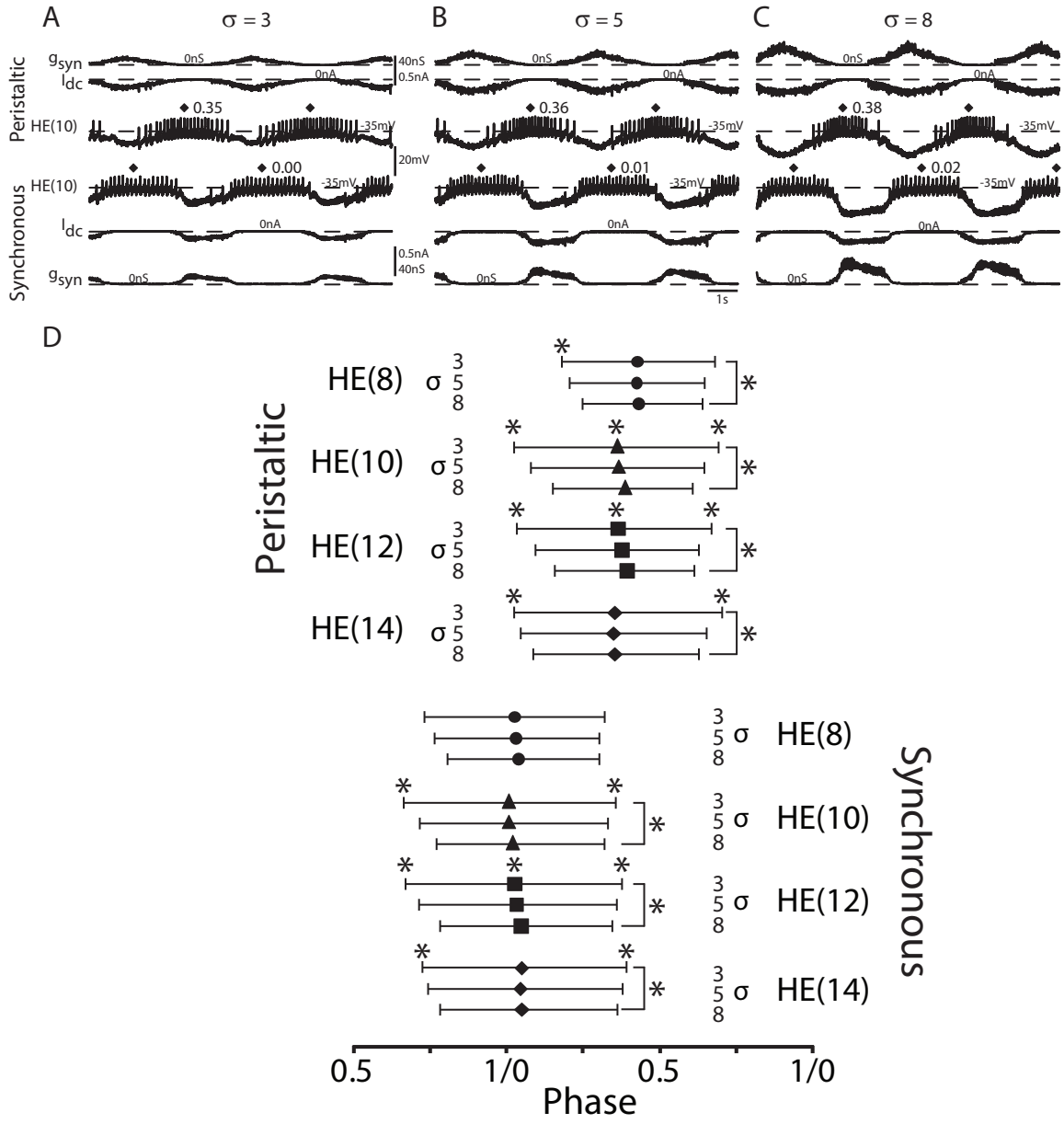
A
σ = 3
B
σ = 5
C
σ = 8
Peristaltic
Synchronous
gsyn
Idc
HE(10)
0nS
0nA
40nS
0.5nA
20mV
-35mV
0.35
0.36
0.38
0.00
0.01
0.02
1s
D
HE(8)
HE(10)
HE(12)
HE(14)
σ
3
5
8
Peristaltic
Synchronous
0.5
1/0
Phase

spike phase among the three scaling factors in our experiments, it is important to note that each of the values observed fall within the range of middle spike phase measured in the living system (Norris et al. 2007a). In subsequent experiments, however, we focused only on segments where the scaling factor did not show this effect (i.e., segments 8 and 14).

Taken together, these results suggest that, as in our canonical ensemble model (García et al. 2008), scaling the synaptic conductance waveform by a constant factor over a moderate range allowed us to tune the output of the heart motor neurons without affecting the middle spike phase. We settled on the scaling factor of 3 for comparison of hybrid system phasing to living system phasing, because the duty cycle associated with this scaling factor was the most similar to that observed in the living system (Table 1).

The segmental input pattern determines segmental phase differences in motor neuron phasing in the hybrid system

Before assessing whether heart motor neuron intrinsic properties contribute to their appropriate segmental phasing, we asked whether the intrinsic properties of the motor neurons were similar across segments. Because the canonical ensemble model motor neurons are identical in their intrinsic properties, they naturally assume different output phasing depending on the

segmental input pattern introduced into them. To test whether heart motor neurons in mid-body segments 8 through 14 show any systematic variation in their intrinsic properties, we isolated segmental ganglia 8 and 14 (n = 6 each) in each experiment and synaptic strength profiles for segments 8 and 14 were introduced into the heart motor neuron in both ganglia. Figure 4*A* compares the response of the HE(8) motor neurons to the HE(8) and the HE(14) synaptic strength profiles; Figure 4*B* compares the response of the HE(14) motor neurons to the HE(8) and the HE(14) synaptic strength profiles. Figure 4*C* shows the average ($\pm$ sd) phase of the HE(8) motor neuron (left panel) and HE(14) motor neuron (right panel) phase when receiving both synaptic strength profiles. The lines connecting the phase symbols show the effect of the synaptic strength profile on phase. There was a significant effect of the synaptic strength profile on phase in both coordination modes (2-Way Repeated Measures ANOVA; Peristaltic Mode $F = 410.87$, $df = 1$, $p < 0.01$; Synchronous Mode $F = 147.47$, $df = 1$, $p < 0.01$). Comparing the average phase of the HE(8) and HE(14) motor neurons when receiving the same synaptic strength profile (e.g., compare the HE(8) and the HE(14) motor neuron phase when both receive the HE(8) synaptic strength profile in Figure 4*C*) indicates the effect of the segmental origin of the heart motor neuron on phase. There was no significant effect of the segmental origin of the heart motor neuron on phase in either mode (2-Way Repeated Measures ANOVA; Peristaltic Mode $F = 0.04$, $df = 1$, $p = 0.85$; Synchronous Mode $F = 0.41$, $df = 1$, $p = 0.55$). These results suggest that there are no systematic differences in heart motor neuron intrinsic properties between midbody segments 8 and 14 that cause them to respond differently to similar

FIG 2.4. Heart motor neurons respond differently to different synaptic strength profiles. *A*: Simultaneous intracellular recordings from a pair of HE(8) motor neurons receiving the segment 8 (left panel) followed by the segment 14 (right panel) input patterns. Both panels are from the same experiment. The synaptic strength profiles are different between the two segmental patterns (note the different scale bars). *B*: Same as panel A, but for the HE(14) motor neurons. Both preparations came from the same animal. *C*: The average phase ($\pm$ sd, n = 6) of heart motor neurons in segments 8 (left panel) and 14 (right panel) each receiving the synaptic strength profiles for segments 8 and 14 are shown. Asterisks on each dashed line connecting data points indicate a significant effect of synaptic strength profile on motor neuron phase (2-Way Repeated Measures ANOVA, $p < 0.05$).

Figure 2.4

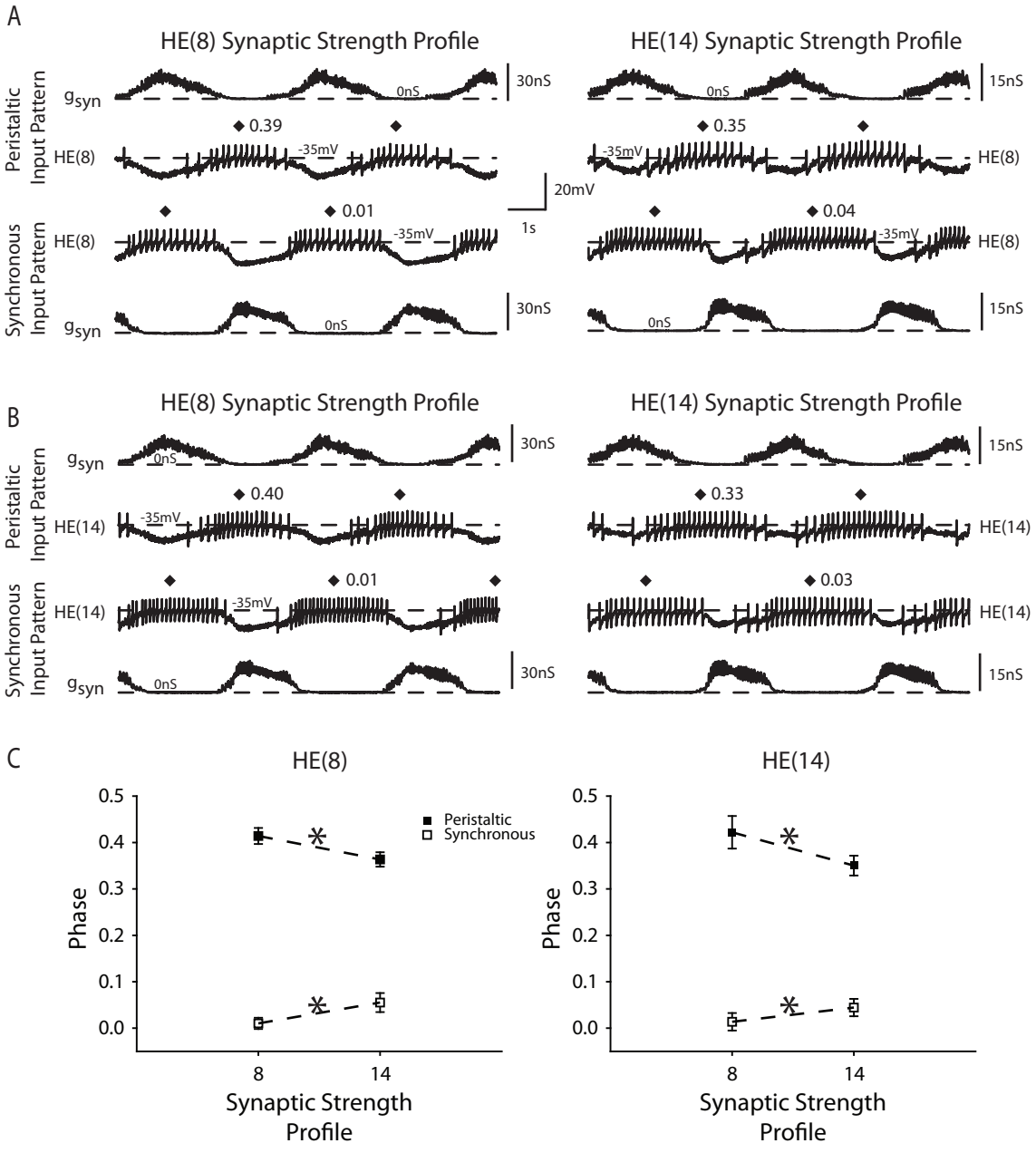
A
HE(8) Synaptic Strength Profile
HE(14) Synaptic Strength Profile
Peristaltic Input Pattern
Synchronous Input Pattern
g_syn
HE(8)
HE(14)
0nS
30nS
15nS
0.39
0.35
0.01
0.04
-35mV
20mV
1s
B
HE(8) Synaptic Strength Profile
HE(14) Synaptic Strength Profile
0.40
0.33
0.01
0.03
C
HE(8)
HE(14)
Peristaltic
Synchronous
Phase
0.0
0.1
0.2
0.3
0.4
0.5
8
14
Synaptic Strength Profile

input patterns. In addition, they suggest that the segmental input pattern independently determines the phasing differences observed in motor neurons in segments 8 through 14, regardless of any role heart motor neuron intrinsic properties may play in the final phasing assumed.

Comparison of motor neuron phasing in the hybrid and living system

We now compared the phasing of heart motor neurons in the hybrid system to the phasing observed in the living system and the model. Figure 5, panels *A*-*D*, show typical recordings from heart motor neurons from segments 8 (Fig. 5*A*), 10 (Fig. 5*B*), 12 (Fig. 5*C*) and 14 (Fig. 5*D*) (n = at least 6 per segment). Each of these motor neurons received the same segment appropriate input pattern as those in our canonical ensemble model. Figure 5*E* shows a bilateral phase diagram for the summarized data for each of these segments. Asterisks in Figure 5*E* show comparisons of the hybrid system to the living system and pound signs show comparisons of the canonical ensemble model to the living system; Table 1 includes all possible comparisons. We present the segment-specific results for the peristaltic mode first, followed by the synchronous mode.

In the hybrid system for HE(8) motor neurons receiving the peristaltic input pattern, first spike phase was similar to that observed in the living system (2-sample *t*-test, $p = 0.41$), but their middle and last spike phases were delayed

(2-sample *t*-test, $p < 0.05$ for both comparisons) (Fig. 5*E*). When comparing canonical ensemble model phasing to the living system, model first spike phase was delayed and middle and last spike phases were advanced (1-sample *t*-test, $p < 0.05$ for all comparisons) (Fig. 5*E*). When compared to the canonical ensemble model, the hybrid system first spike phase was advanced (1-sample *t*-test, $p < 0.05$), but middle and last spike phases were similar (1-sample *t*-test, middle spike $p = 0.50$; last spike $p = 0.27$) (Table 1). Considering middle spike phase only, HE(8) bursts in both the model and the hybrid system are phase advanced compared to the living system.

In the hybrid system for HE(10) motor neurons receiving the peristaltic input pattern, first middle and last spike phases were similar to that observed in the living system (2-sample *t*-test, first $p = 0.86$, middle $p = 0.69$, last spike $p = .66$) (Fig. 5*E*). When comparing canonical ensemble model phasing to the living system, model first spike phase was delayed (1-sample *t*-test, $p < 0.05$), middle was similar (1-sample *t*-test, $p = 0.67$), and last spike phase was advanced (1-sample *t*-test, $p < 0.05$) (Fig. 5*E*). When compared to the canonical ensemble model, the hybrid system first spike phase was advanced (1-sample *t*-test, $p < 0.05$), middle spike phase was similar (1-sample *t*-test, $p = 0.11$), and last spike phase was delayed (1-sample *t*-test, $p < 0.05$) (Table 1). Considering middle spike phase only, HE(10) bursts in both the model and the hybrid system are phased similarly to the living system.

In the hybrid system for HE(12) motor neurons receiving the peristaltic input pattern, first middle and last spike phases were similar to that observed in the living system (2-sample *t*-test, first p = 0.61, middle p = 0.54, last p = 0.55) (Fig. 5*E*). When comparing canonical ensemble model phasing to the living system, model first spike and middle phases were similar (1-sample *t*-test, first spike p = 0.06, middle spike p = 0.67), and last spike phase was advanced (1-sample *t*-test, $p < 0.05$) (Fig. 5*E*). When compared to the canonical ensemble model, the hybrid system first spike phase was advanced (1-sample *t*-test, $p < 0.05$), middle spike phase was similar (1-sample *t*-test, p = 0.57), and last spike phase was delayed (1-sample *t*-test, $p < 0.05$) (Table 1). Considering middle spike phase only, HE(12) bursts both the in the model and in the hybrid system are phased similarly to the living system.

In the hybrid system for HE(14) motor neurons receiving the peristaltic input pattern, first and middle spike phase tend to be delayed compared to that observed in the living system though this delay is not statistically significant (2-sample *t*-test, first p = 0.11, middle spike p = 0.06, last spike p = 0.67) (Fig. 5*E*). When comparing canonical ensemble model phasing to the living system, model first and middle spike phases were delayed (1-sample *t*-test, $p < 0.05$ for both comparisons), whereas last spike phase was similar (1-sample *t*-test, p = 0.97) (Fig. 5*E*). When compared to the canonical ensemble model, the hybrid system first, middle and last spike phases were similar (1-sample *t*-test, first p = 0.12, middle spike p = 0.99, last spike p = 0.77) (Table 1). Considering middle spike

Table 2.1. Statistical comparison of phasing observed in the living system, hybrid system and ensemble model for heart motor neurons in segments 8, 10, 12 and 14.

Table 2.1

Segment		Peristaltic Coordination Mode							Synchronous Coordination Mode					
		First Spike	SD	Middle Spike	SD	Last Spike	SD		First Spike	SD	Middle Spike	SD	Last Spike	SD
8	Living	0.20	0.07	0.47	0.04	0.77	0.07	Living	0.73	0.06	0.01	0.04	0.32	0.05
	Hybrid	0.18‡	0.03	0.43*	0.02	0.68*	0.05	Hybrid	0.73	0.04	0.02‡	0.04	0.32	0.04
	Model	0.26#	0.01	0.43#	0.02	0.67#	0.04	Model	0.82#	0.04	0.12#	0.03	0.35#	0.04
10	Living	0.03	0.09	0.37	0.07	0.71	0.08	Living	0.70	0.10	0.02	0.07	0.36	0.05
	Hybrid	0.02‡	0.02	0.36	0.02	0.69‡	0.04	Hybrid	0.66‡	0.04	0.01‡	0.03	0.36‡	0.04
	Model	0.16#	0.03	0.38	0.01	0.62#	0.01	Model	0.83#	0.04	0.15#	0.03	0.39#	0.03
12	Living	0.05	0.08	0.35	0.05	0.69	0.07	Living	0.73	0.13	0.03	0.08	0.35	0.07
	Hybrid	0.04‡	0.02	0.36	0.02	0.67‡	0.04	Hybrid	0.67‡	0.04	0.03‡	0.03	0.38‡	0.04
	Model	0.10	0.02	0.36	0.01	0.63#	0.04	Model	0.83#	0.04	0.15#	0.03	0.41#	0.04
14	Living	0.94	0.11	0.27	0.10	0.69	0.10	Living	0.73	0.13	0.04	0.10	0.44	0.09
	Hybrid	0.02	0.03	0.35	0.02	0.70	0.04	Hybrid	0.72‡	0.05	0.05‡	0.03	0.39‡	0.04
	Model	0.07#	0.02	0.36#	0.02	0.71	0.04	Model	0.82	0.04	0.16#	0.03	0.43	0.04

* represents significant differences between hybrid and living system (2-sample *t*-test). ‡ represents significant differences between hybrid system and model (1-sample *t*-test). # represents significant differences between the model and the living system (1-sample *t*-test). See Methods

phase only, HE(14) bursts in the hybrid system are phased similarly but in the model they are delayed compared to the living system.

In the hybrid system for HE(8), HE(10), HE(12) and HE(14) motor neurons receiving the synchronous input pattern, the results were similar, so we treat them together. In each of these motor neurons, the hybrid system first, middle and last spike phases were similar to the living system (2-sample *t*-test, $p >> 0.05$ for all comparisons) (Fig. 5*E*). When comparing canonical ensemble model phasing to the living system, in the HE(8) motor neuron first and middle spike phases were delayed (1-sample *t*-test, $p < 0.05$ for both comparisons) and last spike phase was similar (1-sample *t*-test, $p = 0.14$) (Fig. 5*E*). In the HE(10) and HE(12) motor neurons first, middle and last spike phases were delayed (1-sample *t*-test, $p < 0.05$ for all comparisons) (Fig. 5*E*). In the HE(14) motor neuron only the middle spike phase was delayed (1-sample *t*-test, $p < 0.05$); the first and last spike phases were similar (1-sample *t*-test, first spike $p = 0.06$, last spike $p = 0.95$) (Fig. 5*E*). When compared to the canonical ensemble model, the hybrid system first, middle and last spike phases were all advanced (1-sample *t*-test, $p > 0.05$ for all comparisons) (Table 1). Considering middle spike phase only for all these motor neurons, bursts in the hybrid system are phased similarly but bursts in the model are delayed compared to the living system.

Because the motor neurons in the hybrid system received the same segmental input pattern as the model motor neurons, we infer that any differences in phasing (first, middle or last spike phase) between the hybrid

FIG 2.5. Heart motor neuron intrinsic properties contribute to their segment-appropriate phasing in the hybrid system. *A*-*D*: Simultaneous intracellular recordings and synaptic input conductances from heart motor neurons in segments 8(*A*), 10(*B*), 12(*C*) and 14(*D*). *E*: Bilateral phase diagram of the average first, middle and last spike phases measured in the living system (n = at least 8 preparations per segment; open squares), hybrid system (n = at least 6 preparations per segment; open triangles) and the canonical ensemble model (filled diamonds) for segments 8, 10, 12 and 14. *'s indicate a significant difference between the hybrid and the living system and #'s indicate a significant difference between the ensemble model and the living system (*t*-test, $p < 0.05$). Statistical comparisons between the hybrid system and the canonical ensemble model can be seen in Table 1.

Figure 2.5

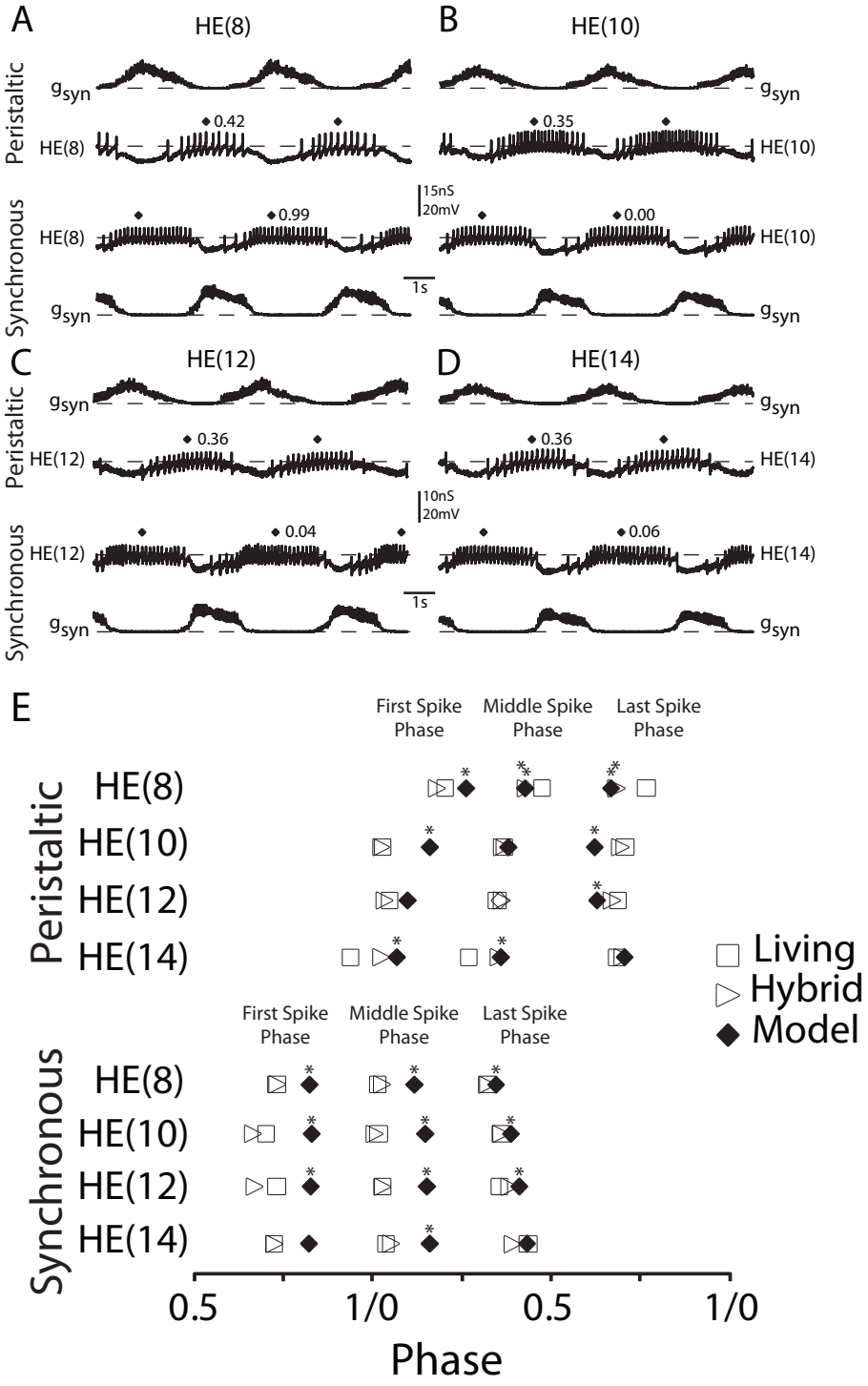
A
HE(8)
B
HE(10)
Peristaltic
g_{syn}
0.42
0.35
HE(8)
HE(10)
15nS
20mV
Synchronous
0.99
0.00
1s
C
HE(12)
D
HE(14)
0.36
0.36
10nS
20mV
0.04
0.06
E
First Spike Phase
Middle Spike Phase
Last Spike Phase
HE(8)
HE(10)
HE(12)
HE(14)
Living
Hybrid
Model
0.5
1/0
0.5
1/0
Phase

system and the canonical ensemble model indicate that the motor neurons in the living system possess additional intrinsic properties, not present in the model motor neurons. Similarity in the phasing of the motor neurons in the hybrid and living systems further corroborates this inference and further suggests that these additional intrinsic properties contribute to appropriate motor neuron phasing in the living system. Heart motor neurons in the hybrid system receiving the synchronous segmental input pattern, showed phasing similar to that observed in the living system and different from the model. We conclude that living motor neurons possess intrinsic properties that contribute to proper phasing when receiving the synchronous input. When receiving peristaltic input in the hybrid system, in those cases (i.e., HE(10) and HE(12) motor neurons) where ensemble model phasing is similar to the living system, the hybrid system also showed phasing similar to the living system. However, the HE(8) motor neurons in the hybrid system like their model counterparts are phase advanced compared to the living system, and the HE(14) motor neurons in the hybrid system show a tendency to be phase delayed compared to the living system, though this delay is not statistically significant, as this delay is in their model counterparts.

To assess whether the discrepancies observed between the hybrid system and the living system phasing (in the peristaltic mode) were due to non-specific effects of the bicuculline methiodide block of the premotor inputs, we performed experiments in which we blocked the premotor inputs with a modified leech saline in which the Ca^{2+} was replaced with an equimolar amount of Mn^{2+}. In these experiments, the HE(8) motor neurons received the HE(8) segmental input

pattern during exposure to this modified saline. We then compared the phasing observed with the modified saline to that observed in bicuculline methiodide. Although the average (n = 6) middle spike phase was delayed in both the peristaltic (0.01) and synchronous mode (0.02) when compared to the bicuculline methiodide block, there was not a significant difference in middle spike phase between the two forms of presynaptic block (2-sample *t*-test; data not shown). Furthermore, the delay in phase did not change the correspondence between the hybrid system and the living system in either mode. This result indicates that bicuculline methiodide did not strongly affect the phasing observed in the hybrid system.

Heart motor neurons in the hybrid system receiving the synchronous segmental input pattern, however, show phasing consistent with that observed in the living system.

Contribution of heart motor neuron intrinsic properties to phasing observed in the hybrid system

Next, we explored how the intrinsic properties of the heart motor neurons in the living system may allow them to integrate a segmental input pattern differently from the model motor neurons in the canonical ensemble model. In the canonical ensemble model, the current primarily responsible for

depolarization and burst formation is a persistent Na^+ current, which was characterized by Opdyke and Calabrese (1994) in heart interneurons and termed I_P. The I_P current in the model was hand-tuned so the model motor neurons fired tonically at an appropriate spike frequency in the absence of synaptic input (Schmidt and Calabrese 1992). The model motor neurons did not include currents such as I_h, which could produce post-inhibitory rebound in response to the synaptic input pattern they received. The synchronous premotor synaptic conductance declines precipitously due to near synchrony in the termination of the premotor inputs. Therefore, model motor neurons receiving the synchronous input pattern are only able to initiate their bursts once the synaptic conductance has nearly ended. When a model motor neuron initiates its firing, its spike frequency increases throughout a burst. Heart motor neuron pairs share inhibitory synaptic current via their electrical coupling. As inhibition in the opposite motor neuron wanes, spike frequency in uninhibited motor neuron increases due to less shared inhibitory current. This sharing of inhibitory current delays the depolarization of a model motor neuron during its burst (cf Fig. 5, (García et al. 2008)). Therefore, the lack of postinhibitory rebound, combined with the delaying effect of the electrical coupling, contribute to a delay in model phase when compared to the living system in the synchronous mode. In the hybrid system, heart motor neurons receiving the synchronous input pattern show modest rebound spiking and, on average, initiate their firing at an earlier phase than model motor neurons (Fig. 5). Although there were some significant differences in last spike phase between the model and the hybrid system in the synchronous mode (Table 1), these differences were not as substantial as those

observed in the first and middle spike phase, so we focused on the role of intrinsic properties in the initiation of firing rather than on the termination of firing. We hypothesized that heart motor neurons, owing to their intrinsic properties, are able to initiate their bursts earlier in the hybrid system than the motor neurons in the canonical ensemble model. Therefore, motor neurons in the hybrid system are able to match the phasing observed in the living system unlike the model motor neurons.

Opdyke and Calabrese (1995) characterized multiple outward currents in the heart motor neurons. The inward currents they found were small when measured at the level of the heart motor neuron soma and hence not analyzed. Therefore, it was not feasible to test, via pharmacological blockade, which inward currents might account for the difference in synaptic input integration between the model and living heart motor neurons. As a compromise, we tested our hypothesis that heart motor neurons initiate their firing earlier by replacing the g_{Syn} extracted from the canonical ensemble model simulations with modified inhibitory synaptic conductance waveforms (Fig. 6). These modified waveforms were designed to engage the complement of intrinsic properties present in the heart motor neurons in different ways. The waveforms were timed to the inputs from the HN(4) premotor interneuron (to preserve our absolute phase reference) and were trapezoidal in shape. The modified conductance waveforms had the same onset kinetics (a ramp conductance rising from 0 nS to g_{syn}over 500 ms), but varied in their offset-kinetics, (i.e., the offset ramp conductance) returning from g_{syn} to 0 nS either 1) instantaneously (offset ramp conductance =

Instantaneous), 2) over the last 250 ms of the HN(4) interneuron burst (offset ramp conductance = 80 nS/s) or 3) over the last 500 ms of the HN(4) interneuron burst (offset ramp conductance = 40 nS). To determine how these waveforms were integrated by the heart motor neurons, we performed bilateral recordings of heart motor neurons in segment 8. One of the HE(8) motor neurons received three waveforms in which the offset ramp conductance increased from 40 nS/s to the instantaneous offset (Increasing Offset Ramp; Fig. 6, top row) while the other HE(8) motor neuron received the reverse sequence (Decreasing Offset Ramp, bottom row). We then compared the average (n = 7) first, middle and last spike phase among the three waveforms. There was a significant difference in the first and middle spike phase among the three inhibitory synaptic conductance waveforms (Fig. 6*D*; 1-Way Repeated Measures ANOVA, $p < 0.05$), with heart motor neurons receiving the instantaneous offset ramp conductance waveform firing later in phase than the 40 nS/s ramp offset waveforms. As expected, there was not a significant difference in last spike phase, as the conductance waveform onset ramp was the same for each of the trapezoidal waveforms used (1-Way Repeated Measures ANOVA, $p > 0.05$). The waveform with the instantaneous offset should most closely replicate the situation observed in the canonical ensemble model; by leaving g_{Syn} at its maximal value until the end of the HN(4) interneuron burst, this waveform overrides the expression of those heart motor neuron intrinsic properties that would initiate firing at an earlier phase. In contrast, the waveform with the slowest offset ramp allows the heart motor neurons to initiate their firing earlier in phase owing to their intrinsic properties. Interestingly, the phasing observed in

FIG 2.6. Replacing the standard synaptic conductance waveform with a modified conductance waveform affects heart motor neuron phase. Simultaneous intracellular recordings from the HE(8) motor neurons receiving a trapezoidal conductance waveform in which the offset rate increased from 40 nS/s (top row, *A*) to 80 nS/s (*B*) to instantaneously (*C*), while the other heart motor neuron received a trapezoidal conductance waveform in which the offset rate decreased from instantaneous (Bottom Row, *A*) to 80 nS/s (*B*) to 40 nS/s (*C*). Because we played in the series of waveforms to the two heart motor neurons in opposite directions, panel *A* and *C* correspond. All panels are from the same experiment. *D*: Summary phasing of the HE(8) motor neurons receiving the series of modified waveforms described in *A-C*. Asterisks on each line indicate significant differences in phase among the three waveforms (1-Way Repeated Measures ANOVA, $p < 0.05$).

Figure 2.6

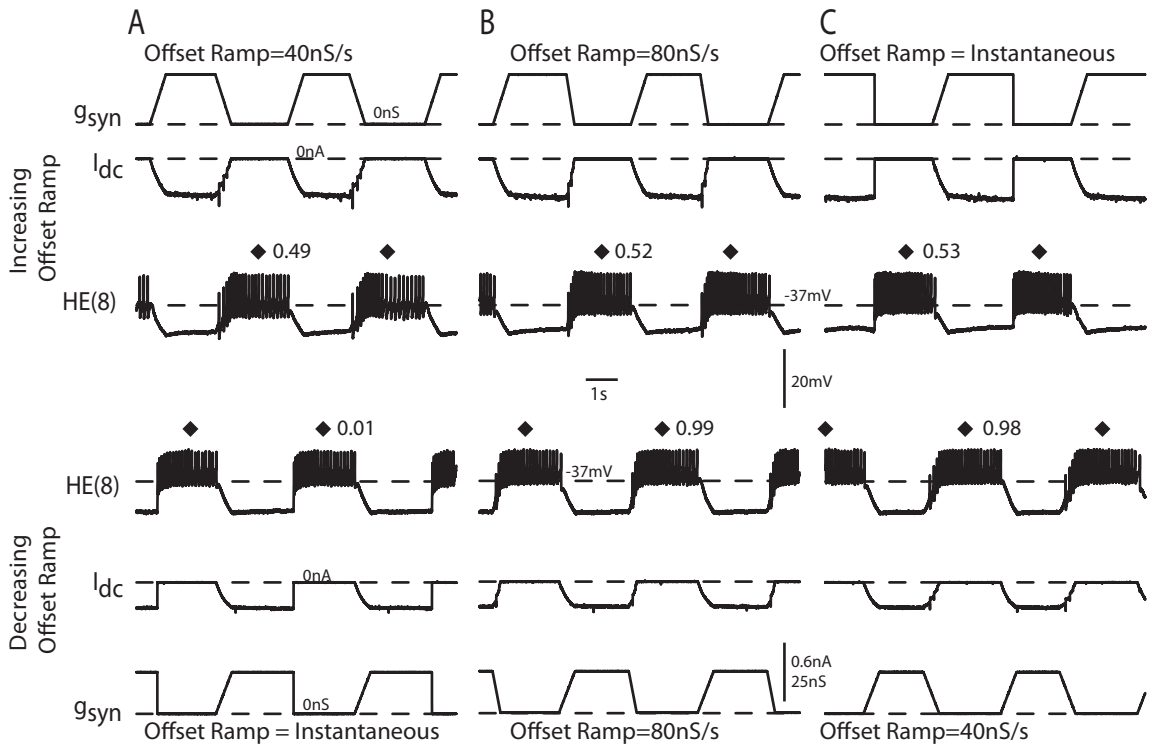
A
Offset Ramp=40nS/s
B
Offset Ramp=80nS/s
C
Offset Ramp = Instantaneous
gsyn
0nS
Idc
0nA
Increasing Offset Ramp
0.49
0.52
0.53
HE(8)
-37mV
1s
20mV
0.01
0.99
0.98
HE(8)
-37mV
Decreasing Offset Ramp
Idc
0nA
0.6nA
25nS
gsyn
0nS
Offset Ramp = Instantaneous
Offset Ramp=80nS/s
Offset Ramp=40nS/s

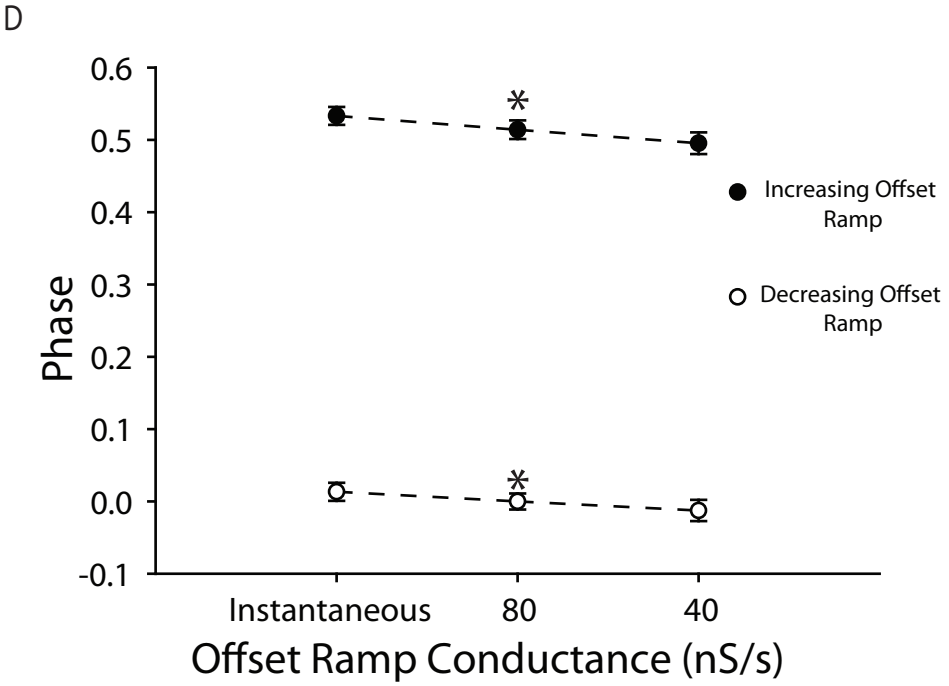
D
0.6
0.5
0.4
0.3
0.2
0.1
0.0
-0.1
Phase
Increasing Offset Ramp
Decreasing Offset Ramp
Instantaneous
80
40
Offset Ramp Conductance (nS/s)

the top row of panel A of Figure 6 would be well matched to the peristaltic mode phasing while the bottom row of panel A would be well matched the synchronous mode phasing observed in the living system (Norris et al. 2007b) suggesting that these two waveforms correspond roughly to our “peristaltic” and “synchronous” coordination mode segmental input patterns. That the hybrid system phasing with the “peristaltic” waveform results in a better match to the living system than the biologically derived peristaltic input waveform could be due to the fact that this waveform provides a greater amount of overall inhibition to the heart motor neurons and thus forces the heart motor neurons to assume a nearly antiphase (i.e., 0.5) output when compared to the HN(4) interneuron. Alternatively, these waveforms may access heart motor neuron intrinsic properties in a manner not replicated completely by the dynamics of the biological segmental input pattern. Taken together, these results suggest that heart motor neuron intrinsic properties contribute to their appropriate phasing, particularly when receiving the synchronous input pattern, by promoting phase advances.

Adding and subtracting electrical coupling alters the middle spike phasing of the heart motor neurons in the hybrid system

In addition to their intrinsic properties, another potential contribution to the phasing of heart motor neurons observed in the living system is the electrical coupling between segmental pairs (Peterson 1983). Our canonical ensemble

model (García et al. 2008) suggested that this coupling may be important in establishing motor neuron phasing. We wanted to explore, then, the extent to which electrical coupling could modify the phasing of motor neurons observed in the hybrid system and whether or not this influenced the difference in phase between the hybrid system and living system in the peristaltic mode. We explored the effect of electrical coupling in the hybrid system by adding virtual electrical coupling between the pair of heart motor neurons in segment 8.

First, we assessed the efficacy of virtual electrical coupling achieved with the dynamic clamp. We measured the endogenous level of soma-to-soma coupling present in pairs of HE(8) motor neurons with hyperpolarizing current pulses (Fig. 7*A*) and then computed the coupling coefficient (Fig. 7*B*) as the ratio of the post-synaptic voltage response to the pre-synaptic voltage response (n = 7). We then turned on the virtual electrical coupling with the synaptic conductance (g_{syn}) set to 0 nS and varied the virtual coupling conductance (g_{coup}) from 1.5 nS to 6 nS in 1.5 nS increments (Fig. 7*A*), computing the coupling coefficient for each value of g_{coup}. As can be seen in the average data of Figure 7*B*, there was a linear increase in the coupling coefficient as the virtual coupling conductance was increased. Greater than 99% of the variance in coupling coefficient is explained by its regression on the artificial coupling conductance applied ($R^2 = 0.996$, $F = 385.90$, $df = 1$, $p < 0.05$). This control protocol indicates that our virtual electrical coupling was effective and did not negatively affect the performance of the dynamic clamp.

FIG 2.7. Artificial electrical coupling alters middle spike phase in the hybrid system. *A*: Augmentation of endogenous gap coupling. Simultaneous intracellular recordings from a pair of HE(8) motor neurons. The dynamic clamp was running, but the dynamic clamp inhibitory synaptic input had been turned off (g_{Syn} = 0 nS). A -0.5 nA step of current (I_{inj}) was injected into one heart motor neuron (Injected Cell, Top Traces), and the voltage deflection in both neurons was recorded; the dynamic-clamp coupling conductance (g_{coup}) was set to 0 nS (left panel) or +6 nS (right panel). With no dynamic-clamp conductance, the contralateral heart motor neuron shows a voltage deflection (Coupled Neuron, Bottom Traces) indicative of the endogenous coupling present between the two heart motor neurons. With the dynamic-clamp coupling conductance set to +6 nS, the same current injection now produces a much larger voltage deflection in the coupled cell. We then computed the coupling coefficient as the ratio of the contralateral cells voltage deflection to the injected cells voltage deflection for a range of dynamic-clamp coupling conductances. *B*: Effect of artificial coupling on coupling coefficient. In seven experiments of the type described in panel *A*, we computed the coupling coefficient across a range of artificial coupling conductances in the dynamic clamp. The average ($\pm$ sd) coupling coefficient is plotted verses the artificial coupling conductance used in the dynamic clamp.

Figure 2.7

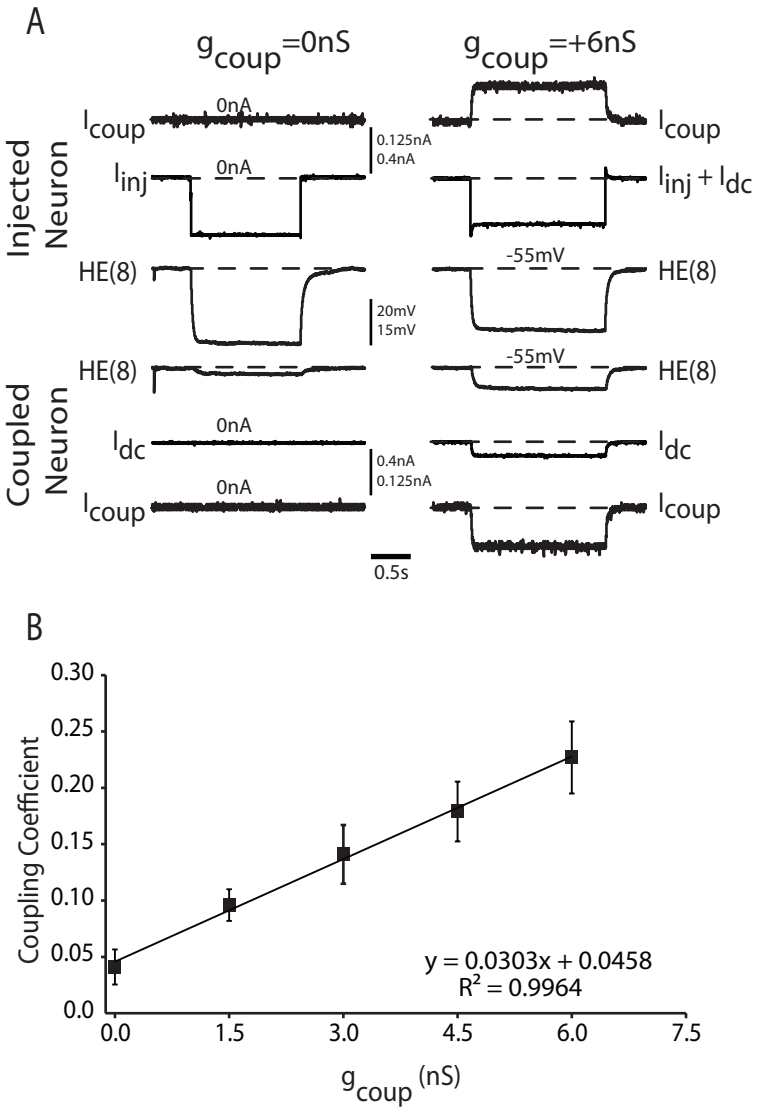
A
g_{coup}=0nS
g_{coup}=+6nS
Injected Neuron
Coupled Neuron
I_{coup}
I_{inj}
$I_{inj} + I_{dc}$
I_{dc}
HE(8)
0nA
0.125nA
0.4nA
20mV
15mV
-55mV
0.5s
B
Coupling Coefficient
g_{coup} (nS)
y = 0.0303x + 0.0458
R^2 = 0.9964
0.0
0.05
0.10
0.15
0.20
0.25
0.30
1.5
3.0
4.5
6.0
7.5

After performing the above control protocol, we then turned on the dynamic clamp synapse (in the same preparation) and played in the segment-appropriate peristaltic and synchronous inhibitory synaptic conductance waveforms along with the virtual coupling conductance set to either 6 nS, (Fig. 8*A*), 0 nS (Fig. 8*B*) and -6 nS (8*C*). When the virtual coupling conductance in this preparation was set to 6 nS, the phasing of the peristaltic heart motor neuron is shifted to an earlier phase (0.37 from 0.39) while the phasing of the synchronous motor neuron is shifted to a later phase (0.03 from 0.01) when compared to g_{coup} = 0 nS. In the average (n = 6) data, we saw significant differences in both coordination modes for phase (Fig. 8*D*; 1-Way Repeated Measures ANOVA, $p < 0.05$).

In the hybrid system experiments described above, we tested the removal of electrical coupling by setting the virtual coupling conductance to -6 nS. In the preparation illustrated in Figure 8*C*, the phase of the peristaltic heart motor neuron is shifted to a later phase (0.42 from 0.39) while the phasing of the synchronous motor neuron is shifted to an earlier phase (0.98 from 0.01) when compared to g_{coup} = 0 nS. There is a significant difference in the average (n = 7) phase in both coordination modes (1-Way Repeated Measures ANOVA, $p < 0.05$).

Increasing electrical coupling in the ensemble model (García et al. 2008) produces a synchronizing effect on the activity of the heart motor neurons (i.e., the side-to-side phase difference within a segment decreased). Here we explored the physiological significance of the electrical coupling between the heart motor

neurons in the hybrid system. In the case of adding to the endogenous coupling between heart motor neurons, when one heart motor neuron is hyperpolarized because of the inhibitory input pattern, that motor neuron passes hyperpolarizing current to its contralateral homolog (arrow on upper I_{coup} trace, Fig. 8*A*); at the same time, the contralateral motor neuron, which is spiking, passes depolarizing current back to the hyperpolarized cell (arrow on lower I_{coup} trace, Fig. 8*A*).The net effect of enhancing endogenous electrical coupling is two-fold; the first is to decrease the impact of a given heart motor neurons I_{Syn} because some portion of that motor neurons synaptic current is passed to its contralateral homolog via the electrical coupling. Secondly, hyperpolarizing current passing from an inhibited motor neuron to its contralateral homolog during its spiking phase attenuates spiking activity during its burst. In the peristaltic mode, these two effects combine to promote a phase advance, as passage of hyperpolarizing current to the peristaltic motor neuron from its inhibited contralateral homolog slows its burst; shifting a greater incidence of spikes to the beginning of the burst. In the synchronous mode, these two effects promote a phase delay, as passage of hyperpolarizing current attenuates the onset of the burst. These two effects result in a significantly smaller within segment phase difference when compared to g_{coup} = 0 nS (Fig. 8*E*; 1-Way Repeated Measures ANOVA, $p < 0.05$), suggesting that electrical coupling synchronizes (i.e., brings their phasing closer together) activity between heart motor neurons within a segment. In our ensemble model, García et al. (2008) suggested that this synchronizing effect was not uniform across segments due to the side-to-side differences in the phasing of the input

FIG 2.8 Effect of artificial coupling on HE(8) motor neuron phase. Simultaneous intracellular recordings from the HE(8) motor neurons with the artificial coupling conductance g_{coup} set to -6 nS (*A*) , 0 nS (*B*) and +6 nS (*C*). Each panel is from the same experiment. *D*: Summary phase (average $\pm$ sd, n = 6) for the HE(8) motor neurons receiving the coupling conductances as described in *A-C*. Asterisks on each line indicate a significant difference in phase among the 3 artificial coupling values (1-Way Repeated Measures ANOVA, $p < 0.05$). E. Summary (average $\pm$ sd, n = 6) within-segment phase difference between the two HE(8) motor neurons. Asterisks indicate a significant difference in the within-segment phase difference across the three artificial coupling values (1-Way Repeated Measures ANOVA, $p < 0.05$).

Figure 2.8

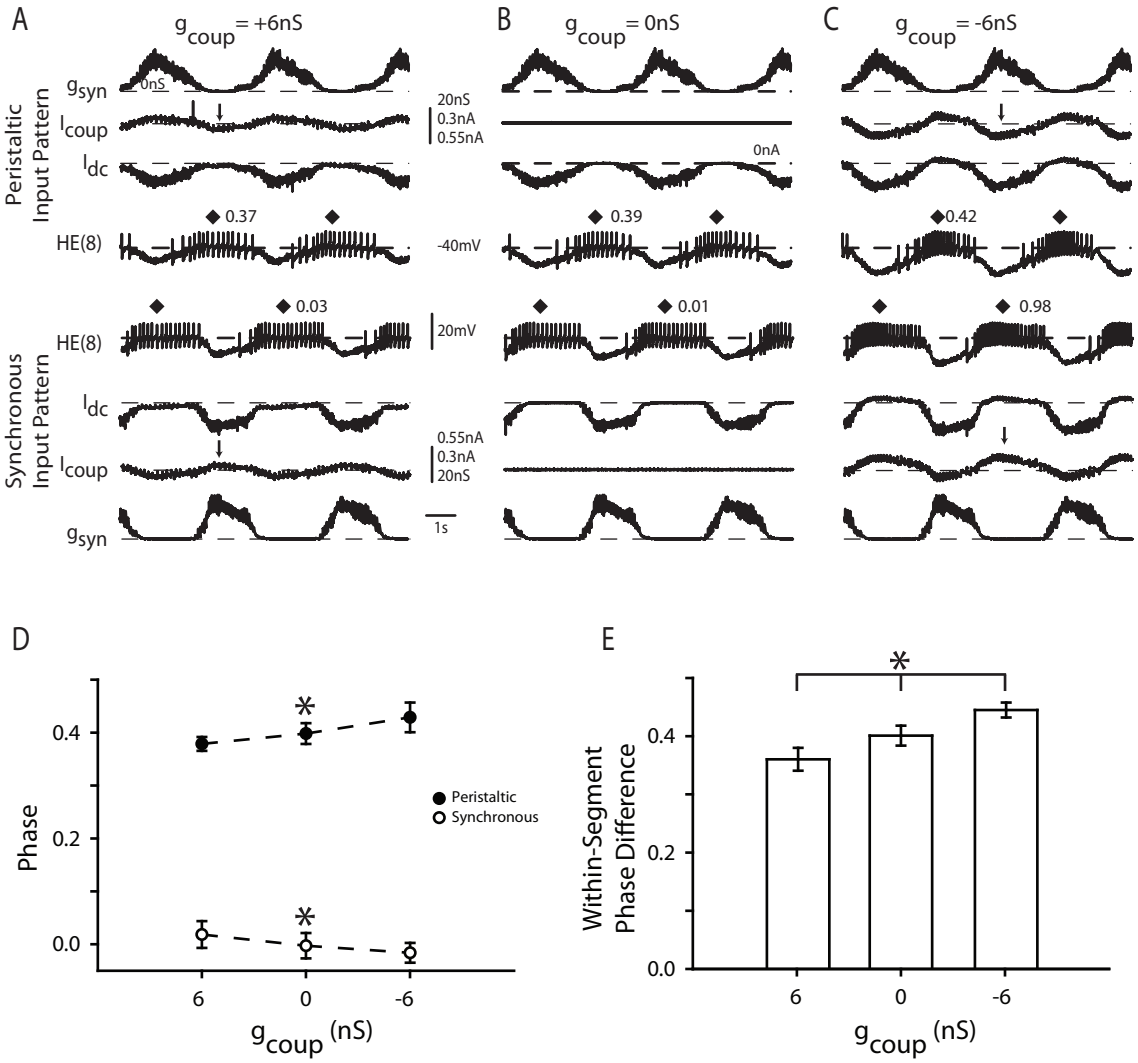
A
B
C
g_coup = +6nS
g_coup = 0nS
g_coup = -6nS
Peristaltic Input Pattern
Synchronous Input Pattern
g_syn
I_coup
I_dc
HE(8)
0nS
20nS
0.3nA
0.55nA
0nA
-40mV
20mV
1s
0.37
0.39
0.42
0.03
0.01
0.98
D
E
Phase
Peristaltic
Synchronous
g_coup (nS)
Within-Segment Phase Difference
0.0
0.2
0.4
6
0
-6

among segments; therefore, in addition to affecting segmental phasing, electrical coupling could also influence intersegmental coordination. Alternatively, in setting the coupling conductance to a negative value, we reverse the sign of the coupling current (i.e., I_{coup}), thus effectively canceling part or all of the endogenous coupling, potentially even adding net negative coupling. By removing endogenous coupling, we enhance the net effect of a given motor neurons own I_{Syn} and functionally uncouple the two motor neurons. Note that $-g_{coup}$ enhances the inhibition of one motor neuron during its inhibited phase (upper arrow on I_{coup}, Fig. 8*C*) as well as enhancing the depolarization of the contralateral motor neuron (lower arrow on I_{coup}, Fig. 8*C*). The net effect is a phase delay of the peristaltic motor neuron and a phase advance of the synchronous motor neuron, thus promoting a significant increase in side-to-side phase difference (Fig. 8*E*, 1-Way Repeated Measures ANOVA, $p < 0.05$).

Taken together, these results affirmed our modeling prediction that the electrical coupling between the heart motor neurons serves to synchronize their ongoing bursting activity. Although these results show that electrical coupling affected the phase of the heart motor neurons in the hybrid system, the synchronizing effect did not improve the correspondence between the hybrid and the living system in the peristaltic mode, nor did it change the good correspondence between the hybrid and living system in the synchronous mode.

DISCUSSION

The goal of the present investigation was to assess how motor neuron intrinsic properties contribute to rhythmic motor output. We used the leech heartbeat CPG, a system in which the pattern of premotor synaptic drive has been quantitatively defined, to address this question. Previously, we introduced a biologically derived input pattern into a canonical model of the ensemble of heart motor neurons in which their intrinsic electrical properties were kept to a minimum (García et al. 2008). While the model motor neurons captured the bilateral asymmetry observed in the living system, model output phasing was significantly different from that observed in the living system (Fig. 5, Table 1), suggesting a role for heart motor neuron intrinsic properties in producing their appropriate output phasing. Here, we constructed hybrid systems using segmental input patterns, which were derived from the living system and which were used in the canonical ensemble model. We show directly, in living motor neurons that receive these segmentally appropriate input patterns that motor neuron intrinsic properties do contribute to appropriate motor output phasing.

The segmental input pattern determines the segmental phase differences in heart motor neuron phasing

The same heart motor neuron (HE(8) and HE(14) motor neurons) responds differently to different synaptic strength profiles (i.e., the segment 8 and 14 synaptic strength profiles), while different motor neurons (segments 8 and 14) respond similarly to the same input pattern (the segment 8 input pattern, Fig. 4). This result implies that the segmental input pattern determines the phasing differences observed in motor neurons in segments 8 through 14 and that the intrinsic properties present in the heart motor neurons in these segments show no systematic segmental variation. In previous work with the heart motor neurons, Opdyke and Calabrese (1995) showed that passive properties (input resistance and capacitance) were not significantly different, particularly among heart motor neurons between segments 7 and 12. It was also shown that there were no significant differences in the maximal current measured for two of the outward currents, which are termed I_{K1} and I_{K2}, between these segments. Although measuring heart motor neuron inward currents at the level of the soma has proved difficult, these results suggest we should not expect to find significant differences among the inward currents in these segments.

The finding that the input pattern determines the segmental phasing differences observed in motor neurons is perhaps not surprising. In the absence of premotor synaptic input, the heart motor neurons fire tonically, and do not show intrinsic bursting oscillations (Schmidt and Calabrese 1992). Furthermore,

heart motor neurons do not appear to exhibit voltage sags indicative of the hyperpolarization-activated I_h current (Wenning and Calabrese, personal communication), a current which has been shown in neonatal rodent motor neurons to promote the transition from their inhibited phase to their firing phase (Kiehn et al. 2000). Therefore, in the absence of intrinsic oscillations and rebound-promoting currents, the output of the motor neurons should be largely determined by the input pattern they receive. Although heart motor neurons receiving the synchronous pattern of input show modest rebound spiking, this rebound spiking does not cause them to assume a phasing inconsistent with the segmental input pattern they receive.

If the segmental input pattern determines the segmental phasing differences observed in motor neurons, we might expect to find correlations between the premotor synaptic conductance and the output phasing observed in the living system. In the pyloric network of the stomatogastric system, for example, the onset of the LP motor neuron is correlated to the synaptic conductance of each of its inputs from the pacemaker kernel, the AB/PD complex (Goaillard et al. 2009). We do not see such correlations between single inputs and output phase in our system (Norris et al. 2011), suggesting that there may be a more complex interaction between elements of the premotor synaptic conductance pattern and the heart motor neuron intrinsic properties.

In our experiments, within a coordination mode, the only difference between the segmental input patterns introduced into the heart motor neurons

was the synaptic strength profile. The temporal pattern was the identical; therefore, we cannot determine, based on these results, what the relative contributions of the temporal pattern and the synaptic strength profile of a segmental input pattern are to motor neuron output phase or to intersegmental coordination. Hybrid experiments in which several temporal patterns and synaptic strength profiles are mixed and matched could help to address this question.

Heart motor neuron intrinsic properties are important for appropriate phasing

Despite the importance of the input pattern, we show that the intrinsic properties of heart motor neurons play a substantive role in determining their output. While it is well established that motor neuron intrinsic properties contribute to motor pattern generation in the pyloric (Marder and Bucher 2007) and gastric mill networks (Nusbaum and Beenhakker 2002) of the crustacean stomatogastric system, almost all of the neurons within those CPGs are themselves motor neurons, and the stomatogastric system is not segmentally distributed like the leech heartbeat system. Because we used the identical segmental input patterns used in our canonical ensemble model, any differences between the hybrid system and model phasing should be attributable to the additional intrinsic properties of the living heart motor neurons not present in the model motor neurons. Specifically, for motor neurons receiving the

synchronous pattern of synaptic input, regardless of the segmental strength profile, the intrinsic properties of the motor neurons promote a phase advance (compared to the canonical ensemble model) sufficient to match the phasing observed in the living system. In many cases, this phase advance is substantial: in each of the segments tested, the average phase advance per segment (compared to the ensemble model) is at least 0.09. While we are unable to determine what set of intrinsic properties are present in the heart motor neurons, a likely candidate could be a low-threshold calcium current. In the experiments where endogenous inputs were blocked with 0 Ca^{2+} high Mn^{2+} instead of bicuculline methiodide, hybrid system synchronous phasing was delayed (although not significantly so) by approximately 0.02 when compared to bicuculline methiodide block. This shift in phase may serve as an estimate of the contribution of such a current to the output phasing of these motor neurons. Addition of a low-threshold Ca^{2+} current to the model motor neurons, therefore, could provide a phase advance compared to the canonical ensemble model.

Our inability to replicate, in the hybrid system, a similar correspondence between the hybrid system and the living system in the peristaltic mode, is surprising. Across segments, heart motor neurons receiving the peristaltic pattern of synaptic input show phasing similar to the ensemble model. We do not attribute these discrepancies to experimental or procedural errors; furthermore, all of the appropriate inputs are accounted for in the segmental input patterns that were used in our model and dynamic clamp experiments (Norris et al. 2011). A modulatory extrinsic input, acting on a cycle-by-cycle basis, may contribute to

peristaltic phasing, but as of yet, no such inputs have been identified in the leech. One final possibility is that, because we are using the identical inputs in every experiment in the presence of the normal intrinsic properties of the heart motor neurons, we are not accounting for natural animal-to-animal variability in both the temporal pattern and synaptic strength profiles. We are currently exploring how natural variability of both the temporal pattern and synaptic strength profiles affect output phasing.

Heart motor neurons escape rhythmic inhibition, while model motor neurons are released from inhibition

We used trapezoidal waveforms designed to control when a motor neuron initiated its firing (Fig. 6). By constraining the onset of heart motor neuron firing until at or very near the offset of the premotor synaptic conductance, we were able to delay middle spike phase in a manner similar to that observed in the model motor neurons. Alternatively, waveforms that allowed for an earlier onset of motor neuron firing during the premotor synaptic conductance show phasing consistent with that measured in our hybrid system experiments with natural synaptic input patterns. This result suggests a fundamental difference between how motor neurons in the living system and the ensemble model may integrate their inputs: heart motor neurons in the living system seem able to escape inhibition by beginning to fire at a point where the synaptic conductance is still

ongoing (note the difference in first spike phase between the hybrid system and model, Fig. 5*E*). Model motor neurons, on the other hand, initiate firing only when the synaptic conductance has fallen to a lower conductance value; i.e., model motor neurons fire when they are nearly fully released from inhibition (Sharp et al. 1996). These results also suggest potential improvements to the model motor neurons; we are currently revising our canonical model to account for the spatial extent of the motor neurons in the living system as well as implementing inward currents that may affect their response to segment-specific patterns of synaptic input (Lamb et al. 2010).

Electrical coupling synchronizes ongoing heart motor neuron activity within a segment

Adding artificial electrical coupling via dynamic-clamp promotes synchronization of phase between heart motor neurons in the same segment. This observation is consistent with our previous modeling efforts (García et al. 2008), as well as observations in *Xenopus* embryos (Zhang et al. 2009). This result suggests that electrical coupling also contributes to the output phasing observed in the living system. The synchronizing effect of the artificial coupling did not improve the correspondence in peristaltic phase between the hybrid system and the living system. Because the artificial coupling was added at the soma, distant from the potential endogenous coupling sites on fine neurites

(Tolbert and Calabrese 1985), the synchronizing effect shown here may represent the lower physiological limit of the synchronizing effect observed in the living system.

Electrical coupling may also influence intersegmental coordination. When similar (although using different values of g_{coup}) hybrid experiments were done in segment 14 receiving the segment 14 input pattern, the reduction in side-to-side phase difference in segment 14 was smaller than that measured in segment 8. At present, we cannot distinguish whether this segment-specific effect is due to side-to-side phasing in the input pattern, as suggested in out ensemble model (García et al. 2008), or possibly due to segmental variation in the coupling between heart motor neurons. A systematic survey of the coupling coefficients between heart motor neurons in the mid-body segments could address this question.

Larger implications

The results presented here show that motor neuron intrinsic properties can make a functional contribution to motor output in the context of an ongoing rhythmic input. Work in the cat spinal cord (Lee and Heckman 1998), neonatal rodent spinal cord (Kiehn et al. 2000), hypoglossal motor neurons (Bayliss et al. 1994; Berger 2000) and turtle fictive scratch (Hounsgaard and Kiehn 1989) have

all shown that motor neurons in these preparations possess intrinsic properties (and electrical coupling) that appear ideally suited to influence the phase and intensity of motor output. Our work suggests that a prerequisite for assessing how motor neuron intrinsic properties in these preparations contribute to motor output will be a quantitative description of the premotor pattern of synaptic input. For example, recent studies in which the pattern of premotor synaptic drive to motor neurons in the neonatal rodent spinal cord (Endo and Kiehn 2008) and turtle fictive scratch (Berg et al. 2007) were decomposed into their inhibitory and excitatory components were used to make inferences about the composition of the premotor interneuronal networks that drive these motor patterns. The identities of the neurons that make up these networks and their connections are still being identified. The strength of the current study is that we have identified the constitutive premotor elements and their relative contributions to the inhibitory synaptic drive impinging upon the motor neurons in this system. By focusing on those segments in which the premotor inputs have been clearly defined, we have provided the relevant context to ascertain how motor neuron intrinsic properties may contribute to motor output.

CHAPTER 3

Patterns of presynaptic activity and synaptic strength interact to produce motor output

ABSTRACT

Studies have begun to measure rhythmic patterns of premotor synaptic drive onto motor neurons in order to generate models of how motor neuron activity is coordinated by premotor networks into a functional motor pattern. These patterns of synaptic drive combine both the temporal pattern of spikes and the profile of synaptic strengths (i.e., conductances) of the premotor network. Given the complexity of these premotor networks, it is difficult, at present, to ascertain what the relative contributions of temporal patterns and synaptic strength profiles are in the production of the rhythmic motor patterns observed. Here, we use the leech heartbeat CPG, in which we can measure both the temporal pattern and the synaptic strength profiles of the premotor network to address how they combine to produce functional output, using a modeling and hybrid-systems approach. Segmental heart motor neurons are coordinated either in a synchronous or in a peristaltic pattern. We show that the synchronous motor pattern is a consequence of the nearly synchronous premotor activity (temporal pattern) produced by the leech heartbeat CPG. For the peristaltic motor pattern, we show that the premotor temporal pattern determines the phase range over which segmental motor neurons can fire while synaptic strength profiles define

the segmental phase progression realized. Finally, we propose a metric that captures the effectiveness of a given synaptic strength profile and predicts an optimal synaptic strength profile for realizing the maximal phase progression determined by the premotor temporal pattern.

INTRODUCTION

To produce rhythmic movements such as walking, nervous systems must produce rhythmic activation of the motor neurons that underlie these movements. Typically, these rhythmic patterns are generated by central pattern generators (CPGs, (Marder and Calabrese, 1996)), rhythmically active networks of neurons capable of producing the pattern in the absence of sensory feedback (i.e., the fictive pattern). The rhythmic synaptic drive to motor neurons (either excitatory or inhibitory) provided by a CPG is produced by the temporal pattern of spikes in premotor interneurons (i.e., the temporal pattern) combined with the patterns of strengths in the synaptic connections (i.e., the synaptic strength profiles) of the premotor interneurons onto motor neurons.

The time-varying synaptic conductances in motor neurons of the hindlimb locomotor network (Endo and Kiehn, 2008) and turtle scratch (Berg et al., 2007) have been decomposed into their excitatory and inhibitory components in order to understand how the premotor networks that generate the synaptic

conductances are organized. Because of the complexities of the hindlimb locomotor and turtle scratch networks, however, it has proved difficult to determine the relative contribution of the temporal pattern and synaptic strength profiles to functional motor output. Indeed, in only a few vertebrate preparations (Biro et al., 2008; Soffe et al., 2009; Gabriel et al., 2011) have candidate premotor interneurons been identified so that a temporal pattern can be matched with synaptic strength profiles. Invertebrate preparations, with their simple and accessible nervous systems, have provided many insights into how temporal and synaptic strength profiles combine to generate motor patterns (Marder and Bucher, 2007; Johnson et al., 2011).

In the present study, we used the leech heartbeat CPG to assess what the relative contributions of temporal pattern and synaptic strength profiles are in the production of functional motor output. Previously (Norris et al., 2011), we showed that, in spite of considerable animal-to-animal variability of input (both temporal pattern and synaptic strength profiles) and output pattern in this system, functional output is maintained. In that study, we concluded that each animal appears to generate its own pairing of temporal pattern and synaptic strength profile such that appropriate motor patterns are always observed. Here we explore what rules govern how temporal patterns and synaptic strength profiles are combined so that functional motor patterns emerge. We show that the temporal pattern sets the limits of motor output (in this case intersegmental coordination) that can be expressed, whereas the pattern of synaptic strength determines where within these limits motor output will fall. We also show that

inappropriate synaptic strength profiles produce non-functional output patterns even when the temporal pattern is appropriate. Finally, we introduce a metric that describes how a pattern of synaptic strength affects intersegmental coordination when paired with a temporal pattern. We conclude that the limits of motor output set by the temporal pattern are sufficient to accommodate the variability in synaptic strength profiles observed across animals so that functional motor output is assured.

METHODS

Animals and solutions

Leeches (*Hirudo sp.*) were purchased from a commercial supplier (Leeches USA, Westbury NY) and maintained in artificial pond water at 15° C. Animals were anesthetized in ice, then dissected in chilled saline. Individual ganglia from midbody segments 8 and 12 were dissected and pinned out, ventral surface up, in 35 mm Petri dishes lined with Sylgard™ (184, Dow Corning, Midland, MI). The ventral sheath of the ganglion was removed with fine scalpels in all experiments. We superfused the preparation with leech saline containing (in mM: 115 NaCl, 4 KCl, 1.8 glucose, 10 HEPES buffer and 1.8 CaCl2 adjusted to a pH of 7.4 using NaOH) at 1-2 ml/min in a bath volume of 0.5-1 mL. All experiments were performed at room temperature. Heart motor neurons were

identified based on soma location on the ventral aspect of the ganglion, soma size and by their characteristic activity of alternating bouts of firing interrupted by barrages of inhibitory post-synaptic potentials (IPSP's). In all experiments in this study, 10^{-4} M bicuculline methiodide was added to the leech saline after cell identification to block inhibitory synaptic input to heart motor neurons (Schmidt and Calabrese, 1992).

Intracellular Recording Techniques

For intracellular voltage recordings from heart motor neurons, we used sharp microelectrodes (~25-40 MΩ filled with 2 M KAc and 20 mM KCl) made from borosilicate glass (1.0 mm outer diameter; 0.75 mm inner diameter; AM Systems, Sequim, WA). Intracellular recordings and current injections were made using an Axoclamp-2A amplifier (Molecular Devices, Sunnyvale, CA) in Discontinuous Current Clamp (DCC) mode using a sampling rate of 2.5-3.0 kHz. To ensure electrode settling, the electrode potential was monitored with an oscilloscope.

In all experiments, both heart motor neurons in a given ganglion were impaled and recorded simultaneously. After penetration, the input resistance of both cells was measured using -0.3 nA pulses. We did not proceed with experiments unless the input resistance of both motor neurons was > 30 MΩ, and the difference in input resistance between the two heart motor neurons was < 15 %. Upon termination of the experiment, the microelectrode was withdrawn from

the cell and the electrode potential was recorded. Only experiments in which the electrode potential was within $\pm$ 5 mV of ground were accepted in this study. Thus, holding potential were normally accurate within $\pm$ 5 mV.

Data Acquisition

Data were digitized (5 kHz sampling rate) using a digitizing board (Digi-Data 1200 Series Interface; Molecular Devices) and acquired using pCLAMP 9.2 (Molecular Devices) on a personal computer (Dell, Round Rock, TX).

Standard Heart Motor Neuron Ensemble Model

We first assessed the relative contributions of premotor temporal patterns and patterns of synaptic strengths using a previously developed model of the ensemble of heart motor neurons (García et al., 2008). The temporal pattern is the series of spike times in all 4 premotor heart interneurons in the peristaltic and synchronous modes, while the pattern of synaptic strengths (in this study referred to as the synaptic strength profile) is the distribution of synaptic conductances elicited by each premotor heart interneuron in a postsynaptic heart motor neuron. Briefly, the motor neurons in this model were single-

compartment, conductance-based models whose membrane potential (V_m) is given by the following current-balance equation:

$$C\frac{dV}{dt} = -(I_{Na} + I_P + I_{KA} + I_{K1} + I_{K2} + I_{leak} + I_{coup} + I_{Syn} + I_{inject})$$

where t is time, C is the total membrane capacitance, I_{leak} is the leak current, I_{coup} is the current due to electrical coupling between the heart motor neurons in a given segment, I_{Syn} is the sum of the inhibitory synaptic currents arising from each of the premotor inputs and I_{inject} is any injected current. The model motor neurons contained five voltage-gated currents: 1) a fast Na^+ current (I_{Na}), 2) a persistent Na^+ current (I_P), 3) a fast transient K^+ current (I_{KA}), 4) an inactivating delayed rectifier K^+ current (I_{K1}) and 5) a non-inactivating delayed rectifier K^+ current (I_{K2}). The Hodgkin-Huxley equations (Hodgkin and Huxley, 1952) describing these voltage-gated currents were the same as those used in a model of an oscillator heart interneuron model (Hill et al., 2001). Each motor neuron was modeled as an isopotential cylinder whose length and diameter were both 60 μm with a specific membrane resistance of 1.1 Ωm^2 and a specific membrane capacitance of 0.05 Fm^{-2}. With these parameters, the input resistance of a model motor neuron was 97 MΩ. The maximal conductances of the individual ionic currents as well as electrical coupling were set empirically so that the activity of the model motor neurons mimicked those observed during intracellular recordings of heart motor neurons in the absence of synaptic input (García et al., 2008). The heart motor neuron ensemble model was implemented in GENESIS

(General Neural Simulator System), with each model motor neuron receiving its segment-appropriate temporal pattern and synaptic strength profile (see below). The model used the Euler integration method with a time step of 0.0001 s. We recorded and saved the computed synaptic conductance waveforms arising from each premotor input as described below as well as their sum (g_{Syn}; B_2, Fig. 1) in each motor neuron for subsequent use in the dynamic clamp (see below).

Derivation of Synaptic Input Patterns Used in Model Simulations

The model motor neurons received an inhibitory synaptic input pattern that consisted of both a temporal pattern and synaptic strength profile; both components were determined from 6 physiological experiments of the type performed by Norris et al (2011) as described below.

For the model motor neurons, the temporal pattern of the premotor heart (HN) interneurons were taken from simultaneous extracellular recordings of the ipsilateral HN(3), HN(4), HN(6) and HN(7) premotor interneurons in both the peristaltic and synchronous coordination modes. For each preparation, the peristaltic and synchronous input patterns were aligned to each other to create a bilateral input pattern – left synchronous-right peristaltic – by assigning a phase of 0.0 to the middle spike of the first peristaltic HN(4) premotor interneuron burst (therefore, the peristaltic HN(4) premotor interneuron is our absolute

phase reference) and a phase of 0.51 to the middle spike of the first burst of the synchronous HN(4) premotor interneuron. These phase values match the average phase difference between the two HN(4) interneurons as measured in the living system (Norris et al., 2006). Each segmental pair of model motor neurons received the same temporal pattern (one peristaltic, the other synchronous) offset by an intersegmental conduction delay of 20 ms per segment. Thus the model heart motor neurons in segment 12 receives the same temporal pattern as the model heart motor neuron in segment 8, offset by 80 ms. Because the spike timings used in our temporal patterns come from living preparations, the temporal patterns are not precisely regular and therefore the average phases presented for model simulations display a variance.

The distributions of synaptic conductances (A_2, Fig. 1) elicited by each premotor heart interneuron in a postsynaptic heart motor neuron (referred to here as an individual heart motor neurons synaptic strength profile) were also derived from the 6 preparations in which the temporal patterns were measured as in Norris et al (2011). In that study, they recorded from each of the premotor heart interneurons, as described above, and then voltage clamped the HE(8) followed by the HE(12) motor neurons. They recorded spontaneous IPSC's in the heart motor neurons arising from activity in the premotor interneurons for multiple bursts in each coordination mode. From these recordings, they generated spike-triggered averages of the IPSCs for each presynaptic heart interneuron. They selected the peak of the spike-triggered average as their measure of an individual premotor heart interneurons synaptic input. These

IPSC's were converted to conductances using a reversal potential of -62 mV (Angstadt and Calabrese, 1991). The set of 4 maximal conductances ($g_{SynHN(i)}$) is unique to each segmental motor neuron pair, thus each motor neuron pair has a unique synaptic strength profile. Each model motor neuron pair received their segment-specific synaptic strength profile. In the model, each premotor heart interneuron spike elicited a unitary synaptic conductance that followed a double exponential function scaled by the synaptic weight for that input in that motor neuron ($g_{SynHN(i)}$). The model computes $g_{Syn}(t)$ from the sum of the 4 individual inhibitory synaptic conductances ($g_{SynHN(i)}$) associated with a particular presynaptic input HN_i. The heart motor neuron ensemble model with standard cellular parameters (García et al., 2008) is referred to here as the standard ensemble model. In this study, we varied the input patterns introduced to the ensemble model motor neurons; the cellular parameters of the model motor neurons, including electrical coupling were held constant.

Heart motor neuron ensemble model simulations

The temporal patterns and synaptic strength profiles used as inputs to the standard ensemble model were taken from 6 preparations ($A_{1\text{-}2}$; Fig. 1) from Norris et al (2011) as described above. In figures and text, these preparations will be identified by the date in 2009 on which the experiments were performed. In one series of simulations (here referred to as "home" simulations), the temporal

FIG 3.1. Heart motor neuron ensemble model input pattern characteristics and hybrid system implementation. A_1: Simplified bilateral phase diagram of the four premotor heart interneurons and the HE(8) and HE(12) motor neurons measured in 6 experimental preparations denoted by the date on which the experiments occurred. The letter next to the date denotes the prep number for that date (A = first, B = second). The line connecting the same colored symbols show the intersegmental phase relationships between the premotor HN interneurons for both the peristaltic and synchronous coordination modes. Motor output is shown opposite its matched premotor input pattern. The color/symbol schemes for the preparations and premotor heart interneurons were conserved throughout the study: blue/diamond: May 19A, red/square: May 19B, green/triangle: May 20B, purple/X: May 22B, cyan/ж: May 26A, orange/circle: May 27B, dark blue/circle: HN(3) interneuron, dark green/triangle: HN(4) interneuron, magenta/square: HN(6) interneuron and cyan/diamond: HN(7) interneuron. The boxes around preparations 5/19A, 5/22B and 5/27B indicate that these preparations were used both in modeling studies as well as in hybrid system experiments. A_2: Synaptic strength profiles associated with each of the six temporal patterns in A_1. The relative synaptic strength profiles for each premotor heart interneuron input onto the HE(8) (top) and HE(12) (bottom) heart motor neurons. The data for A_1 and A_2 are from Norris et al (2011) are shown. B_1: Hybrid system setup. We recorded simultaneously from a pair of heart motor neurons ($V_{HE(L,i)}$ and $V_{HE(R,i)}$) from a given segment, and pharmacologically isolated the motor neurons from their premotor heart interneuron inputs. The dynamic clamp computes and injects, in real time, the

artificial equivalent of the appropriate synaptic current (I_{dc}), into the heart motor neurons. B_2: Exemplar dynamic-clamp experiment and determination of phase in the hybrid system experiments. At the beginning of the voltage recording, the heart motor neurons were firing tonically; g_{Syn} is 0 nS. The vertical line shows when the dynamic-clamp synapse was activated. The dynamic clamp injects a time-varying current (I_{dc}) proportional to the synaptic conductance g_{Syn}. In subsequent figures, I_{dc} is omitted and only g_{Syn} is shown. The vertical green lines on the peristaltic trace represent the middle spike of our phase reference, the peristaltic HN(4) interneuron. The interval between the two green lines is the cycle period of the phase reference. The vertical green line on the synchronous trace represent the middle spike of the synchronous HN(4) interneuron. In subsequent figures, the middle spike of heart motor neuron bursts are indicated by a filled diamond and the average phase for an experiment is indicated next to it. The green vertical lines are omitted in subsequent figures.

Figure 3.1

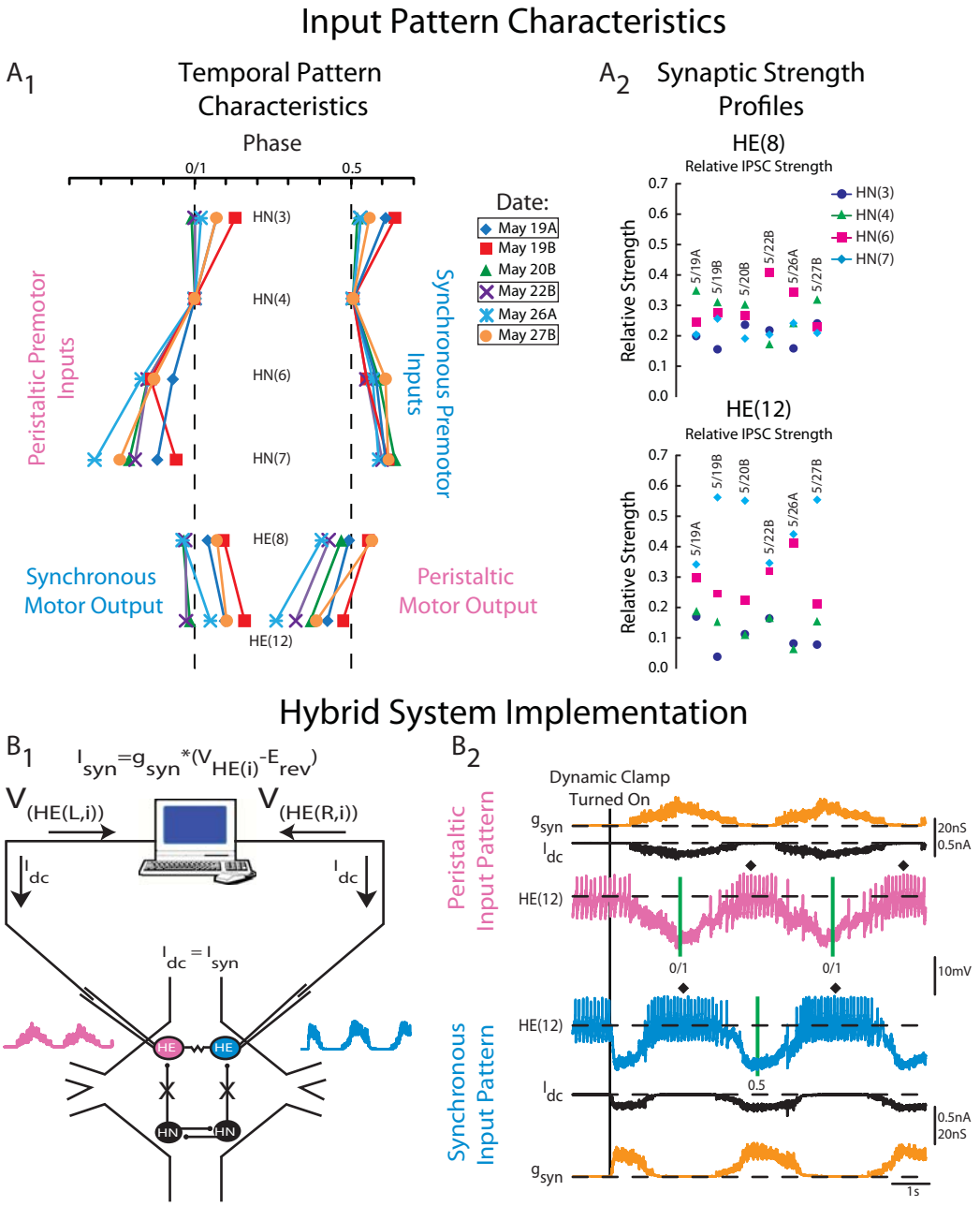
Input Pattern Characteristics
A1
Temporal Pattern Characteristics
Phase
0/1
0.5
HN(3)
HN(4)
HN(6)
HN(7)
HE(8)
HE(12)
Peristaltic Premotor Inputs
Synchronous Premotor Inputs
Date:
May 19A
May 19B
May 20B
May 22B
May 26A
May 27B
Synchronous Motor Output
Peristaltic Motor Output
A2
Synaptic Strength Profiles
HE(8)
Relative IPSC Strength
Relative Strength
HN(3)
HN(4)
HN(6)
HN(7)
5/19A
5/19B
5/20B
5/22B
5/26A
5/27B
HE(12)
Relative IPSC Strength
Hybrid System Implementation
B1
Isyn=gsyn*(VHE(i)-Erev)
V(HE(L,i))
V(HE(R,i))
Idc
Idc = Isyn
HE
HN
B2
Dynamic Clamp Turned On
gsyn
Idc
HE(12)
20nS
0.5nA
0/1
10mV
Peristaltic Input Pattern
Synchronous Input Pattern
0.5
1s

pattern was paired with its own synaptic strength profile. In another series of simulations (here referred to as “mixed” simulations), a given temporal pattern was paired with the 5 other synaptic strength profiles. The six preparations chosen were similar in period (range: 8.8-9.3 s), but varied both in their temporal patterns and their synaptic strength profiles.

To quantitatively compare the 6 temporal patterns, we computed the premotor progression for each input pattern in each coordination mode. The premotor progression (either peristaltic or synchronous) is defined as the difference in phase (defined below) between the last firing premotor interneuron and the first firing premotor interneuron. For example, the May 19A temporal pattern had a premotor peristaltic phase progression of 0.19 phase units, while the May 27B temporal pattern had a premotor peristaltic phase progression of 0.31.

To facilitate a comparison of the synaptic strength profiles, we designated a synaptic strength profile as being canonical in its order, if the following criteria were met: the strongest input (in terms of relative synaptic strength) in the HE(8) motor neuron arose from the HN(4) interneuron, while the strongest input in the HE(12) motor neuron arose from the HN(7) interneuron. Therefore, in the case of the HE(8) motor neuron, the synaptic strength profiles for May 19A and B, May 20B and May 27B are canonical in their order (although different in their relative values), while the May 22B and May 26A synaptic strength profiles are non-

canonical in their order. In the case of the HE(12) motor neurons, all the preparations are canonical in their order.

To compare simulation outputs amongst themselves, we computed the motor progression for each input pattern in each coordination mode. The motor progression (either peristaltic or synchronous) is defined as the difference in phase between the HE(12) motor neuron and the HE(8) motor neuron; negative motor progressions indicate that the HE(8) motor neuron leads the HE(12) motor neuron and vice-versa. We also computed the motor progressions of the same 6 preparation from which we derived the input patterns for use as model target values.

In some model simulations (and in follow-up hybrid system experiments), we inverted the May 27B synaptic strength profile in order to test the effect of the disparity in strength of the HN(4) and HN(7) interneurons in the HE(8) and HE(12) motor neurons on the motor progression between these two motor neurons. Based on the average synaptic strength profiles presented by Norris et al (2007a), the strongest input, on average, to the HE(8) motor neuron arises from the HN(4) interneuron, while the strongest input, on average, to the HE(12) motor neuron arises from the HN(7) interneuron. In our inverted synaptic strength profile, we made the HN(4) interneuron input the weakest in segment 8 and made the HN(7) input the strongest, while in segment 12, we made the input from the HN(7) interneuron the weakest and the input from the HN(4) interneuron the strongest. In the HE(8) motor neuron, we inverted the May 27B

synaptic strength profile by exchanging the synaptic conductance value of the HN(4) interneuron with that of the HN(7) interneuron and by exchanging the synaptic conductances of the HN(3) and HN(6) interneurons. In the HE(12) motor neuron, we inverted the May 27B synaptic strength profile in the following manner: 1) we made the HN(7) interneuron the weakest relative input by setting its synaptic conductance to that of the weakest input, the HN(3) interneuron, 2) we made the HN(4) interneuron input the strongest relative input by setting its conductance to that of the HN(7) interneuron and 3) we set the synaptic conductance of the HN(3) interneuron to that of the HN(6) interneuron and the HN(6) synaptic conductance to that of the HN(4) interneuron. With these changes in assignment of the synaptic strengths, we assessed how these artificial synaptic strength profiles affected both synchronous and peristaltic motor progressions in model and hybrid system experiments.

Hybrid System Design and Implementation

We used the dynamic clamp (Sharp et al., 1993; Sorensen et al., 2004) to produce a virtual version of the HN-HE synapse. The dynamic clamp both computes and injects, in real time (time step: 0.0001 s), a model of the synaptic current (I_{Syn}) based on the intracellularly recorded membrane potential (V_m), a time-varying conductance ($g_{Syn}(t)$) and a reversal potential (E_{Syn}), implemented according to Ohms Law. Because we are linking a synapse-model with heart

motor neurons in the living system, we refer to these preparations as hybrid systems. The dynamic-clamp synapse was implemented according to the following equation:

$$I_{Syn} = \sigma g_{Syn}(t)(V_m - E_{Syn})$$

where I_{Syn} is the synaptic current, $g_{Syn}(t)$ is the time varying synaptic conductance waveform representing the sum of all the individual synaptic inputs to a model motor neuron, σ is a parameter used to scale $g_{Syn}(t)$, V_m is the membrane potential of the motor neuron, and E_{Syn} is the synaptic reversal potential (Angstadt and Calabrese, 1991). To generate the synaptic conductance waveforms introduced in our hybrid system experiments, we extracted $g_{Syn}(t)$ from ensemble model simulations (see above). For simplicity, we label $g_{Syn}(t)$ as g_{Syn} in figures and text (*B₂,* Fig. 1). The synaptic conductance waveforms used in our hybrid system experiments were the same as in the ensemble model, except they were scaled by σ. The scaling factor allowed us to increase the overall synaptic conductance while preserving the relative synaptic strength of the individual premotor synaptic conductances.

All dynamic-clamp calculations were performed using a real-time dedicated processing board (DS1104, dSPACE, Detroit, MI). We activated the dynamic-clamp synapse only when motor neurons were spiking tonically and had no discernible inhibitory postsynaptic potentials in the voltage recording (*B₁-₂*, Fig. 2). We introduced the following synaptic conductance waveforms in the

HE(8) and HE(12) motor neurons: 1) the May 19A temporal pattern paired with its synaptic strength profile, 2) the May 27B temporal pattern paired with its synaptic strength profile, 3) the May 27B temporal pattern paired with the May 22 synaptic strength profile and 4) the May 27B temporal pattern paired with the inverted version of the May 27B synaptic strength profile (described above). In each experiment, we introduced 11 cycles of inhibitory synaptic conductance, yielding 10 bursts of activity.

Data Analysis

Electrophysiological data were analyzed offline using a combination of pCLAMP 9.2 (Molecular Devices) and custom scripts written in Matlab (The Mathworks, Natick, MA) and Spike2 (CED Systems, Cambridge, UK). First, the raw voltage recordings were high-pass filtered (cut-off frequency ~ 1 Hz). These data were then used for spike detection. Spike detection was carried out using methods reported previously (Norris et al, 2006).

After detection, spikes were grouped into bursts as follows: after an interburst interval of 500 ms, the next spike detected was considered the first spike in that burst. Each subsequent spike was included in that burst until the interspike interval greater than 500 ms (i.e., the interburst interval) was

encountered. A minimum of four spikes were required in order to qualify as a burst.

We define period as the interval between successive middle spikes of the peristaltic HN(4) interneuron ($T_{HN(4)}$). We then computed the phase of the heart motor neurons with respect to the synaptic input pattern that they received. We define phase as the difference in time for a spike of interest of a heart motor neuron (or interneuron) and the time of the middle spike of the phase reference, the peristaltic HN(4) interneuron $T_{HN(4)}$. This difference is then normalized to the cycle period of the phase reference, given by:

$$\phi = (\Delta t_{HE(i)-HN(4)})/T_{HN(4)}$$

We calculated the average middle (m) spike phase, burst period (T) and duty cycle (D) for each heart motor neuron. In the text and figures, the generic term phase and symbol ϕ are applied to the middle spike phase as defined above. In figures, we indicate the middle spike phase of a heart motor neuron (model or living) within each burst by a filled diamond above that burst. All phase values are expressed modulo one. Duty cycle is defined as the difference between the average last spike phase and the average first spike phase:

$$D = \phi_{last} - \phi_{first}$$

Because the duty cycle is the difference of two averages, a standard deviation is not reported.

To assess the relative contribution of the synaptic strength profile within a segment to intersegmental phase, we computed a synaptic strength index (SSI). The synaptic strength index is defined as:

$$SSI = \frac{Relative\ HN(4)_{HE(8)}}{Relative\ HN(4)_{HE(12)}} + \frac{Relative\ HN(7)_{HE(12)}}{Relative\ HN(7)_{HE(8)}}$$

where $Relative\ HN(i)_{HE(j)}$ is the relative synaptic strength of premotor HN interneuron i in the HE motor neuron in segment j. The SSI assesses the summed disparity in te strength of the two key premotor HN(4) and HN(7) inputs in the HE(8) compared to the HE(12) motor neurons. The HN(4) input is typically the strongest in the HE(8) and is rather weak in the HE(12) motor neuron, while the HN(7) input is typically the strongest in the HE(12) motor neuron and is rather weak in the HE(8) motor neuron.

Statistics

Data were compiled and analyzed using Microsoft Excel (2010, Microsoft, Redmond, WA), SigmaPlot 11 (Systat Software, San Jose, CA), Minitab (v14, Minitab, State College, PA) or Matlab (The Mathworks). We generated an average

phase and duty cycle for each preparation, and the average (± SD, n = 6) across animals was used for all statistical analyses. We analyzed all phases using a One-Way Repeated Measures ANOVA. In the hybrid system experiments, our *a. priori* comparisons of interest were between the May 19A home simulation synaptic conductive waveform (i.e., temporal pattern matched with its synaptic strength profile), the May 27B home simulation synaptic conductance waveform and the May 27B temporal pattern paired with the May 22 synaptic strength profile synaptic conductance waveform. Therefore, we used pairwise *t*-tests as follow-ups to the ANOVA. Statistical significance was set at $p < 0.05$ for all statistical tests.

RESULTS

Background

The leech heartbeat system has been described in detail (Kristan et al., 2005; Norris et al., 2006; Norris et al., 2007a, b) so we briefly summarize here. Blood flow in the medicinal leech is driven by the rhythmic constriction of a bilateral pair of heart tubes, with one heart tube constricting with a rear-to-front pattern (i.e., peristaltic), while the other heart tube constricts nearly synchronously along its length (i.e., synchronous). The heart tubes receive excitatory input from an ipsilateral member of a pair of heart (HE) motor

neurons, located in midbody segments 3-18 of the 21 midbody segmental ganglia (Maranto and Calabrese, 1984a, b). The firing pattern of the heart motor neurons (i.e., the fictive motor pattern) is bilaterally asymmetric, with motor neurons on one side firing with a rear-to-front progression while those on the other side fire nearly synchronously with appropriate side-to-side coordination of these two firing patterns (Wenning et al., 2004a; Wenning et al., 2004b). The heart motor neurons in segments 7 through 14 receive rhythmic inhibitory input from the ipsilateral member of each of four pairs of heart [HN(3), HN(4), HN(6) and HN(7)] interneurons within the heartbeat CPG (Norris et al, 2007a,b). The firing pattern of the premotor interneurons is also bilaterally asymmetric like that of the heart motor neurons and with appropriate side-to-side coordination. The asymmetry in firing patterns is not permanent, however; there are regular side-to-side switches in the peristaltic and synchronous patterns in the heart interneurons that underlie the changes in both the fictive motor pattern and the rhythmic constriction patterns of the heart tubes. We have been able to measure quantitatively both the firing pattern (the temporal pattern; Norris et al. 2006) of the premotor inputs and the pattern of synaptic strength of each of the premotor interneurons (the synaptic strength profile, Norris et al 2007b, Norris et al, 2011). While there is a considerable amount of animal-to-animal variability in both of these components of the premotor input pattern as well as in the motor output pattern (Norris et al., 2011), functional peristaltic and synchronous motor patterns were always observed.

Standard Ensemble Model Simulations: Segmental Motor Phase

We began our investigation into the relative contributions of premotor temporal patterns and synaptic strength profiles to motor neuron coordination by performing simulations with our previously developed model of the ensemble of heart motor neurons (García et al., 2008). We selected 6 preparations (from a total of 12), identified by the date on which the experiment took place in 2009, in which both the temporal pattern, synaptic strength profiles and motor output had been measured in the living system (Fig. 1A, Norris et al., 2011). These 6 preparations represent our physiological dataset; the phase of the HE(8) and HE(12) motor neurons as well as the motor progressions (the difference in phase between the HE(12) motor neuron and the HE(8) motor neuron) of these preparations represent target phases or motor progressions to which we compared our model output. The preparations selected were similar in period in the peristaltic and synchronous modes and showed modest variability across preparations (range of periods: 8.6 - 9.3 s). These preparations, however, displayed considerable variability in the premotor progression of their temporal patterns (the difference in phase between the last firing premotor interneuron and the first firing premotor interneuron) (A_1, Fig. 1), their synaptic strength profiles (A_2, Fig. 1), which varied in their relative synaptic strengths and in their order of synaptic strengths, and finally in their motor progression (A_1, Fig. 1, lower panel). In the synaptic strength profiles, there are clear trends, despite this variability, which allow us to define a canonical order for the relative synaptic strength in each segment. Nevertheless, some synaptic strength profiles in our

data set are non-canonical in their order in the HE(8) motor neuron (e.g., the HN(6) interneuron is the strongest input in the May 22B synaptic strength profile; see Methods). We ran simulations in which a temporal pattern was matched with 1) its own synaptic strength profile (i.e., home simulations) or 2) the other 5 synaptic strength profiles (i.e., mixed simulations). In the case of the home simulations, our target phase (or motor progression) was the home simulation's physiological counterpart (e.g., we compared the May 27B home simulation to the May 27B physiological preparation); in the mixed simulations, our target phase (or motor progression) was the phase observed for a given temporal pattern (for example, a simulation in which the May 27B temporal pattern was matched with the May 22B synaptic strength profile phase was compared to the phase or motor progression observed in the May 27B physiological preparation). To facilitate simulation comparisons, where data are presented in a Table, temporal patterns are listed on the row; therefore, comparisons to the appropriate target phase or motor progression are made by reading across a row. In all simulations, the cellular properties of the model motor neurons were held constant at their standard values (García et al., 2008).

In our previous modeling study (García et al., 2008), we found that HE(8) model motor neurons were phase delayed when compared to the living system in the synchronous mode and phase advanced when compared to the living system in the peristaltic mode. In that study (García et al., 2008), we paired a specific temporal pattern (i.e., a temporal pattern from one preparation) with a synaptic strength profile based on the average synaptic strength profiles measured in the

living system (Norris et al, 2007a). We then compared model output to our averaged motor neuron phase data (Norris et al., 2007b). It was possible, therefore, that the discrepancy in phase between the model and living system was due, in part, to our failure to account for the animal-to-animal variability in temporal patterns, synaptic strength profiles and output phase previously reported in the living system (Norris et al., 2011). Here, we address this possibility directly by using multiple input patterns and then comparing ensemble model output to a target phase (as defined above). Table 1 shows the phasing observed in the HE(8) model motor neuron in both modes with each of the 6 home simulations shown on the diagonal, while the mixed simulations are shown on the off-diagonal.

In the synchronous mode home simulations (diagonals, Table 1), HE(8) model motor neuron phases were delayed when compared to their target phases (average delay: 0.05), just as in our previous modeling work (García et al., 2008). In those physiological preparations where phase was delayed sufficiently (at least 0.03 phase units; May 19A, May 19B and May 27B) when compared to the average phase of the physiological dataset (0.02), home simulation phases were near (within 0.03 phase units) to their target phases. In those physiological preparations where the HE(8) model motor neuron was phase advanced when compared to the average phase (May 20B, May 22B and May 26A), home simulation phases were delayed when compared to their target phases.

In the synchronous mode mixed simulations, changing the synaptic strength profile matched with a given temporal pattern resulted in both phase advances and delays when compared to the home simulations (rows, Table 1). In mixed simulations, the target phase was the living system phase observed for the temporal pattern on each row (as described above). For the home simulations where the model output approximated the target phase (the May 19A, May 19B and May 27B simulations), in only 1 case did mixing the temporal patterns and synaptic strength profiles provide a phase advance beyond its target phase (i.e., the May 27B temporal pattern matched with the May 19A synaptic strength profile compared to the May 27B HE(8) motor neuron phase). In those simulations where a home simulation phase was delayed compared to the target phase (i.e., May 20B, May 22B and May 26A home simulations), no combination of temporal patterns and synaptic strength profiles provided a phase advance large enough to cause the model phase to approximate a temporal pattern's target phase. In all other cases, the correspondence between the model and target phase was either unaffected or became worse.

In the peristaltic mode home simulations (diagonals, Table 1), HE(8) model motor neurons were phase advanced when compared to their target phases (average advance: 0.11), just as in our previous modeling work (García et al., 2008). In no case did a home simulation approximate the target phase. When considering the peristaltic mode mixed simulations, changing the synaptic strength profile matched with a given temporal pattern also resulted in both phase advances and delays when compared to the home simulations (rows, Table

1), but no combination of temporal patterns and synaptic strength profiles provided a phase delay large enough to cause the model phase to approximate a given temporal patterns target phase.

As described above for the HE(8) model motor neurons, we compared the phase observed in the home simulations of the HE(12) model motor neuron to their target phases (Table 2). In our previous modeling efforts (García et al., 2008), we found that HE(12) model motor neurons were phase delayed when compared to the living system in the synchronous mode like the HE(8) model motor neurons but similar to the living system in the peristaltic mode.

In the synchronous mode home simulations (diagonals, Table 2), HE(12) model motor neuron phases were delayed in 5/6 home simulations when compared to their target phases (average delay: 0.07), just as in our previous modeling work (García et al., 2008). In those physiological preparations where phase was delayed or near the average phase of the physiological dataset (0.06), home simulation phases were near (within 0.03 phase units) to their target phases (May 19A, May 19B, May 26A and May 27B) with the May 19B home simulation producing a phase advance compared to its target phase (Table 1). In those physiological preparations where phase was advanced when compared to the average phase of the physiological dataset (May 20B and May 22B), home simulation phases were delayed when compared to their target phases.

For the home simulations where the model output approximated the target phase (the May 19A, May 26A and May 27B simulations), mixing the temporal patterns and synaptic strength profiles did not provide a phase advance beyond its target phase. In the home simulation where HE(12) model motor neuron phase was advanced compared to its target (May 19B temporal pattern phase), mixing the temporal patterns and synaptic strength profiles did not provide a phase delay beyond its target phase. In those simulations where a home simulation phase was delayed compared to a target phase (i.e., May 20B and May 22B home simulations), no combination of temporal patterns and synaptic strength profiles provided a phase advance large enough to cause the model phase to approximate a temporal pattern's target phase. In all other cases, the correspondence between the model and target phase was either unaffected or became worse.

In the peristaltic mode home simulations (diagonals, Table 2), HE(12) model motor neurons were phase advanced in 5/6 home simulations when compared to their target phases (average advance: 0.05) and phase delayed in 1 home simulation. 3/6 home simulations, however, produced a phase near to their target phases (the May 19A, May 22B and May 26A home simulations) with the May 22B home simulation producing only a slight phase delay compared to its target phase. The closeness in peristaltic phase between HE(12) model home simulations and their target phases were not observed in the HE(8) model motor neurons.

For the home simulations where the model phase was advanced and approximated a target phase (the May 19A and May 26A simulations), mixing the temporal patterns and synaptic strength profiles did not provide a phase delay beyond the target phase for the May 19A temporal pattern, but did for the May 26A temporal pattern. For the phase delayed May 22B home simulation, mixing the temporal patterns and synaptic strength profiles provided both phase advances and delays when compared to the target phase. In those home simulations in which the home simulation phase was advanced compared to its target phase (the May 19B, May 20B and May 27B home simulations), no combination of temporal pattern and synaptic strength profile provided a phase delay sufficient to approximate the target phase.

Our modeling results suggest that the discrepancies in firing phase observed between the HE(8) model motor neurons and the living systems are not simply due to animal-to-animal variability in the input pattern. In the synchronous mode, when the HE(8) model motor neuron was significantly phase delayed in the home simulations compared to a target phase, no combination of temporal patterns and synaptic strength profiles could promote a phase advance large enough to approximate the target phase. Only when a physiological preparation generated an HE(8) motor neuron phase that was delayed substantially from the average of the living system did a model phase approximate a target phase. In the peristaltic mode, in home simulations, the HE(8) model was phase advanced compared to a target phase and no

combination of temporal pattern and synaptic strength profiles could match a target phase.

In order to resolve the difference in phasing between the HE(8) model motor neurons and the heart motor neurons in the living system, the model motor neurons need to be modified in some way. In the synchronous mode, although the model motor neurons can approximate the target phase, the range of phases where this occurs appears to be restricted to preparations in which we observed HE(8) phases delayed substantially from the average of the living system; therefore, the model motor neurons will need to be modified in such a way as to promote a phase advance by initiating their burst firing in the presence of premotor inhibitory input, as suggested previously (Wright and Calabrese 2011). In the peristaltic mode, part of the required modification to the model motor neurons appears to be the addition of intrinsic properties that allow them to sustain firing at the beginning of premotor inhibitory synaptic input, just like the living motor neurons. Figure 2 shows an intracellular recording from the HE(8) motor neurons along with simultaneous ipsilateral extracellular recordings from the HN(3), HN(4), HN(6) and HN(7) premotor interneurons in the peristaltic mode in the May 22B preparation. The synaptic strength profile measured in this preparation is shown to the right in Figure 2. Note the sizable synaptic conductance provided to the HE(8) motor neuron by the HN(6) and HN(7) interneurons. Although the HN(6) and HN(7) interneurons' synaptic inputs reduced the firing frequency of the motor neuron, it is not until the HN(4) interneuron began to fire that the HE(8) motor neuron stopped firing. The

Fig 3.2. Heart motor neurons in the living system maintain firing in the presence of ongoing inhibition from the premotor heart interneurons. Simultaneous ipsilateral extracellular recordings from the HN(3), HN(4), HN(6) and HN(7) premotor interneurons, along with an intracellular recording from the ipsilateral HE(8) motor neuron for the May 22B preparation. The absolute synaptic strength profile for the HE(8) measured in this preparation is shown to the right. The middle spike is indicated above each HN or HE burst (standard color code of Figure 1, $A_{1\text{-}2}$ is used). The heart motor neuron continues to fire even when its first inputs, the HN(6) and HN(7) interneurons are firing and in spite of the sizable synaptic conductance they produce in the motor neuron. The downward arrow on the intracellular trace indicates the middle spike of the HE(8) ensemble model motor neurons while the vertical line indicates the typical point where the HE(8) model motor neurons tend to stop firing (as measured in phase). The data in this figure are derived from experiments done in Norris et al (2011).

Figure 3.2

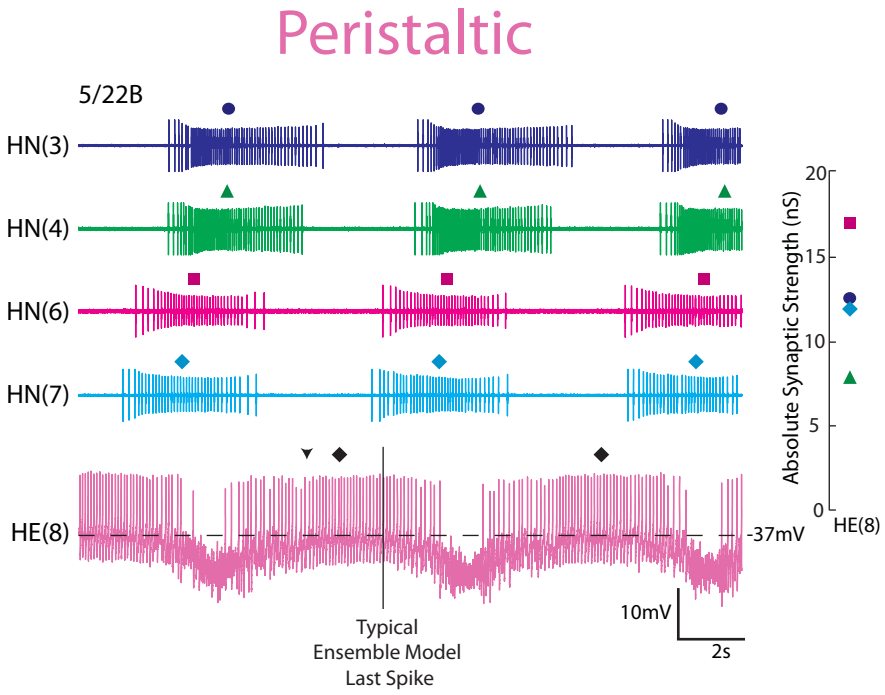
Peristaltic
5/22B
HN(3)
HN(4)
HN(6)
HN(7)
HE(8)
-37mV
10mV
2s
Typical
Ensemble Model
Last Spike
Absolute Synaptic Strength (nS)
20
15
10
5
0
HE(8)

vertical line on the intracellular voltage trace shows where the HE(8) model motor neuron stopped firing in response to the same synaptic input pattern. The ability of living motor neurons to sustain their bursts as premotor inhibitory input begins promotes a phase delay compared to the model motor neurons.

In HE(12) model motor neurons receiving the synchronous input pattern, when the HE(12) model motor neuron was significantly phase delayed in the home simulations compared to the target phase, no combination of temporal patterns and synaptic strength profiles could promote a phase advance large enough to approximate the target, similar to that observed in the HE(8) model motor neurons. In addition, as in the HE(8) model motor neurons, only when a physiological preparation generated an HE(12) motor neuron phase that was delayed substantially from the average of the living system did a model phase approximate the target phase. In fact, in one preparation, May 19B, the phase of the living system was delayed to such an extent (0.16, Table 1) that the home and mixed simulations generate a phase advance compared to the target phase.

In the peristaltic mode, our results suggest that, unlike in the HE(8) model motor neurons, several temporal patterns can, with their own synaptic profiles or in combination with other synaptic strength profiles, produce output similar to that measured in the living system (i.e., the target phase). In 3/6 home simulations, model phase was near (May 19A and May 26A) or phase delayed (May 22B) when compared to the target phase (Table 1). In home simulations where the HE(12) model was phase advanced compared to the target phase, no

combination of temporal pattern and synaptic strength profiles could match the target phase as observed in the HE(8) model motor neurons. These results suggest that, with the standard set of intrinsic properties, the distribution of phases assumed by the HE(12) model motor neurons in the peristaltic mode with the input patterns used has some overlap with the distribution of HE(12) motor neuron phases observed in the living system. This overlap accounts for the models ability to approximate the target phase in the living system. However, in those home simulations where model phase was delayed compared to the target phase, some capacity of the model motor neurons to fire as inhibition begins will no doubt be required to approximate the target phase, as suggested above for the HE(8) motor neurons.

Standard Ensemble Model simulations: Intersegmental Motor Phase Progression

In our study of animal-to-animal variability in the leech heartbeat CPG (Norris et al., 2011), we observed that, in spite of the variability in both temporal patterns and synaptic strength profiles, discernible peristaltic and synchronous motor progressions were observed in every animal, although the sizes of the motor progressions were variable. In that study, we proposed that each animal arrives at its own combination of temporal pattern and synaptic strength profiles in order to generate their stereotyped albeit individual motor patterns. Although

our model motor neurons did not always hit the target segmental phase, we investigated whether our ensemble model would at least produce appropriate peristaltic and synchronous motor progressions between the HE(8) and HE(12) model motor neurons for both modes. For this analysis, we computed the motor progressions across the same home and mixed simulations as above.

To illustrate our procedure, Figure 3 shows the output from model simulations in which the input patterns were derived from the May 19A and May 27B preparations. Iconic representations of the temporal patterns and synaptic strength profiles are shown to the right of the voltage traces. The synaptic strength profiles in these preparations were canonical in their order (i.e., the HN(4) interneuron was the strongest input in the HE(8) motor neurons in these preparations; see Methods) although the total synaptic conductance was larger in the May 27B preparation (note the difference in duty cycle). The synchronous premotor progressions were similar (May 19A: 0.10, May 27B: 0.11), whereas the peristaltic premotor progressions were different between the two input patterns (May 19A: 0.19, May 27B: 0.31). When receiving the May 19A home input pattern the peristaltic motor progression was 0.03, while the synchronous motor progression was -0.04 (the HE(8) leads the HE(12) model motor neuron in phase); when receiving the May 27B home input pattern, the peristaltic motor progression was 0.06 (Fig. 3), while the synchronous motor progression was -0.06. These results indicate that the ensemble model produces appropriate peristaltic and synchronous motor progressions when using these two input patterns.

FIG 3.3. Ensemble model home simulations. Simultaneous bilateral voltage traces from the HE(8) and HE(12) model motor neurons receiving the May19A and May27B input patterns. Dashed line connecting filled diamonds shows the intersegmental peristaltic motor phase progression between the two motor neurons. An iconic representation of the temporal pattern (left) and synaptic strength profiles (right) measured in the living system in those preparations is shown to the right of the voltage traces; standard color code of Figure 1, $A_{1\text{-}2}$ is used. The vertical dashed lines are aligned to the HN(4) interneuron middle spike phase, facilitating a comparison of the temporal patterns (i.e., the premotor progression) of the premotor interneurons measured in these preparations. Large circles represent cell bodies of the HE(8) and HE(12) motor neurons. Sizes of the filled circles show the relative synaptic strengths of the premotor HN interneurons onto the heart motor neurons measured in the living system in those preparations.

Figure 3.3

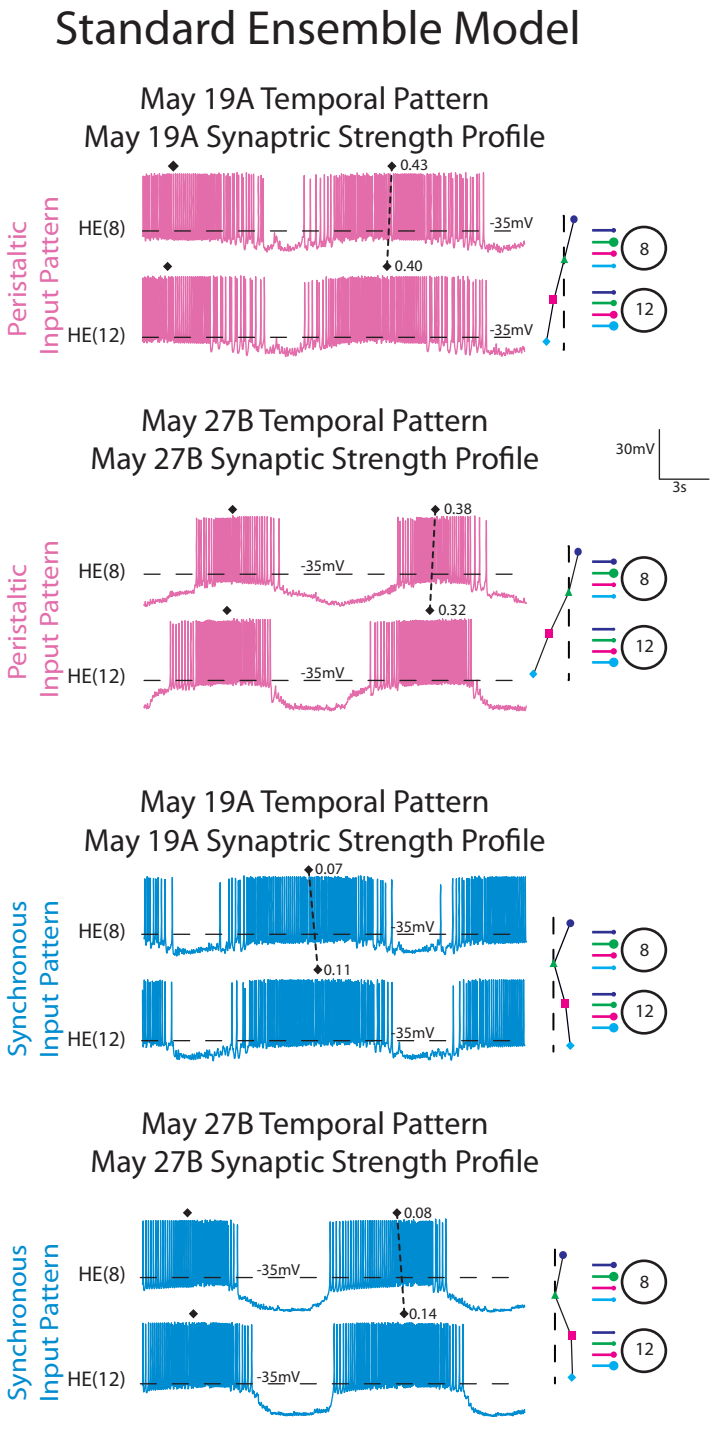
Standard Ensemble Model
May 19A Temporal Pattern
May 19A Synaptic Strength Profile
Peristaltic Input Pattern
HE(8)
HE(12)
0.43
0.40
-35mV
-35mV
8
12
May 27B Temporal Pattern
May 27B Synaptic Strength Profile
30mV
3s
Peristaltic Input Pattern
HE(8)
HE(12)
0.38
0.32
-35mV
-35mV
8
12
May 19A Temporal Pattern
May 19A Synaptic Strength Profile
Synchronous Input Pattern
HE(8)
HE(12)
0.07
0.11
-35mV
-35mV
8
12
May 27B Temporal Pattern
May 27B Synaptic Strength Profile
Synchronous Input Pattern
HE(8)
HE(12)
0.08
0.14
-35mV
-35mV
8
12

Relative Contributions of Temporal Patterns and Synaptic Strength Profiles to Synchronous Motor Progressions: Ensemble Model Simulations

Figure 4 summarizes the synchronous motor progression for all 36 (6 home, 30 mixed) simulations. Each symbol represents a simulation in which a temporal pattern (identified by date) was matched with the synaptic strength profile listed on the horizontal axis. The synaptic strength profiles were ordered in increasing motor progression for home simulations. The synchronous motor progressions observed in the living system are shown on the right side for comparison. The range of these motor progressions represents the biological range for the experiments used as inputs to the standard ensemble model. As can be seen, all combinations of temporal patterns and synaptic strength profiles yield synchronous motor progressions that fall within the range of the physiological dataset, suggesting that, although the segmental phase of both the HE(8) and HE(12) model motor neurons tend to be phase delayed with respect to their target phase, the model generates synchronous motor progressions across temporal patterns and synaptic strength profiles as observed in the living system (Norris et al., 2011). Our simulations predict that, in the synchronous mode, multiple combinations of temporal patterns, regardless of premotor progression and synaptic strength profiles, including profiles with a non-canonical order of their relative synaptic strengths, can produce an appropriate synchronous motor progression.

FIG 3.4. Synchronous motor progressions for the ensemble model when the 6 temporal patterns were matched with each of the 6 synaptic strength profiles. Each symbol (standard color code of Figure 1, $A_{1\text{-}2}$ is used) is the synchronous motor progression between the HE(8) and HE(12) model motor neurons when the temporal pattern (indicated by the appropriate symbol) is matched with the synaptic strength profile indicated on the horizontal axis. The synchronous motor progression measured in the living system for each of the 6 experimental preparations in the physiological dataset is also shown. Synaptic strength profiles are listed in order of decreasing home-simulation (temporal pattern matched with its own synaptic strength profile) synchronous motor progression.

Figure 3.4

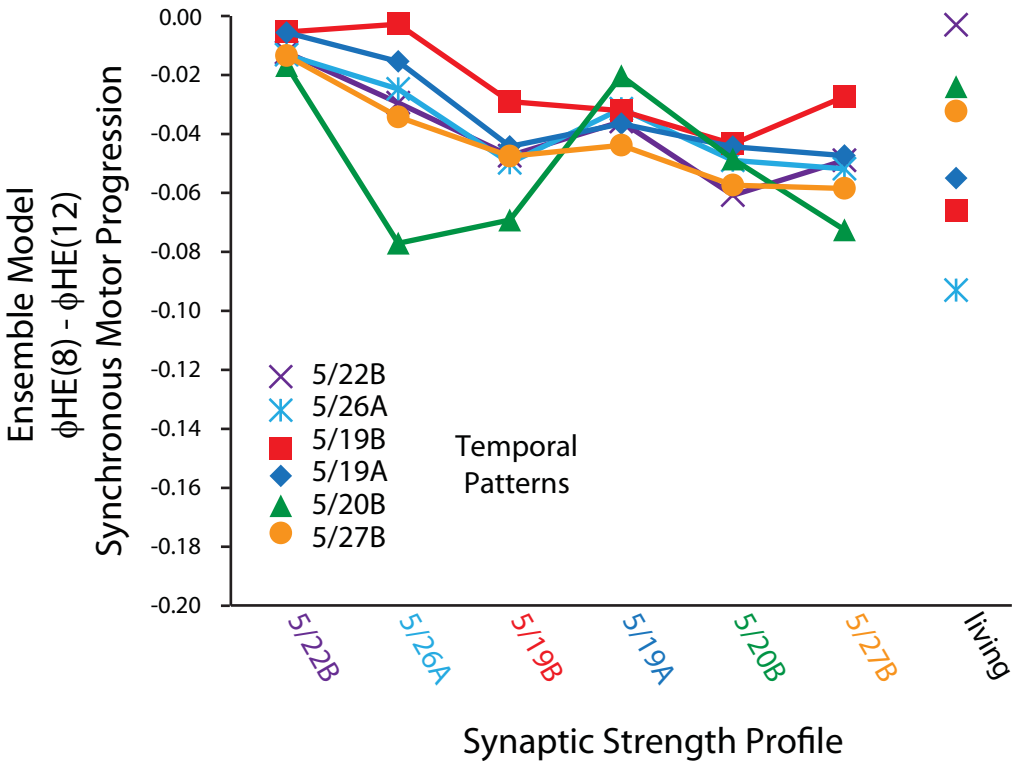
Ensemble Model
ϕHE(8) - ϕHE(12)
Synchronous Motor Progression
0.00
-0.02
-0.04
-0.06
-0.08
-0.10
-0.12
-0.14
-0.16
-0.18
-0.20
5/22B
5/26A
5/19B
5/19A
5/20B
5/27B
Temporal
Patterns
5/22B
5/26A
5/19B
5/19A
5/20B
5/27B
living
Synaptic Strength Profile

Table 3.3 HE(8)-HE(12) model motor phase progressions for home simulations (on diagonal) and mixed simulations (off-diagonal) for the peristaltic (top) and synchronous (bottom) coordination modes.

Table 3.3

Synaptic Strength Profiles

Peristaltic HE(8)-HE12 Phase Difference

Temporal Pattern	may19a	may19b	may20b	may22b	may26a	may27b	living
may19a	**0.02**	0.06	0.06	0.01	0.03	0.04	0.07
may19b	0.02	**0.04**	0.04	0.05	0.04	0.05	0.08
may20b	0.04	0.05	**0.07**	0.01	0.05	0.04	0.10
may22b	0.04	0.05	0.08	**0.02**	0.05	0.05	0.11
may26a	0.03	0.08	0.09	0.01	**0.08**	0.05	0.15
may27b	0.06	0.05	0.10	0.03	0.07	**0.06**	0.18

Synchronous HE(8)-HE12 Phase Difference

Temporal Pattern	may19a	may19b	may20b	may22b	may26a	may27b	living
may19a	**-0.04**	-0.04	-0.04	-0.01	-0.02	-0.05	-0.06
may19b	-0.03	**-0.03**	-0.04	-0.01	0.00	-0.03	-0.07
may20b	-0.02	-0.07	**-0.05**	-0.02	-0.08	-0.07	-0.02
may22b	-0.04	-0.05	-0.06	**-0.01**	-0.03	-0.05	-0.00
may26a	-0.03	-0.05	-0.05	-0.01	**-0.02**	-0.05	-0.09
may27b	-0.04	-0.05	-0.06	-0.01	-0.03	**-0.06**	-0.03

Relative Contributions of Temporal Patterns and Synaptic Strength Profiles to Synchronous Motor Progressions: Hybrid System Experiments

Because the model motor neurons contained a minimal set of intrinsic electrical properties (García et al., 2008), we wanted to test our modeling prediction that, in the synchronous mode, multiple temporal patterns and synaptic strength profiles can generate a synchronous motor progression in living heart motor neurons, i.e., in the presence of their actual intrinsic properties. We extracted the synaptic conductance waveforms generated from three of the model simulations (and a special pattern described below) and used them as inputs in dynamic-clamp experiments (Fig. 5A). We used the HE(8) and HE(12) peristaltic and synchronous synaptic conductance waveforms from the following ensemble model simulations: 1) the May 19A home simulation (A_1), 2) the May 27B home simulation (A_2), 3) the May 27B temporal pattern matched with the non-canonical May 22B synaptic strength profile (A_3), and we added a fourth pattern 4) the May 27B temporal pattern matched with an inverted May 27B synaptic strength profile (A_4; described below). Each of these waveforms was introduced to the same bilateral pair of motor neurons (i.e., one received the synchronous and the other received the peristaltic waveform) in a given experiment (n = 6). We then calculated the phase of the motor neurons for each synchronous waveform and computed the synchronous motor progression. The same experiments were used for a corresponding analysis of the peristaltic waveforms

Table 3.1 HE(8) model motor neuron phase for home simulations (on diagonal) and mixed simulations (off-diagonal) for the peristaltic (top) and synchronous (bottom) coordination modes.

Table 3.1

Synaptic Strength Profiles								
Peristaltic HE(8)								
		may19a	may19b	may20b	may22b	may26a	may27b	living
Temporal Pattern	may19a	**0.43**	0.41	0.43	0.39	0.39	0.41	0.49
	may19b	0.43	**0.41**	0.44	0.46	0.40	0.46	0.56
	may20b	0.39	0.37	**0.39**	0.37	0.37	0.39	0.47
	may22b	0.38	0.35	0.38	**0.36**	0.34	0.37	0.43
	may26a	0.33	0.33	0.35	0.32	**0.31**	0.33	0.41
	may27b	0.39	0.34	0.39	0.38	0.35	**0.38**	0.57
Synchronous HE(8)								
		may19a	may19b	may20b	may22b	may26a	may27b	living
Temporal Pattern	may19a	**0.07**	0.09	0.09	0.13	0.11	0.10	0.04
	may19b	0.09	**0.10**	0.09	0.14	0.13	0.12	0.09
	may20b	0.07	0.06	**0.07**	0.08	0.07	0.06	0.96
	may22b	0.07	0.08	0.07	**0.11**	0.10	0.09	0.97
	may26a	0.05	0.05	0.05	0.07	**0.07**	0.05	0.96
	may27b	0.06	0.08	0.07	0.10	0.10	**0.08**	0.07

– see below. In agreement with our modeling results, there was no difference in the average synchronous motor progression between input waveforms derived from the May 19A home simulation, from the May27B home simulation and from the May 27B temporal pattern matched with the May 22B synaptic strength profile (Fig. 5B; One-Way Repeated Measures ANOVA, $p>0.05$).

To test the contribution of the synaptic strength profile to the synchronous motor progression, we inverted the synaptic strength profile for the May 27B input pattern by exchanging the synaptic conductance arising from the HN(4) interneuron measured in the HE(8) motor neuron (that segment's strongest input) with the synaptic conductance arising from the HN(7) interneuron in the HE(8) motor neuron (that segment's weakest input). We also exchanged the synaptic conductances associated with the HN(6) and HN(3) interneurons in this segment. This manipulation made the relatively weak HN(7) interneuron input the strongest in the HE(8) model motor neuron, while making the strong HN(4) interneuron input the weakest. In the HE(12) model motor neuron, we inverted that segment's synaptic strength profile by making the strong HN(7) interneuron input in that segment the weakest and made the weaker HN(4) input the strongest (see Methods). These inverted synaptic strength profiles were then matched with the May 27B temporal pattern. When this conductance waveform was introduced to the HE(8) and HE(12) model motor neurons, a large, positive phase progression (0.06) was produced that was significantly different from the other combinations of temporal patterns and synaptic strength profiles (Fig. 5B; One-Way Repeated Measures ANOVA, $p < 0.05$). This positive phase

FIG 3.5. The response of heart motor neurons in segments 8 and 12 in the dynamic clamp receiving synaptic conductance waveforms extracted from ensemble model simulations. *A*: Intracellular recordings and synaptic conductances g_{Syn} of the HE(8) and HE(12) motor neurons receiving the synchronous May 19A temporal and synaptic strength profile (A_1), May 27B temporal pattern and synaptic strength profile (*A2*), the May 27B temporal pattern matched with the May 22B synaptic strength profile (*A3*) and the inverted May27B synaptic strength profile (*A4*) are shown. An iconic representation of the temporal pattern (left panel) and the synaptic strength profile (right panel) are shown to the right of the voltage trace; standard color code of Figure 1, $A_{1\text{-}2}$ is used. The vertical dashed lines are aligned to the HN(4) interneuron middle spike phase, facilitating a comparison of the temporal patterns of the premotor interneurons measured in these preparations. Large circles represent cell bodies of the HE(8) and HE(12) motor neurons. Sizes of the filled circles show the relative synaptic strengths of the premotor HN interneurons onto the heart motor neurons measured in the living system on those days. *B*. Average ($\pm$ sd, n = 6) synchronous motor progression of the heart motor neurons from experiments described in panel *A*. Brackets represent the statistical comparison of the May 27B temporal pattern matched with the May 27B inverted synaptic strength profile to the other input waveforms. Asterisk indicates a significant difference in motor progression between the May 27B temporal pattern matched with the inverted May 27B synaptic strength profile waveform and the other input patterns (One-Way Repeated Measures ANOVA, $p < 0.05$).

Figure 3.5

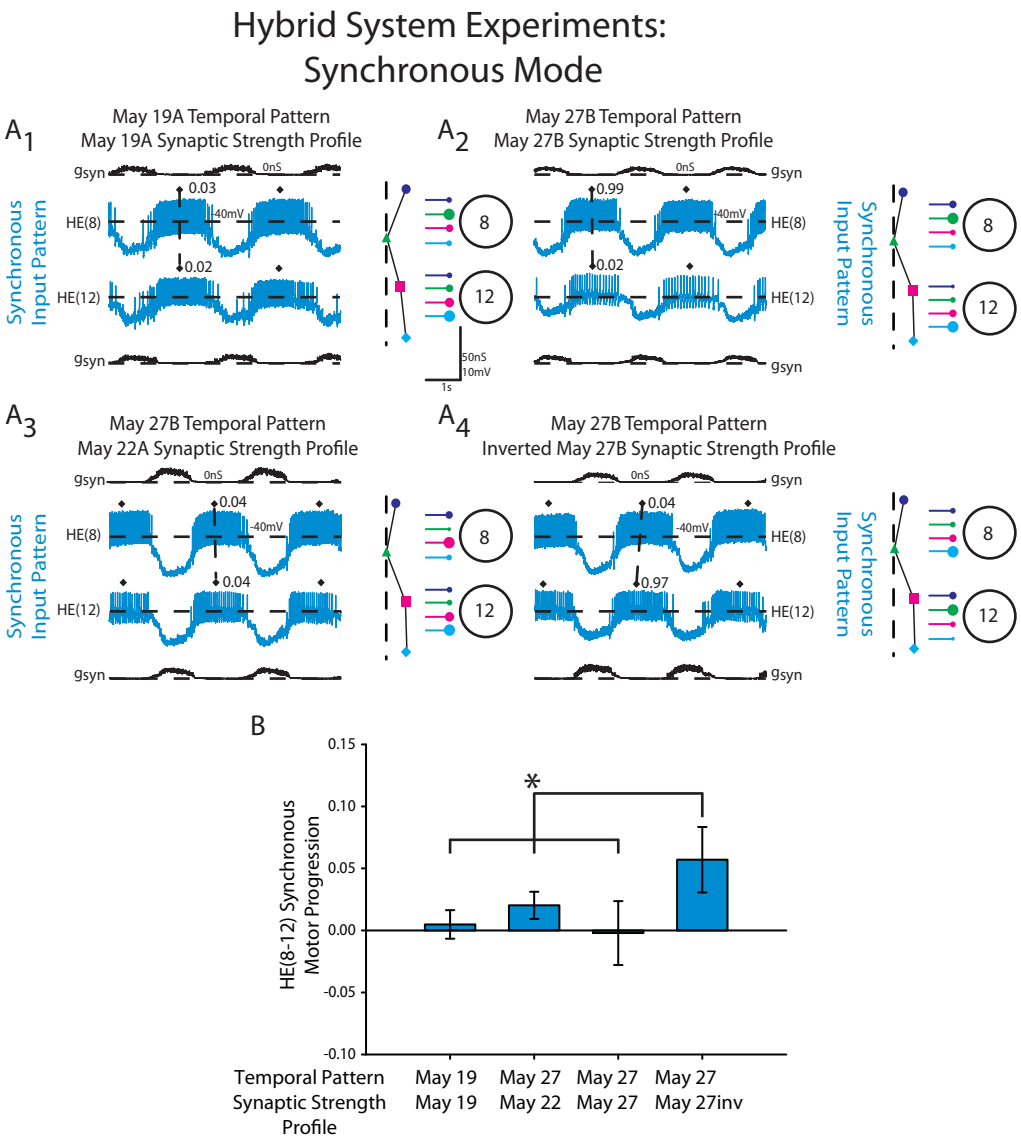
Hybrid System Experiments:
Synchronous Mode
A1
May 19A Temporal Pattern
May 19A Synaptic Strength Profile
A2
May 27B Temporal Pattern
May 27B Synaptic Strength Profile
A3
May 27B Temporal Pattern
May 22A Synaptic Strength Profile
A4
May 27B Temporal Pattern
Inverted May 27B Synaptic Strength Profile
Synchronous Input Pattern
HE(8)
HE(12)
gsyn
0nS
-40mV
0.03
0.02
0.99
0.04
0.97
8
12
50nS
10mV
1s
B
HE(8-12) Synchronous Motor Progression
0.15
0.10
0.05
0.00
-0.05
-0.10
*
Temporal Pattern
Synaptic Strength Profile
May 19
May 19
May 27
May 22
May 27
May 27
May 27
May 27inv

progression, produced with a synchronous temporal pattern, is similar to what is normally observed in the peristaltic mode in the living system, and was confirmed in a corresponding ensemble model simulation (data not shown).

These results suggest that, in the living system, multiple combinations of temporal patterns and synaptic strength profiles can generate an appropriate synchronous motor progression. We attribute this to the fact that the premotor inputs arise nearly synchronously; therefore, synaptic strength profiles may vary in their canonical order and still produce an appropriate synchronous motor progression. However, although non-canonical synaptic strength profiles observed in the living system do not strongly alter synchronous motor progression in the living system there are synaptic strength profiles (albeit artificial ones) that can overwhelm the synchronous premotor temporal pattern and result in a non-functional motor progression.

Relative Contributions of Temporal Patterns and Synaptic Strength Profiles to Peristaltic Motor Progressions: Ensemble Model Simulations

Figure 6 summarizes the peristaltic motor progressions across all model simulations (6 home; 30 mixed). Data are organized as in Figure 4. Across synaptic strength profiles, the May 19A temporal pattern generated, on average, the smallest peristaltic motor progressions (average = 0.04) across synaptic

Table 3.2 HE(12) model motor neuron phase for home simulations (on diagonal) and mixed simulations (off-diagonal) for the peristaltic (top) and synchronous (bottom) coordination modes.

Table 3.2

Synaptic Strength Profiles								
Peristaltic HE(12)								
		may19a	may19b	may20b	may22b	may26a	may27b	living
Temporal Pattern	may19a	**0.40**	0.35	0.37	0.38	0.36	0.37	0.43
	may19b	0.41	**0.37**	0.40	0.41	0.36	0.41	0.48
	may20b	0.36	0.32	**0.32**	0.37	0.32	0.35	0.37
	may22b	0.33	0.30	0.30	**0.34**	0.29	0.32	0.32
	may26a	0.30	0.25	0.27	0.30	**0.23**	0.27	0.26
	may27b	0.33	0.30	0.29	0.35	0.28	**0.32**	0.39
Synchronous HE(12)								
		may19a	may19b	may20b	may22b	may26a	may27b	living
Temporal Pattern	may19a	**0.11**	0.14	0.13	0.13	0.13	0.14	0.10
	may19b	0.12	**0.13**	0.13	0.15	0.13	0.15	0.16
	may20b	0.09	0.13	**0.12**	0.10	0.15	0.13	0.98
	may22b	0.11	0.13	0.13	**0.12**	0.13	0.14	0.97
	may26a	0.08	0.10	0.10	0.09	**0.10**	0.11	0.06
	may27b	0.11	0.13	0.12	0.12	0.13	**0.14**	0.10

strength profiles. The May 27B temporal pattern generated, on average, the largest peristaltic motor progressions (average = 0.06) across synaptic strength profiles. The synaptic strength profiles in both of these preparations are canonical in their order; their premotor progressions, however, were different: 0.19 for May 19A vs. 0.31 for the May 27B preparation. Across temporal patterns, the May 22B synaptic strength profile generated, on average, the smallest peristaltic motor progression (average = 0.02) whereas the May 20B synaptic strength profile generated, on average, the largest peristaltic motor progression (average = 0.07). The premotor progression for these two preparations was similar: 0.21 for May 20B vs. 0.19 for May 22B; the synaptic strength profiles, however, were different: the May 20B was canonical in its order, whereas the May 22B preparation was non-canonical in its order.

Comparing home simulation results, the May 26A home simulation generated the largest motor progression (Fig. 6). The synaptic strength profile for this input pattern was also non-canonical in its order. However, the premotor progression for the May 26A preparation was the largest in the dataset (0.32). To assess whether or not the May 26A temporal pattern could produce a larger peristaltic motor progression with a canonical synaptic strength profile, we compared the May 26A home simulation to that one in which the May 26A temporal pattern was matched with the canonical synaptic strength profile of May 20B. When matched with a canonical synaptic strength profile, the May 26A temporal pattern generated a larger motor progression (0.09 vs. 0.08) than with the non-canonical May26A home synaptic strength profile (Fig. 6).

FIG 3.6. Peristaltic motor phase progression in the ensemble model when the 6 temporal patterns were matched with each of the 6 synaptic strength profiles. Each symbol (standard color code of Figure 1, $A_{1\text{-}2}$ is used) is the peristaltic motor phase progression between the HE(8) and HE(12) model motor neurons when the temporal pattern (indicated by the appropriate symbol) is matched with the synaptic strength profile indicated on the horizontal axis. The peristaltic motor phase progression measured in the living system for each of the 6 experimental preparations in the physiological dataset is also shown. Synaptic strength profiles are listed in order of increasing home-simulation (temporal pattern matched with its own synaptic strength profile) peristaltic motor phase progression.

Figure 3.6

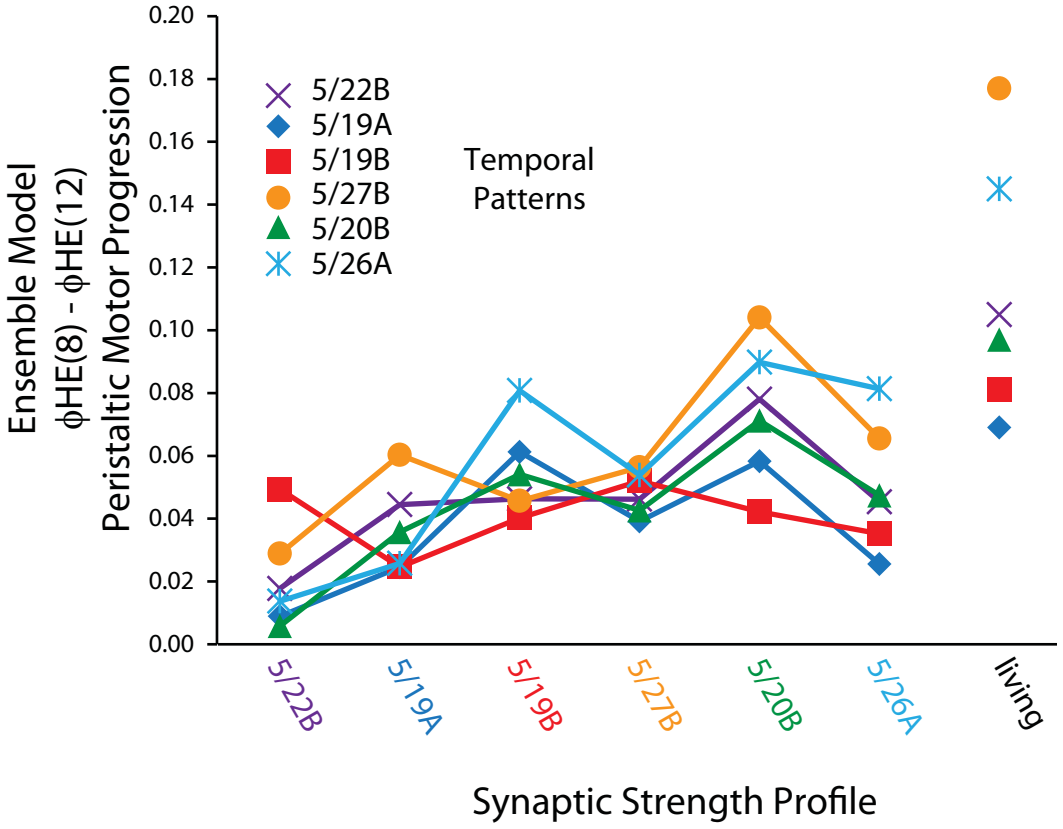
Ensemble Model
ϕHE(8) - ϕHE(12)
Peristaltic Motor Progression
0.20
0.18
0.16
0.14
0.12
0.10
0.08
0.06
0.04
0.02
0.00
5/22B
5/19A
5/19B
5/27B
5/20B
5/26A
Temporal
Patterns
5/22B
5/19A
5/19B
5/27B
5/20B
5/26A
living
Synaptic Strength Profile

Taken together, these results predict that input patterns with larger peristaltic premotor progressions generate larger peristaltic motor progressions than input patterns with smaller premotor progressions. Furthermore, our modeling results predict that synaptic strength profiles that are canonical in their order will generate larger peristaltic motor progressions than non-canonical synaptic strength profiles when matched with the same premotor progression.

Relative Contributions of Temporal Patterns and Synaptic Strength Profiles to Peristaltic Motor Progressions: Hybrid System Experiments

Again, we used the dynamic clamp to test the prediction of our modeling experiments that the larger premotor progressions and canonical strength profiles generate larger peristaltic motor progressions in the heart motor neurons in the living system. For this analysis, we used the data for the peristaltic synaptic conductance waveforms introduced into the motor neurons in the experiments of Figure 5 ($A_{1\text{-}4}$, Fig. 7). Although considered separately, the data for Figure 5 and 7 are thus derived from the same experiment. Our comparisons of interest were those highlighted in the modeling results above: 1) between the May 19A home and May 27B home waveforms and 2) between the May 27B home waveform and the May 27B temporal pattern matched with the non-canonical May 22B synaptic strength profile.

There was a significant difference in the peristaltic motor progression across all the input waveforms (Fig. 7B; One-Way repeated measures ANOVA). In follow-up comparisons, the May 27B home waveform generated a larger peristaltic motor progression than the May 19A home waveform (paired *t*-test, $p < 0.05$). Because the synaptic strength profiles for these two preparations were canonical in their order, we treated this as a test of the prediction that a larger premotor progression generates a large motor progression.

The peristaltic motor progression generated by the May 27B home waveform was significantly greater than that generated by the mixed waveform consisting of the May 27B temporal pattern matched with the non-canonical May 22B synaptic strength profile (paired *t*-test, $p < 0.05$). Because both synaptic strength profiles were matched with the same temporal pattern, we treated this as a test of the hypothesis that canonical synaptic strength profiles generate larger motor progressions than non-canonical synaptic strength profiles.

We also assessed how an inverted synaptic strength profile would affect the peristaltic motor progression. When the conductance waveform derived from the May 27B temporal pattern with an inverted synaptic strength profile (A_4, Fig. 7) was introduced to the HE(8) and HE(12) motor neurons, it generated a negative phase progression (-0.03) that was significantly different from the other combinations of temporal patterns and synaptic strength profiles (Fig. 5B; One-Way Repeated Measures ANOVA, $p < 0.05$). The same negative motor progression was confirmed in a corresponding simulation in the ensemble model

FIG 3.7. The response of heart motor neurons in segments 8 and 12 in the dynamic clamp receiving synaptic conductance waveforms extracted from ensemble model simulations. *A*: Intracellular recordings and synaptic conductances g_{Syn} of the HE(8) and HE(12) motor neurons receiving the peristaltic May 19A temporal and synaptic strength profile (A_1), May 27B temporal pattern and synaptic strength profile (A_2), the May 27B temporal pattern matched with the May 22B synaptic strength profile (A_3) and the inverted May27B synaptic strength profile (A_4) are shown. An iconic representation of the temporal pattern (left panel) and the synaptic strength profile (right panel) are shown to the right of the voltage trace; standard color code of Figure 1, $A_{1\text{-}2}$ is used. The vertical dashed lines are aligned to the HN(4) interneuron middle spike phase, facilitating a comparison of the temporal patterns of the premotor interneurons measured in these preparations. Large circles represent cell bodies of the HE(8) and HE(12) motor neurons. Sizes of the filled circles show the relative synaptic strengths of the premotor HN interneurons onto the heart motor neurons measured in the living system on those days. *B*. Average ($\pm$ sd, n = 6) peristaltic motor progression of the heart motor neurons from experiments described in panel *A*. Brackets represent the statistical comparison of the May 27B temporal pattern matched with the May 27B synaptic strength profile to the May 19A temporal pattern matched with the May 19A synaptic strength profile and the May 27B temporal pattern matched with the non-canonical May 22B synaptic strength profile. Asterisks indicate significant differences in the peristaltic motor progression between the May 27B home simulation and both

the May 19A home simulation and May 27B temporal pattern matched with the May 22B synaptic strength profile (Paired t-test, $p < 0.05$).

Figure 3.7

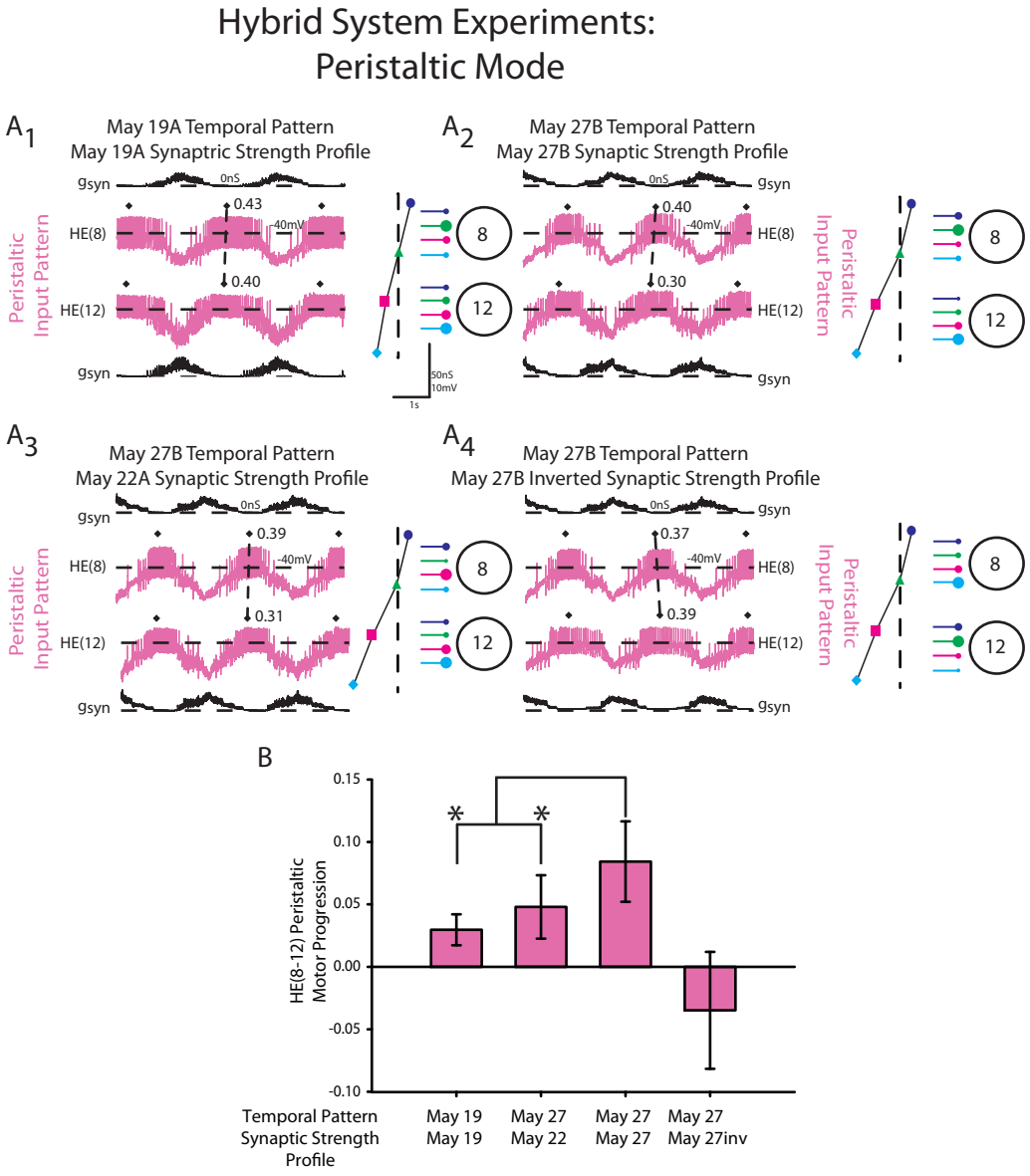
Hybrid System Experiments:
Peristaltic Mode
A1
May 19A Temporal Pattern
May 19A Synaptric Strength Profile
A2
May 27B Temporal Pattern
May 27B Synaptic Strength Profile
A3
May 27B Temporal Pattern
May 22A Synaptic Strength Profile
A4
May 27B Temporal Pattern
May 27B Inverted Synaptic Strength Profile
Peristaltic Input Pattern
gsyn
0nS
HE(8)
HE(12)
-40mV
0.43
0.40
0.39
0.31
0.37
0.30
8
12
50nS
10mV
1s
B
HE(8-12) Peristaltic Motor Progression
0.15
0.10
0.05
0.00
-0.05
-0.10
*
*
Temporal Pattern
Synaptic Strength Profile
May 19
May 19
May 27
May 22
May 27
May 27
May 27
May 27inv

(data not shown). Despite the fact that the temporal pattern had a positive premotor progression, this inverted synaptic conductance waveform produced a negative motor progression, similar to that observed in the synchronous mode in the living system. This result suggests that, in addition to significantly affecting the motor progression observed in the peristaltic mode, a non-canonical synaptic strength profile (albeit an artificial one) can overwhelm a temporal pattern with a large peristaltic premotor progression and result in a non-functional motor progression.

Synaptic Strength Index as Predictor of Peristaltic Motor Progression in Motor Neuron Ensemble Simulations

In our previous work (Norris et al, 2011), we showed that there were very few significant correlations between the relative synaptic strength of an individual premotor input and HE(8) or HE(12) heart motor neuron phase in the living system. We attributed this lack of correlation to the fact that animal-to-animal variability in the relative strength of each premotor input and in the temporal pattern of the inputs masked relatively straightforward correlations such as those observed in the stomatogastric nervous system (Goalliard et al 2009). Indeed, in follow up simulations in which we fixed the temporal pattern and synaptic strength of three of the premotor interneuron inputs and varied the fourth across the range of synaptic strengths observed in the 12 fully

characterized living preparations (Norris et al 2011), strong and significant correlations were observed. In our 6 home simulations, we also did not find correlations between any one input and the phase of an individual motor neuron or the peristaltic motor progression, suggesting that, as in the living system, the animal-to-animal variability in temporal patterns and synaptic strength of the 4 inputs obscures simple correlations in the ensemble model.

We then attempted to identify a metric that would capture the effectiveness of the synaptic strength profiles in segments 8 and 12 in promoting a large peristaltic motor progression. We developed a metric we called the synaptic strength index (SSI; see Methods) that represents the summed disparity in strength of the HN(4) and HN(7) premotor inputs in segments 8 (where the HN(4)/HN(7) input is strongest/weakest) and 12 (where the HN(7)/HN(4) input is the strongest/weakest). We then correlated this value to the peristaltic motor progression of the 6 home simulations (Fig. 8A) and the mixed simulations in which the peristaltic motor progression is averaged across the 6 temporal patterns (Fig. 8B). In both cases, a significant amount of variability in the peristaltic motor progression was explained by its regression on the SSI (home simulations: $R^2 = 0.90$, $F = 15.73$, $df = 1$, $p < 0.05$; average across temporal patterns: $R^2 = 0.80$, $F = 37.57$, $df = 1$, $p < 0.05$). These results suggests that, in the model and in the hybrid system, the stronger the HN(4) interneuron input in the HE(8) motor neuron and, simultaneously, the HN(7) interneuron input in the HE (12) motor neuron, the larger the peristaltic motor progression will be. When the SSI was correlated to the 6 preparations in the physiological dataset, no

FIG 3.8. Correlation between the synaptic strength index (SSI; see Methods) and the peristaltic motor phase progression for both the ensemble model home simulations (*A*) and from the average peristaltic motor progression for a given synaptic strength profile across temporal patterns from the mix-and match simulations (*B*). The downward arrow in 8A indicates the SSI value at which the peristaltic motor progression changes sign and the motor progression no longer resembles a true peristaltic progression between the HE(8) and the HE(12) motor neurons.

Figure 3.8

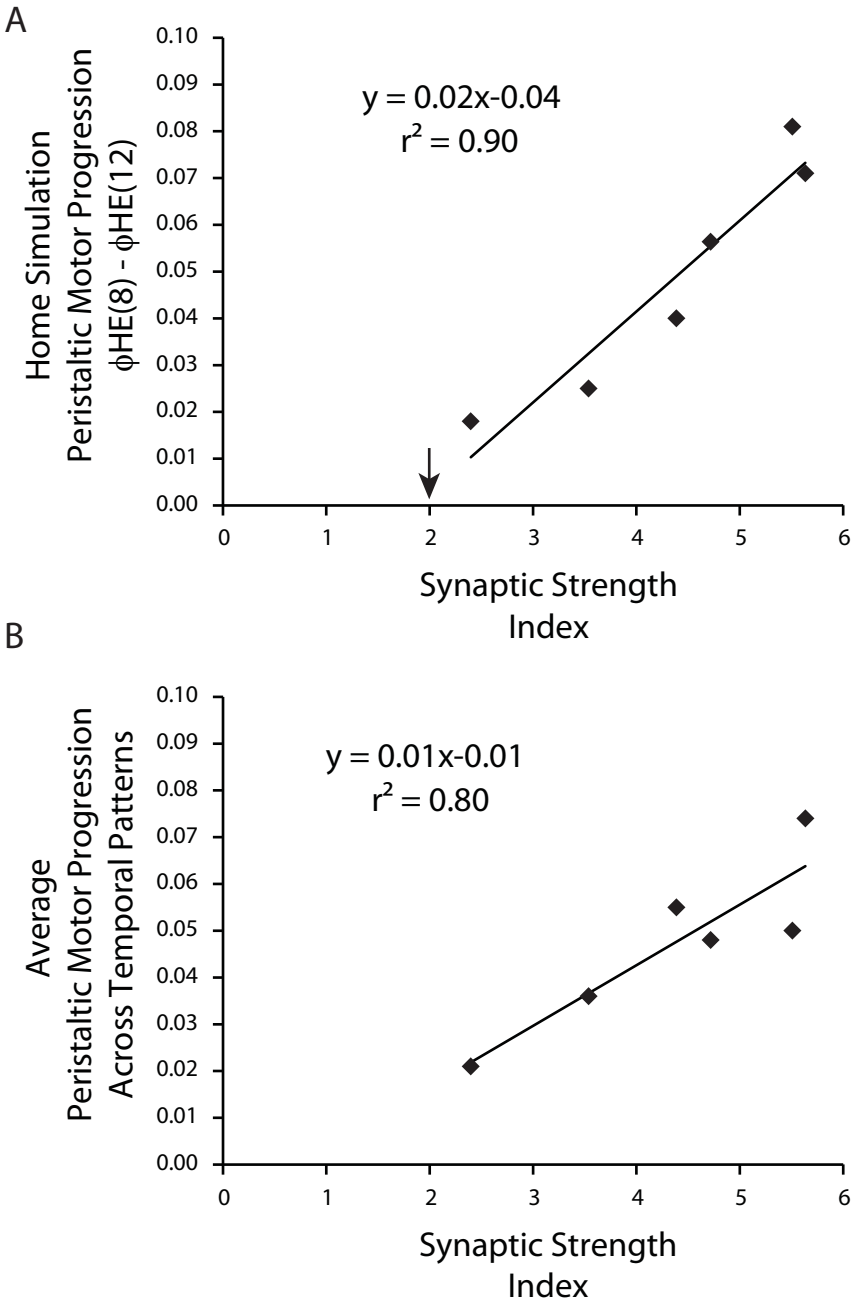
A
Home Simulation
Peristaltic Motor Progression
ϕHE(8) - ϕHE(12)
y = 0.02x-0.04
r2 = 0.90
0.10
0.09
0.08
0.07
0.06
0.05
0.04
0.03
0.02
0.01
0.00
0
1
2
3
4
5
6
Synaptic Strength
Index
B
Average
Peristaltic Motor Progression
Across Temporal Patterns
y = 0.01x-0.01
r2 = 0.80
0.10
0.09
0.08
0.07
0.06
0.05
0.04
0.03
0.02
0.01
0.00
0
1
2
3
4
5
6
Synaptic Strength
Index

correlation was found ($R^2 = 0.12$, $p > 0.05$). We attribute this lack of correlation to animal-to-animal variability, including variability in the intrinsic electrical properties of the HE motor neurons.

In addition to predicting how large a peristaltic motor progression can be, the SSI can also estimate how non-canonical a synaptic strength profile can be before it overwhelms the potential peristaltic motor progression provided by the temporal pattern and produces a negative peristaltic motor progression, as in the dynamic-clamp experiments of Figure 7. In the home simulations, the x-intercept (downward arrow, Fig. 8A) represents the SSI where the peristaltic motor progression reverses sign. This value is 2.0 in the home simulations, and is compatible with synaptic strength profiles in which the HN(4) and HN(7) interneuron inputs are equal in strength in both the HE(8) and HE(12) motor neurons. In the physiological dataset, the May 22B preparation had the smallest SSI (2.40) while the May 20B preparation had the largest SSI (5.63), thus explaining their ability to affect the peristaltic motor progression realized by any temporal pattern with which they were matched. The SSI for the May 27B inverted synaptic strength profile, on the other hand, was 0.86, thus the negative peristaltic motor progression in our modeling and hybrid system experiments. Taken together, these results suggest that, for a given temporal pattern, higher SSI values will result in larger peristaltic motor progressions than smaller SSI values.

DISCUSSION

The goal of the present study was to determine the relative contributions of the temporal pattern and synaptic strength profiles of premotor inputs to rhythmic motor output. We used the leech heartbeat CPG, a system in which we can measure both timing of activity in premotor interneurons (temporal pattern) and patterns of their synaptic strengths onto motor neurons (synaptic strength profiles) in individuals to address this goal. The heartbeat CPG produces a bilaterally asymmetric pattern of activity in which premotor interneurons on one side produce a rear-to-front (peristaltic) progression, and a nearly synchronous (synchronous) progression on the other side. These premotor patterns are elaborated, via chemical inhibitory synapses, into a pattern of synaptic drive onto heart motor neurons that results in a bilaterally asymmetric fictive motor pattern like that of the premotor interneurons. We focused on two pairs of heart motor neurons (i.e., in mid-body segments 8 and 12) in which we can account for all of the premotor inputs these motor neurons receive and which express motor progressions large enough to capture the peristaltic and synchronous motor patterns. In a previous study (Norris et al, 2011) we quantified animal-to-animal variability in all levels of the system: premotor progressions, synaptic strength profiles and motor progressions. In spite of the considerable variability in these components of the system, all preparations had discernible peristaltic and synchronous patterns of activity. We concluded that each animal arrives at a unique combination of temporal pattern and synaptic strength profiles such that peristaltic and synchronous patterns were always expressed. Here we used 6

preparations in which temporal patterns, synaptic strength profiles and motor patterns were quantified in order to ascertain what rules govern how an individual animal arrives at its unique solution of temporal pattern and synaptic strength profiles to produce the appropriate peristaltic and synchronous motor patterns.

In the synchronous mode, our major finding is that many different combinations of temporal patterns and synaptic strength profiles can interact to produce an appropriate synchronous motor pattern. In both our modeling and hybrid system experiments, we observed that synchronous motor progressions could be produced with different combinations of temporal patterns and synaptic strength profiles. It was only when we used an artificially inverted synaptic strength profile that we observed dramatic departures from the synchronous motor progression. We attribute the ability of multiple combinations of temporal patterns and synaptic strength profiles to produce synchronous motor progressions to the near synchronous premotor temporal patterns that the nervous system produces, so that differences in variability of synaptic strength profiles matter little.

In the peristaltic mode, Figure 9 summarizes our data and our working model for how temporal patterns and synaptic strength profiles combine to produce peristaltic motor progressions. Our data show that temporal patterns with a large premotor progression promote larger motor progressions (Fig. 9*A*). For example, as shown in our dynamic-clamp experiments, the May 27B

temporal pattern produced, on average, larger peristaltic motor progressions than the May 19A temporal pattern.

Moreover, our data show that canonical synaptic strength profiles promote larger motor progressions than non-canonical synaptic strength profiles (Fig. 9*B,C*). This effect of the synaptic strength profile on peristaltic motor phase progression is manifested in the following manner. In segment 8, a canonical synaptic strength profile is one in which the HN(4) interneuron provides the strongest synaptic input, with the HN(7) being weakest. Assuming a fixed phase of the HE(12) motor neuron in this scenario, a canonical synaptic strength profile would allow the HE(8) motor neuron (Fig. 9*B*, left synaptic strength profile) to fire through the weaker inhibition from the HN(7) interneuron (note that this is the first input that the motor neurons receive in the peristaltic mode); as the HN(4) interneuron begins to fire, it is most effective at silencing the HE(8) motor neuron (dark shaded HE(8) phase box). The ability to fire through the weak inhibition from the HN(7) interneuron would promote a phase delay of the HE(8) motor neuron, increasing the peristaltic motor progression. If the relative strength of the HN(6) and HN(7) interneurons were to increase, however, in the HE(8) motor neuron (Fig 9*B*, right synaptic strength profile), it would confer upon them a greater ability to terminate the HE(8) motor neuron burst, which then would occur earlier than with a canonical synaptic strength profile. This profile would advance the phase of the HE(8) motor neuron (Fig 9*B*, light shaded HE(8) phase box), decreasing the peristaltic motor progression.

FIG 3.9. Proposed model for establishing peristaltic motor progression in the leech heartbeat system. Panels *A*-*C* are schematized hemi-lateral phase diagrams. Each boxplot represents the first (left edge) last (right edge) and middle (middle line) spike phase for the appropriate premotor interneuron (colored boxes; standard color code of Figure 1, $A_{1\text{-}2}$ is used) and heart motor neurons (grey boxes). Boxplots illustrate the typical firing pattern observed in the living system and are not based on actual data. *A*: Effect of temporal pattern on the peristaltic motor phase progression. *B*: Effect of synaptic strength profile in HE(8) motor neurons on peristaltic motor phase progression. The phase of the HE(8) motor neuron is flexible; the phase of the HE(12) is fixed in this scenario. Shading of the premotor interneuron boxes illustrates the relative synaptic strengths of these inputs on to the heart motor neurons; the graph to the right illustrates the canonical (left) vs. non-canonical synaptic strength profiles for the HE(8) motor neuron. Dark shaded motor neuron phase box represents HE(8) motor neuron phase when considering the canonical synaptic strength profile; the light shaded phase box represents the HE(8) motor neuron phase when considering the non-canonical synaptic strength profile. *C*: Effect of synaptic strength profile in HE(12) motor neurons on peristaltic motor phase progression. The phase of the HE(12) motor neuron is flexible; the phase of the HE(8) is fixed in this scenario. Shading of the premotor interneuron boxes illustrates the relative synaptic strengths of these inputs to the heart motor neurons; the graph to the right illustrates the canonical (left) vs. non-canonical synaptic strength profiles for the HE(12) motor neuron. Dark shaded motor neuron phase box represents HE(12) motor neuron phase when considering the canonical synaptic

strength profile; the light shaded phase box represents the HE(12) motor neuron phase when considering the non-canonical synaptic strength profile.

Figure 3.9

A Temporal Pattern: Larger Premotor Progressions Promotes Larger Peristaltic Motor Progressions

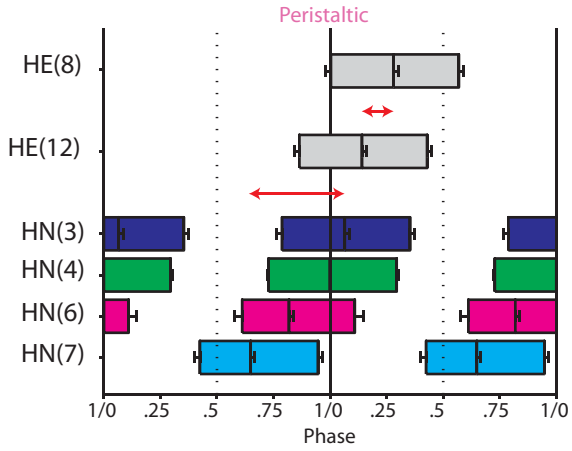

B HE(8) Synaptic Strength Profile: Stronger Synaptic Inputs From Front Premotor Interneurons Promotes Larger Peristaltic Motor Progressions

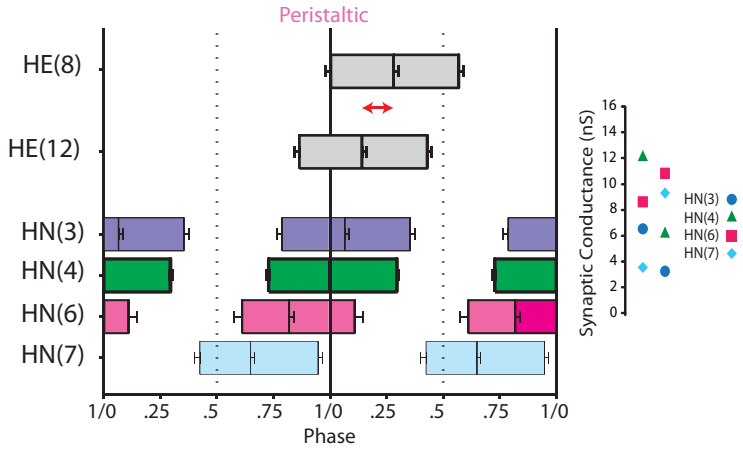

HE(12) Synaptic Strength Profile: Stronger Synaptic Inputs From Rear Premotor Interneurons Promotes Larger Peristaltic Motor Progressions

C

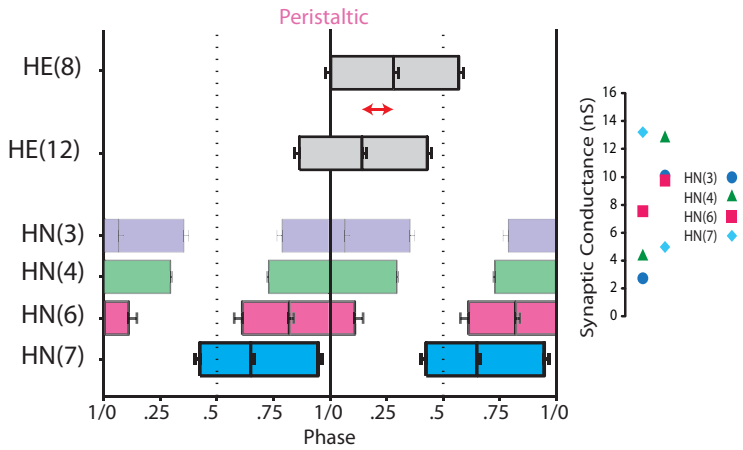

In the HE(12) motor neuron, a canonical synaptic strength profile is one in which the HN(7) interneuron provides the strongest synaptic input, with the HN(4) interneuron being weakest (Fig 9*C*, left synaptic strength profile). Assuming a fixed phase of the HE(8) motor neuron in this scenario, a canonical synaptic strength profile would allow the HN(7) interneuron, being the first input, to terminate the burst of the HE(12) motor neuron, promoting a phase advance with respect to the HE(8) motor neuron (Fig 9*C*, dark shaded HE(12) phase box), and thus promoting a larger peristaltic motor progression. If the relative strength of the HN(7) interneuron were to decrease (Fig 9*C*, right synaptic strength profile), the HE(12) motor neuron would fire through the now weaker inhibition of the HN(7) interneuron, promoting a phase delay compared to the canonical synaptic strength profile (Fig 9*C*, light shaded HE(12) phase box), thus reducing the peristaltic motor progression.

The hypotheses presented in the working model above (Fig. 9*B,C*) for the effect of synaptic strength profiles on the peristaltic motor phase progression are embodied in the synaptic strength index (SSI) we have devised. The SSI, by simultaneously considering the disparity in strength between the HN(4) and HN(7) inputs in the HE(8) and the HE(12) motor neurons, captures the effectiveness of both synaptic strength profiles in promoting the largest peristaltic motor phase progression possible given a particular temporal input pattern. Moreover, as demonstrated in the correlation of Figure 8A, at least when motor neuron intrinsic properties and electrical coupling are held constant as

they are in the ensemble model, the SSI has strong predictive value for the peristaltic motor phase progression.

How, then, do temporal patterns and synaptic strength profiles interact such that peristaltic motor patterns are generated? Our data predict that the heartbeat CPG can reliably produce peristaltic motor patterns by ensuring that the temporal pattern generated within the CPG itself results in the largest premotor progression possible. In this way, the premotor progression between the HN(7) and HN(3) interneurons establishes the maximum amount of motor progression available to the motor neurons that these premotor interneurons exclusively innervate (i.e., the HE(7) to HE(14) motor neurons). Once the premotor progression is established, it sets the range over which motor neurons can fire; the synaptic strength profiles can then define where in this range any heart motor neuron does fire and thus determines the motor progression that is realized. The observations that all preparations, fully characterized, produce functional, albeit individual, peristaltic output (Norris et al., 2011) and the results of our present simulation studies in which temporal patterns and synaptic profiles were mixed (Fig. 6) suggest that the limits of motor output set by the temporal pattern in every individual are sufficient to accommodate the variability in synaptic strength profiles observed across animals.

Relevance to motor pattern generation

The current work can illuminate how motor generating networks in other animals, including vertebrates, produce flexible motor outputs. According to our working model, the temporal pattern sets the range of phases over which neurons may fire, while synaptic strength profiles determine which phase is realized. There is, however, some flexibility in the composition of the synaptic strength profiles that are compatible with functional outputs. The synaptic strength profiles between the peristaltic and synchronous coordination modes are similar (Norris et al., 2007a), indicating that the difference in motor output in the two modes must be due to changes in the temporal pattern of premotor activity within the heartbeat CPG. In the leech heartbeat system, the switch in temporal pattern is the result of changes in activity of the bilateral pair of HN(5) interneurons, which we term "switch" interneurons. While one HN(5) interneuron is active, the ipsilateral interneurons of the CPG expresses the synchronous temporal pattern, while the contralateral interneurons expresses the peristaltic temporal pattern. Thus, switches in the activity of the HN(5) interneurons result in a reconfiguration of the premotor temporal patterns. We suggest that other CPGs, e.g., the spinal locomotor CPG, could be reconfigured to produce flexible motor output in an analogous way by combining descending control of temporal patterning in premotor interneurons with non-phasic neuromodulation of synaptic strengths. Descending input, e.g., from the medullary locomotor region for spinal CPG's could act to modify temporal patterning by changing the linkage between the CPG's timing kernel and

premotor interneurons (Grillner et al., 2005) in the way leech switch interneurons produce switches in temporal patterning within the heartbeat CPG. The temporal pattern in the premotor interneurons would then determine largely the motor output but neuromodulatory modification of the synaptic strength profile could then fine-tune motor output to realize specific functional requirements.

CHAPTER 4

GENERAL DISCUSSION

The purpose of this thesis was to elucidate the functional role of motor neuron intrinsic properties in the generation of a fictive motor pattern and to understand how central pattern generating networks (CPG's) combine timing information and patterns of synaptic strengths in the production of functional motor output (fictive pattern). We used our knowledge of the leech heartbeat CPG, a system in which we can measure both timing information and synaptic strength profiles of premotor input patterns, to address these questions. The findings presented here increase our understanding of the leech heartbeat CPG and provide predictions about the heartbeat system that can be further explored in both the modeling studies and experiments in the living system.

4.1 Major Conclusions

4.1.1 Heart Motor Neuron Intrinsic Properties Contribute to Output Phasing

My results in a hybrid systems analysis using the dynamic clamp suggest that heart motor neuron intrinsic properties can functionally contribute to their output phasing in the synchronous coordination mode. Heart motor neurons in

multiple midbody segments receiving the synchronous input pattern express an ability to initiate their burst firing earlier than model motor neurons, providing a phase advance sufficient to match the average phase observed in the living system. I conclude from the dynamic clamp and modeling studies that a needed addition to the model motor neurons receiving the synchronous input pattern is an ability to promote a phase advance compared to the current model.

Surprisingly, heart motor neurons in the hybrid system receiving the peristaltic input pattern in the dynamic clamp did not match the living system phase. Instead, when receiving the same segmental input pattern as our model motor neurons, motor neurons in the hybrid system assume a phase similar to that observed in the model. Where model phase was similar to that observed in the living system (segments 10 and 12), hybrid system phase also matched the living system phase.

I extended my initial modeling effort by using multiple premotor input patterns in the model in order to exclude the possibility that animal-to-animal variability in the premotor temporal pattern and synaptic strength profiles themselves may have contributed to the discrepancy between the model and living system. In the HE(8) motor neurons, no combination of temporal pattern matched either with its own synaptic strength profile or in combination with other synaptic strength profiles, provided a phase delay large enough to match a target phase. Based on these results I suggest that, in the peristaltic mode, the most needed improvement to the HE(8) model motor neurons is an ability to

produce a phase delay rather than a phase advance which is also required in the synchronous mode in this segment (cf 2.5, Chapter 2).

In the HE(12) motor neurons, however, I observed that several temporal patterns could, with their own synaptic strength profiles and in combination with other synaptic strength profiles, produce an appropriate phase when compared to a target. Where a phase delay is required in order to match a target phase (as in the HE(8) motor neurons), however, HE(12) model neurons also do not appear to be able to generate a phase delay.

Given these results, a straightforward requirement for model motor neurons receiving the synchronous input pattern is to add a conductance that promotes a phase advance compared to the model. For example, a low-threshold Ca^{2+} current, similar to that characterized in oscillator heart interneurons (Ivanov and Calabrese 2000) and termed I_{CaF} in a model of the premotor oscillator interneurons of the heartbeat CPG (Hill et al., 2001), could contribute to the ability of the heart motor neurons to express a phase advance compared to the model. In agreement with this suggestion, in experiments in which I replaced the Ca^{2+} in leech saline with equimolar Mn^{2+} in order to block premotor inputs, the hybrid system phase was delayed, although not significantly, compared to the phase observed in normal leech saline. I predict that the characterization of this current in heart motor neurons and subsequent inclusion in the model motor neurons should result in a phase advance in synchronous model output compared to that observed in our initial modeling efforts ((García et al. 2008);

see below). Alternatively, a persistent inward sodium current (I_P), could also contribute to a phase advance in model motor neurons. Although I_P is included in the model, its kinetics were based on that used in a model of premotor oscillator interneurons in the heartbeat CPG (Hill et al., 2001), and its maximal conductance was hand-tuned to provide appropriate activity of the model motor neurons. Characterization of I_P in heart motor neurons would result in a more accurate representation of the current in model motor neurons and may promote a phase advance in model motor neurons in conjunction with or independent of the proposed Ca^{2+} current.

The discrepancies in phase between the model and the living system in the peristaltic mode are intriguing on two fronts. First, the requirements for matching the living system phase are not as straightforward as my data suggest in the synchronous mode. Peristaltic model motor neurons in posterior segments (e.g., segment 14) require phase advances in order to match the living system, whereas anterior motor neurons (e.g., segment 8) require phase delays. It is tempting to assume, therefore, that there may be differences in intrinsic properties in heart motor neurons across segments. However, in experiments measuring outward currents in heart motor neurons, the maximal conductance of several of these currents were not significantly different between segments 7 and 12 (Opdyke and Calabrese, 1995). Furthermore, the experiments presented in Chapter 2, in which multiple input patterns from different segments were played into the same motor neuron pairs (HE(8) and HE(14) pairs) suggest that the

intrinsic properties in these segments are general enough that they can assume a phase consistent with multiple midbody segmental input patterns.

Secondly, the heart motor neurons within a segment receive both peristaltic and synchronous premotor input patterns, suggesting that their intrinsic properties may be similar, of necessity, to accommodate the different synaptic input pattern across switches in coordination modes. In support of this idea, Norris et al.(2007), showed that there was no difference in the spike-mediated synaptic conductance produced in a heart motor neuron by a given premotor interneuron across coordination modes. Experiments in the living system characterizing intrinsic electrical properties in the heart motor neurons across modes could resolve the question of whether they vary with coordination mode.

How, then, does one resolve the competing notions that the heart motor neurons are most likely similar in their intrinsic properties and yet, according to our model, heart motor neurons express two distinct mechanisms for integrating their synaptic input differently from the model? In all honesty, this has been perhaps the most frustrating aspect of this thesis project. That said, however, I think the following is possible. For posterior motor neurons requiring a phase advance (e.g., segment 14), a mechanism similar to that proposed for phase advances in the synchronous coordination mode would work in those model motor neurons. For the anterior motor neurons, I think a Ca^{2+} current that sustains an heart motor neuron burst, separate from the Ca^{2+} current suggested

to provide a phase advance for the model motor neurons receiving the synchronous input pattern, may provide a delay to the phase of the HE(8) motor neuron. For example, in the same oscillator interneuron model mentioned above, the inactivation kinetics of a Ca^{2+} current, termed I_{CaS}, contributes to cycle period by extending burst duration (Hill et al. 2001; Olypher et al. 2006). If a similar current could be characterized in the motor neurons, then I_{CaS} would be ideally suited to provide a phase delay in the anterior motor neurons. Two other alternatives to a Ca^{2+} current would still be possible however: 1) appropriate tuning of the I_P current described above could also provide a phase delay of the heart motor neurons and 2) characterization of an outward current, such as K_{Ca}, whose inactivation kinetics are tuned such that they also promote a phase delay. My prediction is that the maximal conductances of such currents would be similar across segments and modes. Therefore, the output phase of the heart motor neurons involves an interaction between the premotor synaptic input patterns and the heart motor neuron intrinsic properties in which identical intrinsic properties are variably engaged by the input patterns that they receive (cf 2.6, Chapter 2).

I also conclude from these results that, while the HE(12) model motor neuron could be improved by providing a means for a phase delay, these model motor neurons appear to behave in a manner more similar to the corresponding heart motor neurons in the living system than the HE(8) model motor neurons do to their counterparts. One possibility for this difference is the observation that synaptic strength profiles in this segment tend to be canonical across animals.

For example, in 23 preparations in which the HE(12) synaptic strength profiles was measured in the living system, only once was a non-canonical synaptic strength profile observed (Norris et. al., 2011). Therefore, it is possible that the HE(12) motor neurons in the living system are similarly as sensitive to the synaptic input they receive from the HN(7) interneuron as the model motor neurons are. Evidence for this suggestion can be seen in Fig 2.5E. Note that in the peristaltic mode the last spike phase of the HE(12) model motor neuron more closely approximates the living system than in the HE(8) motor neuron. This improved correspondence (relative to the HE(8) motor neuron) is most likely due to the increased relative synaptic strength of the HN(7) interneuron. I propose that the HE(12) motor neurons in the living system are as similarly sensitive to the HN(7) input as model motor neurons, suggesting that there is a range of HE(12) motor neuron phases in the living system that overlap with what the HE(12) model motor neuron can produce when receiving different input patterns. I predict that the range of model phases overlaps with the lower biological range of HE(12) motor neuron phases produced in the living system as model motor neurons cannot generate a phase delay on their own.

4.1.2 Rules Governing Premotor Matching of Temporal Pattern and Synaptic Strength Profiles

In order to produce appropriate rhythmic motor output, CPG's must provide rhythmic activation of the motor neurons that underlie the motor pattern. Currently, studies in which premotor patterns of synaptic drive onto

motor neurons have focused on understanding how their activity is coordinated by their premotor inputs into a functional motor pattern. Based on the results presented in this thesis, I show that the leech heartbeat CPG can produce functional synchronous motor patterns because of the nearly synchronous premotor temporal pattern produced by the premotor interneurons. In the peristaltic mode, functional output can be generated by ensuring that the heartbeat CPG generates the largest premotor phase progression possible. This sets the range of absolute phases over which the heart motor neurons can fire. The synaptic strength profile can then determine the phase progression observed between the HE(8) and HE(12) motor neurons.

4.2 Future Directions for the Heart Motor Neuron Ensemble Model

Here I present some directions for advancing the heart motor neuron ensemble model as well as experiments with the model that could generate predictions that can be tested in the living system. As mentioned above, improvements to the model begin with the implementation of a more realistic complement of intrinsic properties. The following improvements to the model could occur in parallel with the characterization of motor neuron intrinsic properties in the living system.

4.2.1 Multi-Compartment Model

A relatively straightforward improvement to the model would be to add a spatial component to the existing model. The lab has previously generated multicompartment models of one of the oscillator interneurons (Tobin and Calabrese 2006). In that study, three models were presented: one that captured the full morphology of the oscillator interneuron and two reduced models that captured the essential features of the interneurons. I would suggest a reduced model that provides a spatial segregation of the premotor synaptic inputs, active conductances and electrical coupling between pairs of heart motor neurons. The model could consist of several functional regions of the heart motor neurons, including the soma, a synaptic compartment, a neurite compartment, an axon compartment and a compartment for electrical coupling. This model could be used to facilitate parameter exploration studies such as evolutionary algorithms that could be applied to a more morphologically realistic model of the heart motor neurons.

4.2.2 Evolutionary Algorithm

In addition to developing a multi-compartment model, parameter search methods such as evolutionary algorithms may assist those wishing to advance the model in developing complements of intrinsic conductances that lead to output similar to that observed in the living system. Evolutionary algorithms (Smolinski et al. 2006), are an optimization strategy wherein initial populations of model

parameter sets that are determined randomly are used to generate subsequent offspring models that can be selected for or against based on a pre-defined fitness metric. Ideally, a set of "fit" models can then be settled on and explored to determine how the properties of these models produced a desired output. This strategy was previously employed in the lab for modeling oscillator interneurons (Tobin et al., 2006). Metrics that could be used to tune the model include heart motor neuron phase and duty cycle, the slow voltage waveform of the heart motor neurons, spike shape, and F-I curves observed in the living system.

4.2.3 Maximal Expression of Premotor Phase Progression

The results of Chapter 3 suggest that the peristaltic premotor phase progression from the HN(7) to the HN(3) interneuron sets the range over which the heart motor neurons from midbody segments 7 to 14 fire, with the synaptic strength profile determining the actual motor progression between the HE(8) and HE(12) motor neurons. These results could be enhanced by the following modeling studies.

4.2.4 Reduction of Inputs to Ensemble Model Neurons

One approach to determining the extent to which the synaptic strength profile sets the motor progression between the HE(8) and HE(12) motor neurons would be to force the HE(8) and HE(12) model neurons to express the entire premotor phase progression provided to them. In order to force the model to

assume the premotor phase progression, the model motor phase progression would need to be determined by two inputs: one input (the HN(3) interneuron) in the HE(8) motor neuron and one input (the HN(7) interneuron) in the HE(12) motor neuron. To restrict the number of inputs to the HE(8) and HE(12) motor neurons, I would set the g_{Syn} of the HN(4), HN(6) and HN(7) interneurons to 0 nS in the HE(8) model neuron and the g_{Syn} of HN(3), HN(4) and HN(6) interneuron in the HE(12) model neuron to 0 nS. The g_{Syn} of the HN(3) and HN(7) interneurons would then be adjusted such that they provide sufficient inhibition to the model motor neurons. I would predict that the peristaltic motor progression observed in these simulations would be similar to the premotor phase progression of the input pattern. These experiments could then be performed in the hybrid system to confirm the modeling prediction.

4.2.5 Generalized Synaptic Strength Index

Our Synaptic Strength Index (SSI) is a metric that allows us to determine the effectiveness of a synaptic strength profile is. In our modeling and hybrid system experiments, the SSI was able to predict that an artificially inverted synaptic strength profile would result in non-functional motor output. Interestingly, although the SSI appears to be a good indicator of the peristaltic motor progression between segments 8 and 12, the SSI does not include the relative synaptic influence of the HN(3) interneuron, whose contribution to the temporal pattern should set one end of the limit of the motor phase progression, and the HN(6) interneuron, which provides a relatively strong input to both the

HE(8) and the HE(12) motor neurons. Perhaps the SSI, as measured, works for the phase progression between the HE(8) and HE(12) motor neurons because, across animals, the HN(4) and HN(7) premotor interneurons are the strongest inputs onto these motor neurons. It is possible that our SSI may not correlate as strongly with larger peristaltic motor progressions between the HE(7) and HE(14) motor neurons because the synaptic strength profiles in these two motor neurons, which have not been characterized to the extent that they have in the HE(8) and HE(12) motor neurons, have significant input from the HN(3) and/or HN(6) interneurons. I suggest that, once the synaptic strength profiles in these segments are characterized, summed relative strengths of the front premotor interneurons (the HN(3) and HN(4) interneurons) along with summed relative strengths for the middle interneurons (the HN(6) and HN(7) interneurons) be combined in a similar fashion to our SSI to look for correlations with larger peristaltic progressions between the HE(7) and HE(14) motor neurons.

4.2.6 Abstract Representation of Premotor Input Patterns

One question that arises from the results of Chapter 3 is whether heart motor neurons amplify the premotor phase progression provided to them by their premotor temporal patterns and synaptic strength profiles. This question could be addressed in the ensemble model by generating a series of abstract premotor input patterns. For example, synaptic strength profiles for the HE(8) and HE(12) motor neurons could be distributed in regular patterns (i.e., a Gaussian distribution) to determine an “ideal” synaptic strength profile that generates the

maximum motor phase progression. Temporal patterns could be generated with different phase differences among the premotor interneurons, for example, by increasing the phase differences as you proceed from the HN(7) to HN(3) interneuron, that also result in a maximal motor phase progression. With these ideal temporal patterns and synaptic strength profiles, one could look for complements of intrinsic conductances in the heart motor neurons that result in motor phase progressions larger than the phase progression provided by the premotor temporal pattern.

4.2.7 Using a Biologically-derived Synaptic Conductance Waveform

In our initial modeling efforts (García et al. 2008), we chose a specific temporal pattern and matched it to a synaptic strength profile based on the average g_{Syn} measured in many animals. Since then, we have acquired a physiological "database" of preparations in which we have timing information, synaptic strength profiles and motor output. This means we also have the synaptic current traces that generated the synaptic strength profiles for these animals. Although we are confident that our measures of relative synaptic strength and timing are not the cause of the discrepancy between the ensemble model and the living system, we cannot rule out that the underlying dynamics of the HN-HE synapse, which include intraburst synaptic plasticity, may not be accurately represented. In the ensemble model, this plasticity was implemented as a function of a voltage waveform (see Appendix) which increased and decreased exponentially between two voltage values. I suggest that the synaptic

current records from the physiological preparations in our dataset be converted to synaptic conductances (using Ohms Law). These new synaptic conductance waveforms could then be used in parallel experiments in both the model and in hybrid system experiments to assess the effects of intraburst synaptic plasticity on model and heart motor neuron output.

4.3 Future Directions in the Living System

The results presented in Chapter 3 lead to the hypothesis that the premotor phase progression between the HN(7) and HN(3) interneurons defines the absolute range over which the heart motor neurons in segments 7 through 14 may fire. We further hypothesize that the premotor phase progression in turn is determined by synaptic parameters within the heartbeat CPG itself, and not because of feedback, for example, from motor neurons. Therefore, I suggest the following experiments to address these hypotheses.

4.3.1 Correlate the Peristaltic Premotor Phase Progression to the Peristaltic Motor Progression across Midbody Segments 7 to 14

To test the hypothesis that the peristaltic premotor phase progression between the HN(7) and HN(3) interneurons sets the range over which the HE(7) to HE(14) motor neurons fire, I suggest experiments using simultaneous

extracellular recordings of the ipsilateral HN(3) and HN(7) interneurons along with the HE(7) and HE(14) motor neurons in the peristaltic mode. I would then correlate the premotor phase progression with the motor phase progression in the peristaltic mode. I would predict that a strong positive correlation would exist, indicating that larger premotor phase progressions correlate with larger motor phase progressions. My intuition is that premotor and motor phase progressions would be similar; however, if the motor phase progression was smaller than the premotor phase progression, it could indicate that a safety factor is built into the premotor phase progression to ensure functional peristaltic output. However, if the motor phase progression were larger than the premotor phase progression, this result could indicate that perhaps the motor neurons amplify the premotor phase progression provided to them and would indicate a role for motor neuron intrinsic properties not only in their segmental phasing, but also for intersegmental coordination. Follow-up experiments in conjunction with modeling could provide a mechanism for how this amplification occurs.

4.3.2 Correlate Switch Interneuron to Middle Premotor Interneuron Synaptic Strength and/or Oscillator Interneuron to Middle Premotor Interneuron Coupling Strength to Premotor Phase Progression

To test the hypothesis that the premotor phase progression is determined by synaptic interactions within the heartbeat CPG, I suggest experiments in which the premotor phase progression between the HN(7) and HN(3) interneurons is measured via extracellular recordings. I would also include an

extracellular recording of the switch [HN(5)] interneuron for spike-triggered averaging of its synaptic input onto the HN(7) interneuron. Once the premotor phase progression has been measured, the HN(7) interneuron should be voltage-clamped to measure the IPSC's arising from the contralateral HN(5) interneuron, as the contralateral HN(5) interneuron provides the inhibition to the peristaltically coordinated HN(7) interneuron. I would then correlate the strength of the HN(5) synaptic input to the HN(7) interneuron with the HN(7) to HN(3) phase progression; I would predict a strong positive correlation between the synaptic conductance of the HN(5) onto the HN(7) interneuron with the premotor phase progression between the HN(3) and HN(7) interneurons.

Interestingly, a recent study in the lab showed that the phasing of the HN(7) interneurons arises from an interplay between the synaptic conductance (g_{Syn}) provided by the HN(5) interneuron onto the HN(7) interneuron and the electrical coupling conductance (g_{coup}) arising from the HN(3/4) oscillator interneurons onto the HN(7) interneurons (Weaver et al. 2010). In that study, increasing g_{coup} decreased the phase difference between the HN(7) and HN(3) interneuron. I would also suggest correlating HN(3)/HN(4) g_{coup} onto the HN(7) interneuron to the same premotor phase progression. My prediction is that there would be a negative correlation here, owing to the synchronizing effect of g_{coup} on the premotor phase progression. It is also possible that the ratio of this g_{Syn} and g_{coup} may correlate to the premotor phase progression observed if it

is found that neither g_{Syn} or g_{coup} correlate with the premotor phase progression individually.

4.3.3 Explore Heart Motor Neuron Intrinsic Properties and Electrical Coupling across Midbody Segments

The experiments undertaken in this thesis were motivated by the lack of correspondence in phase between our ensemble model motor neurons and the living system. Using a combined modeling and physiological approach, I systematically examined how motor neurons in the living system integrate their segmental input patterns differently from the ensemble model motor neurons. The results presented here suggest that the quantification of intrinsic properties in the heart motor neurons in the living system will be essential to advancing the ensemble model.

In addition to experiments characterizing intrinsic conductances, experiments focused on electrical coupling across segments could address the question of how electrical coupling may contribute to intersegmental coordination. Although we do not expect that heart motor neuron intrinsic properties to vary significantly across segments, the data presented in Chapter 2 suggest that electrical coupling may not be the same across segments, and therefore, in addition to affecting individual phase, electrical coupling may affect intersegmental coordination, as is suggested in our modeling and hybrid system work.

4.3.4 Neuromodulator Studies

It is well established that neuromodulators can exert a profound influence on both motor neuron intrinsic properties and on CPG circuits (Marder and Bucher 2001; Sillar et al. 1997); in fact, rhythmic activity in the *in vitro* neonatal rodent spinal cord preparation is most usually elicited by a cocktail of neuromodulators. At present, only a few studies have looked at the effect of modulatory peptides or classical monoamines on the heartbeat CPG (Nadim and Calabrese 1997; Tobin et al. 2006); for example, myomodulin has been shown to alter bursting activity in oscillator heart interneurons, which could alter the temporal pattern of premotor input and therefore phase of the heart motor neurons. Therefore, I would suggest experiments with neuromodulators, such as myomodulin, searching for one that result in shifts of the phasing of the premotor interneurons with respect to each other. One could then assess whether or not heart motor neuron intrinsic properties are engaged differently in scenarios where the temporal pattern is driven to assume different phase progressions within the CPG circuit itself. Direct assessments of how neuromodulators may affect heart motor neuron intrinsic properties could also be informative. Although bath application of a neuromodulator may result in changes in the period of a heart motor neuron, the change in period would be due to neuromodulatory influences within the CPG and not on the heart motor neurons themselves. Therefore, it would be interesting to explore whether aspects of heart motor neuron activity, such as spike frequency, change in the presence of

a neuromodulator. A change in spike frequency would indicate a change in the intrinsic properties of the motor neurons themselves.

4.3.5 Comparison of Peristaltic Motor Phase Progression to Heart Tube Peristaltic Progression

The results presented in this thesis will be best understood only when placed within the context of the heartbeat patterns themselves. The question, then, becomes how do rules governing the combination of temporal patterns and synaptic strength profiles and the contribution of heart motor neuron intrinsic properties ultimately result in the appropriate heart tube constriction patterns observed *in vivo*. In a recent study, Wenning et al (2004a, b) performed video recordings of blood flow in juvenile leeches. They used changes in a light signal due to blood flow in the heart tubes to generate a phase diagram of the activity of the heart tubes themselves. In that study, they showed that the phase of the heart tube constrictions was similar to the fictive heartbeat motor pattern measured in isolated nerve cords. I propose a similar study in which the peristaltic motor phase progression measured in the living system (isolated nervous system) between the HE(7) and HE(14) motor neurons be paired with prior video analysis of the peristaltic phase progression of the constriction pattern between these same segments. For example, a leech could undergo video analysis of its constriction patterns, then be used in follow up experiments in the nervous system where we measure fictive timing, synaptic strength profiles and motor output to determine their relationship. Such a study would be instrumental in

determining whether the fictive motor output of the leech CNS is faithfully reproduced in the heart tube constriction patterns or if the biomechanical constraints of the heart tubes themselves (or potentially even feedback sensory receptors in the heart, though none are known) result in a modification of the motor output they receive. Furthermore, studies such as these could examine how variability in the fictive motor pattern is translated into functional constriction patterns at the level of the heart tubes. For example, as shown previously (Norris et. al., 2011), there is considerable animal-to-animal variability in fictive timing and synaptic strength profiles and motor output. Is this variability expressed at the level of the heart tubes, or does a transformation of the motor signal produced by the biomechanics of the heart tube occur? Finally, within an animal, the intersegmental phase differences are not uniform across segments (Norris et al., 2007b). Is this variation in intersegmental phase progressions across segments expressed in the heart tubes or are they smoothed out along the heart tube? I believe studies such as these would result in a complete characterization of the behavior, from synaptic parameters within the premotor CPG itself to motor output, an endeavor not possible in other animals.

4.4 Larger Implications

The experiments described in this thesis show that: 1) Motor neuron intrinsic properties can make a functional contribution to the generation of

rhythmic motor output and 2) that a rather simple set of rules govern how timing information and synaptic strength profiles can be combined to produce functional motor output in the leech heartbeat system.

4.4.1 Implications for the Contribution of Motor Neuron Intrinsic Properties to Motor Pattern Generation in Other Animals

The finding that heart motor neuron intrinsic properties can contribute to the output phase observed *in vitro* can inform studies in other animals in which the contribution of motor neuron intrinsic properties to rhythmic motor output has not been determined. This work suggests that a requirement for assessing the contribution of motor neuron intrinsic properties will be a quantitative assessment of the premotor pattern of synaptic drive from the premotor CPG onto the motor neurons.

The contribution of heart motor neuron intrinsic properties observed and/or predicted for heart motor neurons to their output phase may be similar to the putative contributions of motor neuron intrinsic properties to motor output in other systems. For example, in my hybrid systems analysis of heart motor neuron intrinsic properties, I show that heart motor neuron intrinsic properties provide a phase advance compared to the ensemble model when receiving the synchronous input pattern. The ability of heart motor neuron intrinsic properties to promote a phase advance is similar to the finding in neonatal rodent motor neurons that I_h can promote a phase advance of the transition from the inhibitory

to the excitatory phase of its locomotor cycle in the presence of rhythmic input (Kiehn et al., 2000). Furthermore, my prediction that an inward current that would promote a phase delay would also mirror work in the neonatal rodent spinal cord, in which motor neurons express plateau potentials that result in continued motor activity in the absence of synaptic input (Kiehn and Eken 1998). Finally, recent data in adult zebrafish has shown that certain motor neuron pools in the zebrafish spinal cord show voltage sags indicative of I_h that could play a role in generating swimming activity (Gabriel et al., 2011).

The data presented in chapter 2, Fig 6, in which modified conductance waveforms were used to engage heart motor neuron intrinsic properties in a variable manner, could provide information on how motor neuron intrinsic properties in other systems may or may not contribute functionally to motor output. For example, heart motor neurons are dedicated to the heartbeat system, unlike other motor neurons in the leech CNS. Motor neurons that participate in the turtle scratch motor pattern, however, are used in locomotion in addition to scratch, as is the case for spinal interneurons (Berkowitz 2008). Therefore, although turtle motor neuron intrinsic properties may not contribute to motor output for fictive scratch (Alaburda et al., 2005, Berg et al., 2007), they might contribute to other motor behaviors in which they are involved.

In terms of broader impact, the results shown here may inform searches for therapeutic strategies for recovery from spinal cord injury (SCI), a condition whose primary symptom is the loss of locomotor movements. My data may

provide an initial estimate of how much of a motor neurons output phase in the spinal cord can be accounted for by the intrinsic properties of those motor neurons. Currently, the most effective strategy for regaining some aspect of locomotor control is treadmill training (Edgerton and Roy 2002), which is thought to provide appropriate sensory information throughout a step cycle in addition to providing use-dependent facilitation of synapses activated during locomotion. If it can be shown that motor neurons in the spinal cord contribute to motor output, then, in the case of spinal cord injury, motor neurons could be targeted for activation by stimulation methods with rhythmic and /or phasic patterns of activation that could assist in the recovery of locomotor control, an approach that has been demonstrated in frogs (Bizzi et al, 1991) and cats (Mushahwar and Gauthier, 2002).

4.4.2 Implications for Intersegmental Coordination of Motor Pattern Generation in Other Animals

My finding that the temporal pattern sets the range over which heart motor neurons fire, while synaptic strengths determine motor progressions has interesting implications for how other CPG networks can produce flexible motor output. The data here suggest that, by predetermining the range of motor neuron firing, a CPG network can accommodate variability in synaptic strength profiles (within some biological range) onto motor neurons while maintaining functional motor output. For example, a switch in locomotor gaits (e.g., walking forward/backward) in limbed animals would result from either a descending

input from the medullary locomotor region (MLR) or a descending neuromodulatory input that reconfigures the premotor interneuronal network, as occurs in the pyloric CPG of the STN (Johnson et al. 2011). Assuming that the reconfigured network is interacting with the same pool of motor neurons, my results suggest that the change in the linkage between the CPG kernel and the temporal premotor pattern does not necessarily have to be accompanied by a change in the synaptic strength profile produced on the motor neurons. By not requiring that both timing information and synaptic strength profiles be changed together, the premotor CPG would not need to regulate synaptic strength across locomotor gaits. Instead, nonphasic neuromodulation of synaptic strengths could fine-tune motor output such that functional requirements are met.

My data can also inform studies on how motor neurons can be coordinated to produce intersegmental motor patterns. Studies in tadpoles have suggested that the wave of activity during swimming is the result of a rostro-caudal gradient of both excitability and inhibition (Roberts and Tunstall 1994; Tunstall and Roberts 1994). The primary spinal neuron types have now been defined and experiments are under way to assess which premotor interneurons provide excitatory and inhibitory synaptic input onto motor neurons (Soffe et al. 2009). Although the heartbeat system does not exhibit an “excitability gradient”, as the premotor synaptic inputs onto heart motor neurons are inhibitory, they do exhibit segmental trends in the average relative strengths of their synaptic inputs, with middle premotor interneuron relative synaptic strengths increasing as front premotor interneuron relative synaptic strengths decrease when one moves from

segment 8 rearward to segment 14. My data suggest similar trends in synaptic strength profiles for premotor interneurons could account for the excitatory and inhibitory gradients of synaptic drive onto motor neurons in the tadpole swim system as well.

4.5 Final Conclusions

In conclusion, the work presented in this thesis suggests that a quantification of the premotor pattern of synaptic drive onto motor neurons will be required in order to understand how motor neuron intrinsic properties contribute to rhythmic motor pattern generation. Furthermore, the results presented here may be extended to explore further questions in the leech heartbeat system. Finally, some aspects of this work may inform studies designed to produce therapeutic strategies for patients with spinal cord injury.

APPENDIX: HEART MOTOR NEURON ENSEMBLE MODEL CONSTRUCTION

A.1 General Modeling Strategy

The heart motor neuron ensemble model was implemented using GENESIS (GEneral NEural Simulation System) software (Bower and Beeman 1998). Each of the 32 heart motor neurons (16 bilateral pairs) were modeled as single compartment neurons with intrinsic conductances, inhibitory synaptic conductances, and a conductance for the electrical junctions linking bilateral segmental pairs. Inhibitory synaptic input onto the model motor neurons arises from ipsilateral premotor heart (HN) interneurons; four identified bilateral pairs - the HN(3), HN(4), HN(6), and HN(7) interneurons - and one unidentified bilateral HN(X) pair. The timing of these inputs (temporal pattern) was derived from 13 bursts of heart interneuron extracellular recordings and the intersegmental conduction delays, and the strengths of each input (spatial pattern) from averaged voltage clamp recordings and estimated time course of synaptic plasticity: both described in detail below. The simulation ran for 60 s with a time step of 0.0001 s, and the middle ten bursts of the motor neurons (fictive motor pattern) sculpted from the 13 bursts of inhibitory input were used in analysis. A bilateral pair of electrically coupled model motor neurons in one ganglion and their associated synaptic inputs forms the fundamental module of the ensemble model.

The current balance equation for the membrane potential (V) of each individual model heart motor neuron was:

$$(1) \qquad C\frac{dV}{dt} = -(I_{Na} + I_P + I_{KA} + I_{K1} + I_{K2} + I_{Syn} + I_{Coup} + I_{inject})$$

where t is time, C is total membrane capacitance, I_{leak} is the leak current, I_{Coup} is the junctional current for the electrical coupling and (I_{Syn}) is the sum of the synaptic currents for the inhibitory chemical synapses. Each motor neuron contained five voltage-dependent ionic currents: a fast Na^+ current (I_{Na}), a persistent Na^+ current (I_P), a fast transient K^+ current (I_{KA}), an inactivating delayed rectifier K^+ current (I_{K1}) and a non-inactivating delayed rectifier K^+ current (I_{K2}). The Hodgkin-Huxley equations (Hodgkin and Huxley 1952) describing these currents were those used for a model of an oscillator heart interneuron (Hill et al. 2001). The maximal conductance, $\bar{g}_{ion}$, of the currents were set empirically to match the general activity of heart motor neurons recorded intracellularly in the living system ($\bar{g}_{Na} = 200\ nS, \bar{g}_p = 8.5\ nS, \bar{g}_{KA} = 50\ nS, \bar{g}_{K1} = 100\ nS, \bar{g}_{K2} = 80\ nS$). The specific membrane resistance was 1.1 Ωm^2, the specific membrane capacitance was 0.05 Fm^{-2}. Each motor neuron was modeled as an isopotential cylinder with length and diameter equal (60 μm). These cell proportions result in an input resistance of each model motor neuron

of 97 MΩ, a value that falls within the range measured in the living system (Opdyke and Calabrese 1995).

A.3 Modeling Premotor Inhibitory Synaptic Inputs: Temporal Pattern

Sixty seconds of simultaneous extracellular recording from ipsilateral HN(3), HN(4), HN(6), and HN(7) premotor interneurons both in the synchronous and in the peristaltic coordination mode were used to generate the temporal pattern of synaptic inputs onto the model motor neurons (like Fig. 2 in Norris et al. (2006)). The peristaltic and synchronous input patterns were aligned to one another by assigning a phase of 0.0 to the middle spike of the first peristaltic HN(4) burst and a phase of 0.51 to the middle spike of the first synchronous HN(4) burst, which is the average side-to-side phase difference between the peristaltic and synchronous HN(4) activity observed in the living system (Norris et al. 2006). The period of the data set used for playback in our canonical ensemble model was 4.3 s. The average period for the living system varies from 4.0 – 8.5 s (average 5.8 s) (Norris et al. 2006). Extracellular recordings of the spike times are not available for the HN(X) interneuron, so its temporal pattern was bootstrapped to conform generally to its pattern of IPSCs recorded in heart motor neurons (Norris et al. 2006). Intersegmental conduction delays were assigned to be 20 ms per segment in conformity with measurements from the lining system (Fig. 3*B* in Norris et al. (2007)). Spikes in the identified premotor neurons in both coordination modes and the HN(X) interneuron in the peristaltic mode travel rearward, but the HN(X) interneuron's spike in the synchronous mode travel

frontward (Calabrese 1977). The temporal pattern of synaptic inputs was then constructed for each segmental module from the basic peristaltic (for left model motor neurons) and synchronous (for right model motor neurons) spike time patterns offset by the appropriate intersegmental conduction delays.

A.4 Modeling Premotor Inhibitory Synaptic Inputs: Spatial Pattern

The relative synaptic weights of premotor inputs to each model motor neuron were assigned based on experimental data multiplied by a scaling factor. Thus, we initially set the maximal synaptic conductance $\bar{g}_{Syn}$ from each of the identified premotor inputs to each motor neuron for both coordination modes to the average conductance value form voltage clamp data in Fig. 3*A* of Norris et al. (2007). In the living system, for all the identified premotor interneurons, there was no statistical difference between the average synaptic conductance in the same motor neuron for the two coordination modes (Norris et al. 2007). On the other hand, the synaptic weights appeared to be slightly different for the peristaltic and synchronous HN(X) inputs (Fig. 3*A* (Norris et al. 2007)).In our ensemble model, we used an approximate average value of $\bar{g}_{Syn}$for the HN(X) inputs to the model motor neurons of the two sides (HE(3) 6.5 nS; HE(4) 6.25 nS; HE(5) 5.75 nS; HE(6) 2.0 nS) except where noted. A uniform (see text for exceptions) scaling factor, σ, was then applied to these maximal conductances producing a scaled $\bar{g}_{Syn}$, in order to obtain appropriate duty cycles for model motor neuron activity as described in the text. For each synaptic input to each model motor neuron, the synaptic current was calculated as:

$$(2) \quad I_{Syn} = g_{Syn}\,(V_m - E_{rev})$$

where g_{Syn} is the instantaneous conductance (calculated as indicated below from the scaled $\bar{g}_{Syn}$) of the specific premotor input, I_{Syn} is the associated post-synaptic current, V_m is the instantaneous membrane potential of the model motor neuron, and E_{rev} is the reversal potential, assumed to be -62.5 mV (Angstadt and Calabrese 1991).

Each spike time in the temporal pattern triggered a synaptic activation function, $f_{Syn}(t)$ given by:

$$(3) \quad f_{Syn}(t) = a(e^{-t/\tau_1} - e^{-t/\tau_2})$$

where a is a normalization constant chosen so that the maximal value of $f_{Syn}(t)$ = 1. Thus,

$$(4a) \quad a = \frac{1}{e^{-t_{peak}/\tau_1} - e^{-t_{peak}/\tau_2}}$$

where,

$$(4b) \quad t_{peak} = \frac{\tau_1\tau_2 ln\frac{\tau_1}{\tau_2}}{\tau_1 - \tau_2}$$

The time constants determine, respectively, the decay and rise times of the synaptic conductance ($\tau_1 > \tau_2$). In the model, the synaptic time constants for the premotor input originating from the HN(3), HN(4), HN(6), and HN(7) interneurons were set based on measurements from typical voltage clamp records: τ_1 = 0050 and τ_2 = 0.004 in Norris et al. (2007). Greater summation in the synaptic input from the inputs from the HN(X) interneurons has been observed experimentally (Norris et al. 2007), so τ_1 was increased to 0.1 for these synapses.

During each premotor interneuron burst, the postsynaptic currents show intraburst synaptic plasticity (Figs. 4 and 5, Norris et al. 2007). This short-term synaptic plasticity was included in the ensemble model by modifying equations from Hill et al (2001) for synaptic plasticity in a conductance-based heart interneuron model. M is a synaptic plasticity factor that in this case is an instantaneous function of presynaptic voltage, V_{pre}:

$$(5) \quad M_\infty = 0.1 + \frac{0.9}{1+e^{-1000(V_{pre}+0.04)}}$$

Because only the spike times of the premotor interneurons are used as inputs to the model, we created a V_{pre} waveform for each premotor input that simulated the presynaptic membrane potential oscillation. This waveform increased exponentially from -50 to -30 mV for the first 75% of the premotor burst and then decayed exponentially from that point back to -50 mV. The rise and fall of V_{pre} was thus defined by two time constants, $\tau_{plast-Rise}$ and $\tau_{plast-Decay}$

that effectively control the time course of M and thus the rise and fall of synaptic strength. Each of these time constants was set to 0.250 s, standard values that approximated the IPSC plasticity (synaptic enhancement early in a burst and synaptic depression late in a burst) observed in voltage-clamp recordings of Norris et al. (2007b).

A.5 Spatiotemporal Pattern

Combining the spatial and temporal patterns for each synaptic input, equation (*1*) becomes:

$$(6) \quad I_{Syn(HN(\#))}(t,V) = \sum_{s-1}^{s} M \cdot f_{Syn(HN(\#))}(t - t_s) \cdot \sigma \cdot \bar{g}_{Syn(HN(\#))}(V_m - E_{rev})$$

where *s* is the numerical order of each presynaptic spike in the temporal pattern for the given input and t_s is the time of occurrence of that spike and σ is the synaptic scaling factor defined above with reference to *(2)*.

The I_{Syn} for each given model motor neuron in the current-balance equation (*1*) is the sum of all synaptic input onto each premotor cell:

$$(7) \quad I_{Syn} = \sum_{HN(\#)=X,3,4,6,7} I_{Syn}(HN(\#))$$

where $I_{Syn(X)}$ is the specific synaptic current onto that motor neuron from the HN(X) heart interneuron, $I_{Syn(3)}$ is the specific synaptic current onto that motor

neuron from the HN(3) interneuron, and so on. A snapshot of the resultant spatiotemporal pattern of synaptic inputs can be gained from the conductance plots of Fig. 4 of García et al., 2008 for the independent g_{Syn} and combined $\bar{g}_{Syn}$ synaptic inputs to the HE(3) and HE(10) model motor neurons, peristaltic and synchronous.

A.6 Modeling Electrical Coupling

The electrical junctions between the bilateral heart motor neuron pairs were modeled to reflect measured coupling coefficient (average 0.34) and low-pass filtering (50 Hz cut off frequency; -3 dB) gathered from experiments in the living system on isolated ganglia (Peterson 1983). This match was achieved by setting the maximal conductance of the electrical coupling, g_{Coup}, to 6 nS and filtering I_{Coup} with a simulated RC circuit. The equations for the model electrical synapse were:

$$(8a) \quad I_{Coup} = I_a = g_{coup}\,(V_a(t) - V_b(t))$$

$$(8b) \quad I_{Coup} = I_b = -I_a$$

where I_a is the current into motor neuron a and I_b is the current into motor neuron b. V_a and V_b are the membrane voltages of motor neurons a and b, respectively; and g_{Coup} is the maximal conductance of the electrical junction.

REFERENCE LIST

Alaburda A, Russo R, MacAulay N, and Hounsgaard J. Periodic high-conductance states in spinal neurons during scratch-like network activity in adult turtles. *J Neurosci* 25: 6316-6321, 2005.

Bayliss DA, Viana F, Bellingham MC, and Berger AJ. Characteristics and Postnatal-Development of a Hyperpolarization-Activated Inward Current in Rat Hypoglossal Motoneurons in-Vitro. *Journal of Neurophysiology* 71: 119-128, 1994.

Berger AJ. Determinants of respiratory motoneuron output. *Resp Physiol* 122: 259-269, 2000.

Berkowitz A. Physiology and morphology of shared and specialized spinal interneurons for locomotion and scratching. *Journal of Neurophysiology* 99: 2887-2901, 2008.

Bower, and Beeman. *The Book of Genesis*. New York City: Springer-Verlag, 1998.

Calabrese R. The Neural Control of Alternate Heartbeat Coordination States in the Leech, *Hirudo medicinalis*. *Journal of Comparative Physiology* 122: 111-143, 1977.

DeLong ND, Beenhakker MP, and Nusbaum MP. Presynaptic inhibition selectively weakens peptidergic cotransmission in a small motor system. *J Neurophysiol* 102: 3492-3504, 2009.

Edgerton VR, and Roy RR. Paralysis recovery in humans and model systems. *Current Opinion in Neurobiology* 12: 658-667, 2002.

Feldman JL, Smith JC, and Liu G. Respiratory pattern generation in mammals: in vitro en bloc analyses. *Current Opinion in Neurobiology* 1: 590-594, 1991.

García PS, Wright TM, Cunningham IR, and Calabrese RL. Using a model to assess the role of the spatiotemporal pattern of inhibitory input and intrasegmental electrical coupling in the intersegmental and side-to-side coordination of motor neurons by the leech heartbeat central pattern generator. *Journal of Neurophysiology* 100: 1354-1371, 2008.

Goaillard JM, Taylor AL, Schulz DJ, and Marder E. Functional consequences of animal-to-animal variation in circuit parameters. *Nat Neurosci* 12: 1424-1430, 2009.

Grillner S. The motor infrastructure: from ion channels to neuronal networks. *Nature reviews* 4: 573-586, 2003.

Hildebrandt JP. Circulation in the Leech, Hirudo-Medicinalis L. *Journal of Experimental Biology* 134: 235-246, 1988.

Hill AA, Lu J, Masino MA, Olsen OH, and Calabrese RL. A model of a segmental oscillator in the leech heartbeat neuronal network. *J Comput Neurosci* 10: 281-302, 2001.

Ivanov AI, and Calabrese RL. Intracellular Ca2+ Dynamics During Spontaneous and Evoked Activity of Leech Heart Interneurons: Low-Threshold Ca Currents and Graded Synaptic Transmission. *J Neurosci* 20: 4930-4943, 2000.

Johnson BR, Brown JM, Kvarta MD, Lu JYJ, Schneider LR, Nadim F, and Harris-Warrick RM. Differential Modulation of Synaptic Strength and Timing Regulate Synaptic Efficacy in a Motor Network. *Journal of Neurophysiology* 105: 293-304, 2011.

Kiehn O. Locomotor circuits in the mammalian spinal cord. *Annual review of neuroscience* 29: 279-306, 2006.

Kiehn O, and Eken T. Functional role of plateau potentials in vertebrate motor neurons. *Curr Opin Neurobiol* 8: 746-752, 1998.

Kiehn O, Kjaerulff O, Tresch MC, and Harris-Warrick RM. Contributions of intrinsic motor neuron properties to the production of rhythmic motor output in the mammalian spinal cord. *Brain Res Bull* 53: 649-659, 2000.

Li WC, Perrins R, Soffe SR, Yoshida M, Walford A, and Roberts A. Defining classes of spinal interneuron and their axonal projections in hatchling Xenopus laevis tadpoles. *Journal of Comparative Neurology* 441: 248-265, 2001.

Macagno E. The number and distribution of neurons in leech segmental ganglia. *Journal of Comparative Neurology* 190: 283-302, 1980.

Maranto AR, and Calabrese RL. Neural Control of the Hearts in the Leech, Hirudo-Medicinalis .1. Anatomy, Electrical Coupling, and Innervation of the Hearts. *Journal of Comparative Physiology* 154: 367-380, 1984a.

Maranto AR, and Calabrese RL. Neural Control of the Hearts in the Leech, Hirudo-Medicinalis .2. Myogenic Activity and Its Control by Heart Motor Neurons. *Journal of Comparative Physiology* 154: 381-391, 1984b.

Marder E, and Bucher D. Central pattern generators and the control of rhythmic movements. *Curr Biol* 11: R986-996, 2001.

Marder E, and Bucher D. Understanding circuit dynamics using the stomatogastric nervous system of lobsters and crabs. *Annu Rev Physiol* 69: 291-316, 2007.

Marder E, and Calabrese RL. Principles of rhythmic motor pattern generation. *Physiol Rev* 76: 687-717, 1996.

Nadim F, and Calabrese RL. A Slow Outward Current Activated by FMRFamide in Heart Interneurons of the Medicinal Leech. *J Neurosci* 17: 4461-4472, 1997.

Norris BJ, Weaver AL, Morris LG, Wenning A, García PA, and Calabrese RL. A central pattern generator producing alternative outputs: Temporal pattern of premotor activity. *Journal of Neurophysiology* 96: 309-326, 2006.

Norris BJ, Weaver AL, Wenning A, García PS, and Calabrese RL. A central pattern generator producing alternative outputs: Pattern, strength, and dynamics of premotor synaptic input to leech heart motor neurons. *Journal of Neurophysiology* 98: 2992-3005, 2007a.

Norris BJ, Weaver AL, Wenning A, García PS, and Calabrese RL. A central pattern generator producing alternative outputs: Phase relations of leech

heart motor neurons with respect to premotor synaptic input. *Journal of Neurophysiology* 98: 2983-2991, 2007b.

Norris BJ, Wenning A, Wright TM, and Calabrese RL. Constancy and variability in the output of a central pattern generator. *Journal of Neuroscience* 2011.

Nusbaum MP, and Beenhakker MP. A small-systems approach to motor pattern generation. *Nature* 417: 343-350, 2002.

Olypher A, Cymbalyuk G, and Calabrese RL. Hybrid systems analysis of the control of burst duration by low-voltage-activated calcium current in leech heart interneurons. *Journal of Neurophysiology* 96: 2857-2867, 2006.

Prinz AA, Bucher D, and Marder E. Similar network activity from disparate circuit parameters. *Nat Neurosci* 7: 1345-1352, 2004.

Puhl JG, and Mesce KA. Keeping It Together: Mechanisms of Intersegmental Coordination for a Flexible Locomotor Behavior. *Journal of Neuroscience* 30: 2373-2383, 2010.

Roberts A, and Tunstall MJ. Longitudinal Gradients in the Spinal-Cord of Xenopus Embryos and Their Possible Role in Coordination of Swimming. *Eur J Morphol* 32: 176-184, 1994.

Schulz DJ, Goaillard JM, and Marder EE. Quantitative expression profiling of identified neurons reveals cell-specific constraints on highly variable levels of gene expression. *P Natl Acad Sci USA* 104: 13187-13191, 2007.

Shafer MR, and Calabrese RL. Similarities and differences in the structure of segmentally homologous neurons that control the hearts of the leech, Hirudo medicinalis. *Cell Tissue Res* 214: 137-153, 1981.

Sillar KT, Kiehn O, and Kudo N. Chemical Modulation of Vertebrate Motor Circuits. In: *Neurons, Networks and Behavior*, edited by Stein P, Grillner S, Selverston AI, and Stuart DG. Cambridge, Massachusettes: MIT Press, 1997.

Skinner FK, Kopell N, and Mulloney B. How does the crayfish swimmeret system work? Insights from nearest-neighbor coupled oscillator models. *Journal of Computational Neuroscience* 4: 151-160, 1997.

Smolinski TG, Boratyn GM, Milanova M, Buchanan R, and Prinz AA. Hybridization of independent component analysis, rough sets, and multi-objective evolutionary algorithms for classificatory decomposition of cortical evoked potentials. *Lect N Bioinformat* 4146: 174-183186, 2006.

Soffe SR, Roberts A, and Li WC. Defining the excitatory neurons that drive the locomotor rhythm in a simple vertebrate: insights into the origin of reticulospinal control. *J Physiol-London* 587: 4829-4844, 2009.

Suzue T. Respiratory Rhythm Generation in the Invitro Brain-Stem Spinal-Cord Preparation of the Neonatal Rat. *J Physiol-London* 354: 173-&, 1984.

Thompson WJ, and Stent GS. Neuronal Control of Heartbeat in Medicinal Leech .1. Generation of Vascular Constriction Rhythm by Heart Motor Neurons. *Journal of Comparative Physiology* 111: 261-279, 1976a.

Thompson WJ, and Stent GS. Neuronal Control of Heartbeat in Medicinal Leech .2. Intersegmental Coordination of Heart Motor Neuron Activity by Heart Interneurons. *Journal of Comparative Physiology* 111: 281-307, 1976b.

Tobin AE, and Calabrese RL. Endogenous and half-center bursting in morphologically inspired models of leech heart interneurons. *J Neurophysiol* 96: 2089-2106, 2006.

Tobin AE, Van Hooser SD, and Calabrese RL. Creation and reduction of a morphologically detailed model of a leech heart interneuron. *J Neurophysiol* 96: 2107-2120, 2006.

Tolbert LP, and Calabrese RL. Anatomical Analysis of Contacts between Identified Neurons That Control Heartbeat in the Leech Hirudo-Medicinalis. *Cell and Tissue Research* 242: 257-267, 1985.

Tunstall MJ, and Roberts A. A Longitudinal Gradient of Synaptic Drive in the Spinal-Cord of Xenopus Embroys and Its Role in Coordination of Swimming. *J Physiol-London* 474: 393-405, 1994.

Wadden T, Grillner S, Matsushima T, and Lansner A. Undulatory Locomotion - Simulations with Realistic Segmental Oscillator. *Computation and Neural Systems* 301-306539, 1993.

Weaver AL, Roffman RC, Norris BJ, and Calabrese RL. A role for compromise: synaptic inhibition and electrical coupling interact to control phasing in the leech heartbeat CpG. *Front Behav Neurosci* 4: 2010.

Wenning A, Cymbalyuk GS, and Calabrese RL. Heartbeat control in leeches. I. Constriction pattern and neural modulation of blood pressure in intact animals. *J Neurophysiol* 91: 382-396, 2004a.

Wenning A, Hill AA, and Calabrese RL. Heartbeat control in leeches. II. Fictive motor pattern. *J Neurophysiol* 91: 397-409, 2004b.

Wright TM, and Calabrese RL. Contribution of motor neuron intrinsic properties to fictive motor pattern generation. *Journal of Neurophysiology* 2011.